

STACKED MICROCHANNEL HEAT SINKS FOR LIQUID COOLING OF  
MICROELECTRONICS DEVICES

A Dissertation  
Presented to  
the Academic Faculty

by

Xiaojin Wei

In Partial Fulfillment  
of the Requirements for the Degree of  
Doctor of Philosophy in Mechanical Engineering

Georgia Institute of Technology  
November 2004

Copyright © Xiaojin Wei 2004

STACKED MICROCHANNEL HEAT SINKS FOR LIQUID COOLING  
OF  
MICROELECTRONICS DEVICES

Approved by:

Dr. Yogendra K. Joshi, Chair/Advisor  
School of Mechanical Engineering

Dr. Peter Hesketh  
School of Mechanical Engineering

Dr. Andrei Fedorov  
School of Mechanical Engineering

Dr. C. P. Wong  
School of Material Science and Engineering

Dr. Bruno Frazier  
School of Electrical and Computer Engineering

Date Approved:  
November 2004

## ACKNOWLEDGEMENT

I would like to thank my advisor, Dr. Yogendra Joshi, for his guidance, encouragement and support during the course of this study at the University of Maryland College Park and Georgia Institute of Technology.

I am also grateful to my dissertation committee members including Dr. Peter Hesketh, Dr. Andrei Fedorov, Dr. Bruno Frazier and Dr. C.P. Wong for their time and efforts in reviewing the proposals and dissertations and their helpful advices.

My sincere gratitude goes to DARPA and Intel Corporation for their financial support. I would also like to thank the University of Maryland College Park for their financial support in the form of Graduate School Fellowship.

I would also like to take this opportunity to express my appreciations and thanks to my friends in the Microelectronics and Emerging Technologies Thermal Laboratory for their support and help.

Special acknowledgement goes to my wife Xiaoyuan for her continuous support throughout my years as a graduate student.

## TABLE OF CONTENTS

ACKNOWLEDGEMENT	iii
LIST OF TABLES	vi
LIST OF FIGURES	vii
LIST OF SYMBOLS OR ABBREVIATIONS	xi
SUMMARY	xvii
<b>CHAPTER 1 INTRODUCTION</b>	<b>1</b>
1.1 Motivation	2
1.2 Literature review	6
1.2.1 Review of microchannel concepts	6
1.2.2 Review of experimental studies in microchannel	8
1.2.3 Review of analytical studies in micro-channel	9
1.2.4 Review of Micro Particle Image Velocimetry techniques for micro-channel flow	10
1.3 Objectives	14
1.4 Overview of the current study	15
<b>CHAPTER 2 EXPERIMENTAL SETUP AND PROCEDURES</b>	<b>17</b>
2.1 Experimental setup for heat transfer study	17
2.1.1 Test module	18
2.1.2 Test facilities	22
2.2 Test matrix and procedures for heat transfer experiments	23
2.3 Uncertainty analysis	25
2.4 Experimental setup for PIV measurement	27
2.5 Procedures for Micro-PIV measurement	30
<b>CHAPTER 3 FABRICATION OF THE STACKED MICROCHANNEL STRUCTURES</b>	<b>32</b>
3.1 Etching of microchannels and manifolds	35
3.2 Bonding component layers into a stack	40
3.3 Metallization	44
3.4 Packaging	46
3.5 Fabrication of the test chip for Micro PIV measurement	47

3.6 Summary	48
<b>CHAPTER 4 EVALUATION OF THE THERMAL PERFORMANCE OF STACKED MICROCHANNEL HEAT SINKS</b>	<b>49</b>
4.1 Experimental study	49
4.1.1 Uniform heating	50
4.1.2 Partial heating	57
4.2 Numerical study of the conjugate heat transfer for stacked microchannels	62
4.2.1 Model construction and validation	62
4.2.2 Modeling results and discussion	65
4.3 Summary and conclusions	73
<b>CHAPTER 5 CHARACTERIZATION OF LAMINAR FLOW INSIDE MICROCHANNELS USING MICRO RESOLUTION PARTICLE IMAGE VELOCIMETRY</b>	<b>75</b>
5.1 Considerations for Micro-PIV measurement	75
5.1.1 Seeding particles	75
5.1.2 Spatial resolution and depth of measurement	77
5.1.3 Refractive index correction for Micro-PIV measurement	80
5.1.4 Image processing and correlation analysis	82
5.2 Results and discussion	87
5.2.1 Fully developed velocity profile	87
5.2.2 Developing flow near entrance	93
5.2.3 Pressure drop	95
5.3 Effects of the sidewall profile on flow and heat transfer	96
5.3.1 Velocity profile and pressure drop	97
5.3.2 Heat transfer	100
5.4 Summary and Conclusion	106
<b>CHAPTER 6: SUMMARY, CONCLUSIONS, DESIGN GUIDELINES AND RECOMMENDATIONS FOR FUTURE WORK</b>	<b>108</b>
6.1 Summary	108
6.2 Conclusions	108
6.3 Design guidelines for stacked microchannel heat sinks	111
6.4 Recommendation for future work	112
<b>REFERENCES</b>	<b>113</b>

## LIST OF TABLES

Table 2.1 Microchannel dimensions (mm)	20
Table 2.2 Testing matrix	24
Table 3.1 Fabrication steps for STMC	34
Table 4.1 Thermal resistances for different power input for counter flow	57
Table 4.2 Thermal resistances for different power input for parallel flow	57
Table 4.3 Computational conditions for parallel flow	63
Table 4.4 Computational conditions for counter flow	64
Table 5.1 The effective particle image sizes and depths of measurement using f-number described in equation (5.4) and equation (5.5)	79
Table 5.2 Dimensions of the channels for Micro-PIV measurement	88
Table 5.3 Location of the plane with maximum velocity for channels SG34	98
Table 5.4 Local Nusselt number for 5° trapezoidal channel and rectangular channel	101
Table 5.5 Nusselt numbers for rectangular, positively tapered and re-entrant channels for H2 boundary condition or conjugate heat transfer ( $x^+=0.45$ )	105

## LIST OF FIGURES

Figure 1.1 Comparison of pressure drop and thermal resistance for different number of layers at fixed flow rate ( $0.83 \times 10^{-6} \text{ m}^3/\text{s}$ or 50 ml/min)	4
Figure 2.1 Schematic of the test flow loop	18
Figure 2.2 Schematic of the stacked microchannel test module	19
Figure 2.3 Dimensions of stacked microchannels	20
Figure 2.4 Schematic of the bonded prototype (a) Parallel flow arrangement (b) Counter flow arrangement	21
Figure 2.5 Thin film heaters and nine resistive temperature sensors (s1 to s9)	22
Figure 2.6 Schematic of a Micro-PIV test setup	28
Figure 2.7. Double-frame camera timing and Nd:YAG laser Q-switch pulse firing for cross-correlation PIV data acquisition	29
Figure 2.8 Schematic of the microchannel structure for using in micro-PIV measurement	30
Figure 2.9 Reference coordinates for the velocity measurement	31
Figure 3.1 Schematic of a stacked microchannel (STMC): All layers have the same overall dimension	33
Figure 3.2 Effects of channel aspect ratio on the side wall profile	36
Figure 3.3 Effects of channel aspect ratio on the etching rate	37
Figure 3.4 Fabrication steps for microchannels with features on both sides	38
Figure 3.5 Samples fabricated using DRIE etching	39
Figure 3.6 IR image of a bonded stack of MC1 and MC2	42
Figure 3.7 Effects of annealing temperature on bonding interface (600x)	43
Figure 3.8 Lift-off process steps for heaters and temperature sensors	45

Figure 3.9 SEM picture of the cross section of a bonded microchannel for Micro-PIV. All dimensions are in $\mu\text{m}$ .	47
Figure 4.1 Typical calibration curves for the resistive sensors	50
Figure 4.2 Wall temperature distribution for parallel flow and uniform heating	52
Figure 4.3 Wall temperature distribution for counter flow and uniform heating	53
Figure 4.4 Total thermal resistances for parallel flow and counter flow with equal flow rate at each of the two microchannels layers	53
Figure 4.5 Total thermal resistances for parallel flow with different interlayer flow rate ratio	54
Figure 4.6 Total thermal resistances for counter flow with different interlayer flow rate ratio	54
Figure 4.7 On-chip thermal resistances for different flow combinations	56
Figure 4.8 Temperature distribution for parallel flow with downstream half heating	58
Figure 4.9 Temperature distribution for counter flow with downstream half heating	58
Figure 4.10 Temperature distribution for parallel flow with upstream half heating	59
Figure 4.11 Temperature distribution for counter flow with downstream half heating	60
Figure 4.12 Increases in thermal resistance for parallel flow undergoing localized heating	61
Figure 4.13 Increases in thermal resistances for counter flow undergoing localized heating	61
Figure 4.14 Domain of computation for numerical modeling	62
Figure 4.15 Wall temperature distribution along the flow direction for counter flow with 83 ml/min total flow rate	65
Figure 4.16 Heat flux at solid-liquid interfaces in $\text{kW/m}^2$ for a total flow rate of 83 ml/min	68



Figure 4.17 Temperature contour map for the cross-sections (Z-Y plane) at different axial position, parallel flow with total flow rate 83 ml/min	69
Figure 4.18 Temperature contour map for the cross-sections at different axial positions for counter flow at a total flow rate of 83 ml/min	70
Figure 4.19 Heat flux at solid-liquid interfaces in kW/m <sup>2</sup> for a total flow rate of 300 ml/min	71
Figure 4.20 Temperature contour map for the cross-sections at different axial positions for parallel flow at a total flow rate of 300 ml/min	72
Figure 4.21 Temperature contour map for the cross-sections at different axial position, counter flow with total flow rate 300 ml/min	73
Figure 5.1 Effects of the refractive index on the object plane displacement	81
Figure 5.2 Typical velocity profile after correlating two raw image maps	83
Figure 5.3 Effects of the presence of wall boundary inside interrogation area on the velocity measurement	84
Figure 5.4 Implementation of equation (10) to extend the velocity field to the wall region	86
Figure 5.5 Velocity profile using different image processing techniques	87
Figure 5.6 Cross-section of a microchannel for Micro-PIV test	88
Figure 5.7 Velocity profile for SG34 (1 ml/hour or 0.07 m/s)	89
Figure 5.8 Velocity profile for SG34 (4 ml/hour or 0.28 m/s)	90
Figure 5.9 Velocity profile for SG53 ( 1ml/hour or 44 mm/s)	91
Figure 5.10 Velocity profile for SG103 (4 ml/hour or 88 mm/s)	92
Figure 5.11 Velocity profile for SG103 (10 ml/hour or 0.22 m/s)	92
Figure 5.12 Velocity profile development for SG103 (Re = 9.8)	94
Figure 5.13 Velocity profile developing for SG103 (Re = 25 or 0.22 m/s)	95
Figure 5.14 Pressure drop for microchannels of various dimensions	96
Figure 5.15 Velocity contour plot for cross-sections of different channels	98

Figure 5.16 Angle effects on flow characteristics	99
Figure 5.17 Effects of sidewall angle on friction losses. Pressure drop are for trapezoidal channel while friction factor ratio is the ratio between the trapezoidal and the corresponding rectangular channel with equal flow area.	100
Figure 5.18 Contour map of temperature at the cross-section of rectangular and trapezoidal channel with 5° sidewall angle for H2 boundary condition.	102
Figure 5.19 Heat transfer performance variations with sidewall angle, H2 boundary condition	103
Figure 5.20 Contour map of temperature at the cross-section of channels for conjugate heat transfer (only half of the fluid cross-section is shown). Uniform heat flux is applied at bottom of the silicon and the top surface is adiabatic.	104
Figure 5.21 Heat flux distribution along the side walls of all three channels	105

## LIST OF SYMBOLS or ABBREVIATIONS

CF11	counter flow with interlayer flow rate ratio between MC1 and MC2 set at one to one
CF12	counter flow with interlayer flow rate ratio between MC1 and MC2 set at one to two
CF21	counter flow with interlayer flow rate ratio between MC1 and MC2 set at two to one
D	Brownian motion diffusion coefficient ( $\text{m}^2/\text{s}$ )
$d_e$	effective image diameter for particles with finite size ( $10^{-6} \text{ m}$ )
$d_{e,\infty}$	effective image diameter for particles with finite size without paraxial assumption( $10^{-6} \text{ m}$ )
$d_{e,P}$	effective image diameter for particles with finite size using paraxial assumption( $10^{-6} \text{ m}$ )
$d_H$	hydraulic diameter (m)
$d_P$	diameter of the seeding particles for Micro-PIV (m)
$d_s$	diameter of the diffraction limited point response function ( $10^{-6} \text{ m}$ )
f	friction factor
$f^\#$	f-number for objective lenses
$f^\#_\infty$	f-number for objective lenses without paraxial assumptions
$f^\#_P$	f-number for objective lenses with paraxial assumptions
h	heat transfer coefficient ( $\text{W}/\text{m}^2\text{-K}$ )
$H_1$	total thickness of silicon wafer bearing MC1 (mm)
$H_2$	total thickness of silicon wafer bearing MC2 (mm)
H2	constant heat flux boundary condition

$H_{b1}$	thickness of the base region under MC1 (m)
$H_{b2}$	thickness of the base region under MC2 (m)
$H_{b3}$	effective thickness of the cover plates (m)
$H_c$	channel depth (m)
$H_{c\_SG}$	depth of the channels for Micro-PIV measurement ( $\mu\text{m}$ )
$H_{c1}$	depth of the channel MC1 (mm)
$H_{c2}$	depth of the channel MC2 (mm)
$H_t$	total thickness of the computational domain ( $\mu\text{m}$ )
$k$	thermal conductivity, (W/m-K)
$L$	overall length of the stacked microchannel structure (m)
$L_c$	channel length (m)
$L_{c1}$	length of channel MC1 (mm)
$L_{c2}$	length of channel MC2 (mm)
$L_i$	distance from water-air interface to objective plane (m)
$L_o$	distance from water-air interface to actual objects (m)
$M$	magnification of objective lenses
MC1	the first layer of microchannels from the bottom in the stack
MC12	bonded two layer stack including MC1 and MC2
MC12MN2	bonded three layer stack including MC1, MC2 and MN2
MC12MN21	bonded four layer stack including MC1, MC2, MN2 and MN1
MC12MN21PT	bonded five layer stack
MC2	the second layer of microchannels from the bottom in the stack
MN1	manifolds for the channels in MC1

MN2	manifolds for the channels in MC2
n	number of channels as in equation (1.3); refractive index as in equation (5.5)
NA	numerical aperture
Nu	Nusselt number
$Nu_{conj, bot}$	mean Nusselt number averaged over the bottom wall for conjugate heat transfer
$Nu_{conj, m}$	mean Nusselt number averaged over all peripheral walls for conjugate heat transfer
$Nu_{conj, side}$	mean Nusselt number averaged over the side wall for conjugate heat transfer
$Nu_{H2, bot}$	mean Nusselt number averaged over the bottom wall for H2 condition
$Nu_{H2, m}$	mean Nusselt number averaged over all peripheral walls for H2 condition
$Nu_{H2, side}$	mean Nusselt number averaged over the side wall for H2 condition
$Nu_{H2, top}$	mean Nusselt number averaged over the top wall for H2 condition
P1, P2, P3	three electrodes for heaters
PF11	parallel flow with interlayer flow rate ratio between MC1 and MC2 set at one to one
PF12	parallel flow with interlayer flow rate ratio between MC1 and MC2 set at one to two
PF21	parallel flow with interlayer flow rate ratio between MC1 and MC2 set at two to one
PT	fluid connection ports
Q	volumetric flow rate ( $m^3/s$ )
$Q_{input}$	Heat input (W)
Re	Reynolds number

$s_1$ through $s_9$	array of nine sensors
SG103	channel for Micro-PIV measurement with effective width at 103 microns
SG34	channel for Micro-PIV measurement with effective width at 34 microns
SG53	channel for Micro-PIV measurement with effective width at 53 microns
$s_i$	image distance (m)
$s_o$	virtual object distance (m)
$T$	absolute temperature (K)
$t$	time (s)
$T_{f,1}$	mean inlet fluid temperature for MC1 (K)
$T_{f,2}$	mean inlet fluid temperature for MC2 (K)
$u$	fluid velocity used in equation (5.1) (m/s)
$u(X,t)$	velocity in the measurement volume as a function of space and time
$u(y)$	velocity distribution along $y$ (m/s)
$u_0$	velocity at the centroid of the interrogation area (m/s)
$u_m$	mean velocity calculated in equation (5.10) (m/s)
$u_{wall}(y)$	velocity field extended to wall region as in equation (5.12) and (5.13) (m/s)
$v$	mean velocity (m/s)
$V_1$	mean inlet velocity for MC1 (m/s)
$V_2$	mean inlet velocity for MC2 (m/s)
$W$	overall width of the stacked microchannel structure (m)
$W(X)$	weighting function
$W_c$	channel width (m)

$W_{c1}$	width at the bottom of the channels in MC1 (mm)
$W_{c1\_SG}$	width at the bottom of the channels for Micro-PIV measurement ( $\mu\text{m}$ )
$W_{c2}$	width at the top of the channel MC1 (mm)
$W_{c2\_SG}$	width at the top of the channels for Micro-PIV measurement ( $\mu\text{m}$ )
$W_{c3}$	width at the bottom of the channel MC2 (mm)
$W_{c4}$	width at the top of the channel MC2 (mm)
$W_f$	fin width (m)
$W_u$	width of a unit cell including two halves of the fin width and one channel width (mm)
$x$	coordinates along the main flow direction
$x^+$	dimensionless distance from the inlet
$\mathbf{X}$	3-D space coordinates vector
$y$	coordinates along the channel width direction
$y_0$	y coordinates at the centroid of the interrogation area
$y_i$	y coordinates at the boundary interfaces
$z$	coordinates along the channel depth direction
$z_{\max}$	z coordinates of the plane with maximum velocity

### Greek Symbols

$\Delta P$	pressure drop (pa)
$\delta t$	time interval between laser pulse 1 and laser pulse 2 ( $\mu\text{s}$ )
$\delta z_{\text{corr}}$	depth of correlation as in equation (5.7) ( $\mu\text{m}$ )
$\delta z_{\text{corr,P}}$	depth of correlation with paraxial assumption ( $\mu\text{m}$ )
$\delta z_{\text{corr},\infty}$	depth of correlation without paraxial assumption ( $\mu\text{m}$ )

$\delta z_m$	depth of measurement as in equation (5.6) ( $\mu\text{m}$ )
$\varepsilon_B$	relative error in velocity due to Brownian motion
$\kappa$	Boltzman coefficient
$\lambda$	wave length (nm)
$\mu$	dynamic viscosity (kg/m-s)
$\theta$	thermal resistance (K/W)
$\theta_1$	thermal resistance for single layer microchannel (K/W)
$\theta_a$	refractive angle in air (degree)
$\theta_w$	incident angle in water (degree)
$\rho$	density ( $\text{kg/m}^3$ )
$\frac{\partial u}{\partial y} _{y_0}$	derivative of velocity at the centroid of the interrogation area as in equation (5.11) (1/s)
$\frac{\partial^2 u}{\partial y^2} _{y_0}$	second Derivative at the centroid of the interrogation area of velocity as in equation (5.11) (1/s)



## SUMMARY

A stacked microchannel heat sink was developed to provide efficient cooling for microelectronics devices at a relatively low pressure drop while maintaining chip temperature uniformity. Microfabrication techniques were employed to fabricate the stacked microchannel structure, experiments were conducted to study its thermal performance. A total thermal resistance of less than 0.1 K/W was demonstrated for both counter flow and parallel flow configurations. The effects of flow direction and interlayer flow rate ratio were investigated. It was found for the low flow rate range that the parallel flow arrangement results in a better overall thermal performance than counter flow arrangement; whereas, for the large flow rate range, the total thermal resistances for both the counter flow and parallel flow configurations are indistinguishable. On the other hand, the counter flow arrangement provides better temperature uniformity for the entire flow rate range tested. The effects of localized heating on the overall thermal performance were examined by selectively applying electrical power to the heaters. Numerical simulations were conducted to study the conjugate heat transfer inside the stacked microchannels. Negative heat flux conditions were found near the outlets of the microchannels for the counter flow arrangement. This is particularly evident for small flow rates. The numerical results clearly explain why the total thermal resistance for counter flow arrangement is larger than that for the parallel flow at low flow rates.

In addition, laminar flow inside the microchannels were characterized using Micro-PIV techniques. Microchannels of different width were fabricated in silicon, the smallest channel measuring 34  $\mu\text{m}$  in width. Measurements were conducted at various

channel depths. Measured velocity profiles at these depths were found to be in reasonable agreement with laminar flow theory. An interesting result from Micro-PIV measurement is that the maximum velocity is not located at the midplane of the channel depth but shifts significantly towards the top of the microchannels. This is due to the slight sidewall slope, a common issue faced with DRIE etching. Numerical simulations were conducted to investigate the effects of the sidewall slope on the flow and heat transfer. The results show that the effects of large sidewall slope on heat transfer are significant; whereas the effects on pressure drop are not as pronounced.

# **CHAPTER 1**

## **INTRODUCTION**

The ever-growing demand for functionality and performance in microprocessors causes continuous increases in the number of transistors integrated per chip and the operating frequency and decreases in feature size. As a result, the total amount of heat generated and the heat flux have increased tremendously over the past decades and are predicted to so for many years to come [1]. It is of vital importance to dissipate the heat from the active circuits to the environment while maintaining an acceptable junction temperature in order to maintain the reliability and performance of the devices.

Typically cooling of microprocessors are performed by attaching a heat sink with an integrated fan. To assess the effectiveness of the cooling solution the term thermal resistance is introduced. It is defined as the maximum temperature difference normalized by the total power dissipation. The temperature difference between the hot junction and the ambient air is usually used. It is generally agreed that air cooling technology is approaching its limit as the thermal management becomes increasingly demanding. As predicted by the ITRS roadmap [1], the thermal resistance from the junction to ambient for high performance microprocessors has to be reduced from 0.46 °C/W for the year 2001 to 0.18 °C/W for the year 2010. On the other hand the available space for thermal management devices shrinks with the system size. Clearly, a shift from air cooling technology to liquid cooling technology is necessary to meet these challenges in the future.

## 1.1 Motivation

One of the promising liquid cooling techniques is to attach a microchannel heat sink to, or directly fabricate microchannels on, the inactive side of the chip. Usually in a closed-loop arrangement, coolant such as water is pumped through the microchannels to take away the heat generation. In fully developed laminar flow, the non-dimensional Nusselt number is constant. Thus the heat transfer coefficient is inversely proportional to the hydraulic diameter, as shown in Equation (1.1).

$$Nu = \frac{h \cdot d_H}{k} = const \Rightarrow h \propto \frac{1}{d_H} \quad (1.1)$$

In an early work by Tuckerman and Pease [2], a silicon microchannel heat sink containing parallel micro flow passages 50  $\mu\text{m}$  wide and 302  $\mu\text{m}$  deep was experimentally demonstrated to have a very low thermal resistance (as low as  $9 \times 10^{-6}$  K/(W/m<sup>2</sup>)). This resistance is substantially lower than that of conventional heat sinks.

Microchannel heat sinks can be fabricated using the micromachining techniques that have been used for IC fabrication. This makes batch production possible and thus potentially reduces the fabrication cost. Since the microchannel heat sink is much smaller than an air cooled heat sink, the mechanical load on the chip is significantly reduced. However, several issues must be addressed in order to implement the microchannel cooling technique for the thermal management of microelectronics. Firstly the pressure drop due to flow friction in the microchannel is very large. For fully developed laminar flow, the Poiseuille number (the product of the friction factor and the Reynolds number) is constant. The pressure drop due to friction is thus determined by

$$\Delta P = 4f \frac{L}{d_H} \frac{\rho v^2}{2} = 2f \text{Re} \frac{L}{d_H^2} \nu \mu \quad (1.2)$$

For rectangular channels, the hydraulic diameter is defined as  $d_H = \frac{2W_c H_c}{W_c + H_c}$ .

Velocity is determined by dividing the volumetric flow rate  $Q$  by the total flow area as shown in Equation (1.3).

$$v = \frac{Q}{n \cdot W_c \cdot H_c} \quad (1.3)$$

Substituting the equations for hydraulic diameter and velocity into (1.2) produces

$$\frac{\Delta P}{L_c} = \frac{1}{2} f \text{Re} \frac{1}{H_c} \frac{\mu \cdot Q \cdot (1 + W_c / H_c)^2}{n \cdot W_c^3} \quad (1.4)$$

Clearly, the pressure drop is proportional to  $\frac{1}{n \cdot H_c \cdot W_c^3}$  if  $W_c/H_c$  is negligible. If

the flow rate  $Q$  and the number of channels  $n$  are fixed, the pressure drop increases dramatically as the channel size shrinks.

A stacked microchannel heat sink [3] addresses this issue by increasing  $n$ , the number of channels while keeping  $Q$  constant. As can be seen from Figure 1.1 (a), compared with single-layered microchannel, stacked microchannel drastically reduces the pressure drop. Results from a simple resistance network model, as shown in Figure 1.1 (b), indicate that thermal resistance is not very sensitive to the number of layers. Two competing effects result in the trend in Figure 1.1 (b). One is that the total available heat transfer area increases as the number of layers increases. The other is that fin efficiency decreases significantly as more microchannels are stacked on-top. Effectively the fluid flowing in the top layers does not contribute to the cooling as effective as that flowing in the microchannels in the bottom layer.

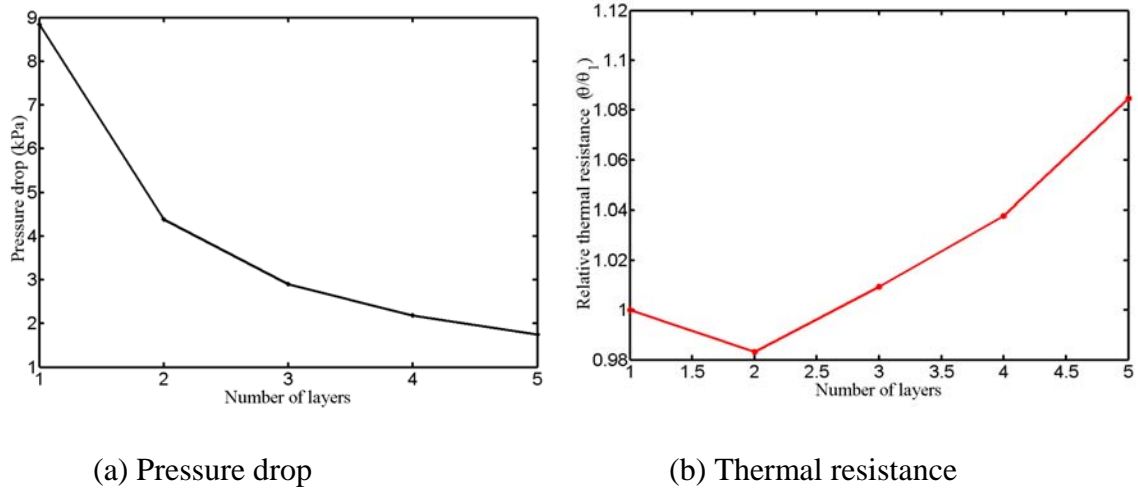


Figure 1.1 Comparison of pressure drop and thermal resistance for different number of layers at fixed flow rate ( $0.83 \times 10^{-6} \text{ m}^3/\text{s}$  or 50 ml/min)

Another issue associated with any single phase cooling technique, is the temperature non-uniformity in the chip being cooled. Along the flow direction, the coolant temperature rises as a result of the heat input. At the same time the heat transfer coefficients decrease along the flow direction due to the growing boundary layer thickness. In the entrance region heat transfer coefficient is extremely high due to the very thin local boundary layer [4]. It decreases asymptotically to the fully developed value if the channel is sufficiently long. Non-uniformity in temperature is often undesirable for several reasons. Firstly, the spatial temperature gradient may adversely affect the performance and reliability of electronic devices. For instance, spatial temperature gradient in interconnects can produce an atomic flux divergence or gradient which results in electromigration damages to the metal traces on the chip. Studies have revealed that void formation occurs in regions where the electron flow is in the direction of increasing temperature, and hillocks form in locations where the electron flow is in the

direction of decreasing temperature [5]. Secondly, large temperature non-uniformity can cause additional thermal stresses in the die which pose potential reliability concerns to the devices.

In an optimization study, Bau [6] found that reducing the cross-sectional area along the flow direction could dramatically reduce temperature non-uniformity; however, because of flow acceleration, the pressure drop increases considerably.

There exists a need to develop microchannel heat sinks that have not only low overall thermal resistance but also less pressure drop and better temperature uniformity. In the current study, a stacked microchannel structure was developed that consists of two layers of microchannels, two layers of manifolds for fluid distribution and one layer of fluid connection ports. Compared with single-layered microchannels, the pressure drop across the microchannels are significantly reduced due to the increases of total flow area for the same flow rate. A flexible design of fluid distribution allows either parallel or counter flow arrangement. The counter flow arrangement can be applied to reduce the chip temperature non-uniformity by pumping fluid flow in opposite directions on adjacent layers. The stacked microchannel structure was fabricated using microfabrication techniques. Thermal performance of this thermal management device was both experimentally and numerically studied.

## 1.2 Literature Review on Microchannels

### 1.2.1 Review of concepts

Microchannel heat sink was first proposed for heat sinking of very large scale integrated (VLSI) electronic components in 1980s. Tuckerman and Pease [2] and Tuckerman [7] reported a microchannel heat sink, consisting of parallel micro flow passages 50  $\mu\text{m}$  wide and 302  $\mu\text{m}$  deep, which was demonstrated to have thermal resistance as low as  $9 \times 10^{-6} \text{ K}/(\text{W}/\text{m}^2)$  for a pumping power of 1.84 W. At a heat flux of  $790 \text{ W}/\text{cm}^2$ , this corresponds to a maximum temperature difference of  $71^\circ\text{C}$ . This work is considered as a milestone in the development of micro-scale heat sinks; however, typical pressure drop for these microchannels is more than two bars. Meanwhile the surface temperature rises due to caloric heating along the flow direction is also very large which is highly undesirable from the performance and reliability point of view.

Manifold microchannel heat sinks were first suggested in Harpole and Eninger [8] and numerically studied by Copeland et al. [9] and Ng and Poh [10]. Compared to conventional microchannel heat sinks, manifold microchannel heat sinks feature many inlet and outlet manifolds, alternating at a periodic distance along the length of the microchannels. Coolant flows from the inlet port into the manifolds and forms separate streams. Each stream flows through a short section of microchannels. If fully developed laminar flow and fixed flow rate are assumed, at, the pressure drop is reduced by a factor equal to the number of manifold inlet/outlet compared with conventional microchannel heat sink. On the other hand, the same temperature variation exists for manifold microchannels in a much shorter distance. There are also concerns of the heat transfer efficiency for the region underneath the manifolds.



Assuming fully developed conditions, Bau [6] conducted an optimization study to minimize the temperature gradient and the maximum temperature for microchannel heat sink. It was demonstrated that further reductions in maximum temperature and temperature gradient could be achieved by varying the cross-sectional dimensions of the microchannel. The penalty of this method is the dramatically increased pressure drop due to the acceleration along the flow direction.

Vafai and Zhu [11] numerically investigated a two-layered microchannel heat sink with counter-current flow arrangement. It was found that counter-flow arrangement reduces the temperature gradient dramatically compared with single-layered microchannel for  $Re = 143.6$ .

Stacked microchannel heat sinks was discussed in Wei and Joshi [3]. By stacking several layers of microchannels, the total available flow area increases. For fixed flow rate, the pressure drop is reduced by a factor almost equal to the number of layers. The thermal performance of the stacked microchannel heat sink is affected by the channel aspect ratio, the thermal conductivity of the base material and the flow rate. A simple thermal-resistance-network analysis found that at fixed pumping power conditions the overall thermal resistance for a two-layered microchannel is 30% less than that of a single-layered microchannel. Stacked microchannels provide flexibility to engineer the microchannel dimensions on different layers and to adjust the flow directions and interlayer flow rate ratios for different power map of microprocessors.

### 1.2.2 Review of experimental studies

Following the work of Tuckerman and Pease [2], many studies have been performed to characterize flow and heat transfer in microchannel structures. Friction factor and Nusselt number are the two primary parameters examined in most of the experimental literature. Several studies [12-20] indicated that these two parameters deviate from the classical theory developed for macro-size channels and the transition from laminar to turbulent flow occurs at a smaller critical Reynolds number. Unfortunately there is no consensus on the trend of this deviation among different researchers. For instance, Wu and Little [12] performed tests for flow of gas in trapezoidal microchannels and found the friction factor for laminar flow in microchannel to be generally larger than predicted by the Moody diagram and to be affected by surface roughness. Pfahler et al. [13] however found the friction factor for microchannels to be smaller than predicted by laminar theory.

The reported deviations were attributed to different sources such as micro-rotational effects of the molecules (Papautsky et al. [16]), flow maldistribution in the manifolds (Harms [17]), surface roughness (Mala and Li [18]), electric double layer (Mala et al. [19]) and viscous heating (Tso and Mahulikar [20]).

In contrast Xu et al. [21] reported that flow characteristics in microchannels with hydraulic diameter of 30 to 344  $\mu\text{m}$  at Reynolds numbers of 20 to 4000 agree with predictions based on the Navier-Stokes equation. Liu and Garimella [22] showed that conventional correlations offer reliable predictions for laminar flow characteristics in microchannels over a hydraulic diameter range of 244 to 974  $\mu\text{m}$ .

Recently Lee and Garimella [23] investigated heat transfer in microchannels made of copper for a Reynolds number range of 300 to 3500. The widths of the studied channels range from 194  $\mu\text{m}$  to 534  $\mu\text{m}$  while the depths are five times the widths. In deducing the average Nusselt number, an average wall temperature based on a one-dimensional conduction model was used. For laminar flow the measured Nusselt number agreed with predictions for thermally developing flow over the entire length of the channel.

Baviere et al. [24] studied flow inside smooth and rough microchannels with height range of 7  $\mu\text{m}$  to 300  $\mu\text{m}$  and Reynolds number range of 0.01 to 8000. In the smooth wall case the result of friction factor was well predicted by theory. For the rough wall case, an artificial surface roughness was added to the sidewalls of the smooth microchannels and the measured friction loss was significantly larger but no earlier transition to turbulence was observed.

In typical flow experiments, the pressure drop was measured across plenums at the end of the microchannels. This bulk property is usually lumped with other hydraulic losses such as header loss, entrance effects and uncertainties due to the various factors mentioned in the previous research work. This made it difficult to interpret the experimental data and to compare results among different researchers.

### 1.2.3 Review of analytical studies

Modeling of transport in microchannels can be divided into two categories. In the first, methods used for macro-scale channels are directly implemented to evaluate the performance of microchannel heat sinks. In the second category, new effects are taken

into account to explain the deviation of the measured results from classical theory. The former range from simple 1-D models (Phillips [25]; Knight et al. [26]) to three-dimensional conjugate studies (Weisberg and Bau [27], Yin and Bau [28], Fedorov and Viskanta [4]). The latter consider effects such as surface roughness [18], electric double layer (EDL) [19] and micro-rotation of molecules [16]. However, existing analytical studies are still inconclusive.

#### 1.2.4 Review of Micro Particle Image Velocimetry study for microchannel flow

Particle Image Velocimetry (PIV) is a well established non-intrusive measurement technique that is capable of simultaneously mapping the velocity field over an area defined by the field of view. In a typical PIV implementation (Adrian, [29]), the flow field to be measured is seeded with flow-tracing particles. These particles are illuminated with either a pulsed light source or a continuous light source gated by a camera shutter. The images of the particles are taken at two known times. The displacement of the particle image is then statistically determined by correlation techniques. In order to resolve the flow field inside microchannels, a Micro PIV technique is required to achieve spatial resolution on the order of several microns.

Evolved from PIV, Micro-PIV incorporates an additional microscope to resolve the small flow field. Depending on the dimensions of the channel, sub-micron particles are typically used. As the particle size is very close to the illuminating light wavelength, it is necessary to use inelastic scattering techniques for imaging. For applications where water is the fluid polystyrene particles coated with fluorescent dyes can be used as they have similar density as water. These epi-fluorescent particles are excited by an incident

monochromatic light and emit light at longer wavelength. A long-pass filter will allow only the emitted light from the particles to reach the camera. Compared with PIV, Micro-PIV can be distinguished by the illumination method. Volume illumination is necessary for Micro-PIV as optical access is usually limited in one direction and it is also very difficult to produce thin light sheet of a few microns. Consequently, velocity measured using Micro-PIV is essentially averaged over a certain volume.

The first implementation of Micro-PIV was reported in Santiago et al. [30] where an epi-fluorescent microscope was with a continuous Hg-arc lamp and a CCD camera to record the flow around a nominally 30  $\mu\text{m}$  elliptical cylinder in a Hele-Shaw flow cell. The flow was traced with 300 nm diameter polystyrene particles coated with fluorescent dyes. The resolution of this system was reported to be 6.9  $\mu\text{m} \times 6.9 \mu\text{m} \times 1.5 \mu\text{m}$ . As the flow is very slow and the particles are small, Brownian motion effects are considered to be large. In this experiment the time delay between image exposures was controlled through the camera shutter. This limits the application of such a system to relatively low velocities.

Meinhart et al. [31] measured velocity distribution in a microchannel 30  $\mu\text{m}$  deep and 300  $\mu\text{m}$  wide. The microchannels were fabricated in a glass substrate. A 5 ns pulsed Nd: YAG laser was used as the light source to illuminate the 200 nm diameter fluorescent particles. The images of the flow field were recorded using a 1300  $\times$  1030  $\times$  12 bit CCD camera. The streamwise velocity profile estimated from the PIV measurements on one plane agrees within 2% with analytical results. A similar system was used in Meinhart and Zhang [32] to measure the transient flow inside a micro-fabricated inkjet printhead. The measurement domain was a converging area near the exit nozzle of the printhead and

the width of the nozzle was about 60  $\mu\text{m}$ . For the inkjet printhead studied, four distinct regions of the ejection cycle were identified: infusion, inversion, ejection and relaxation.

Sharp et al. [33] employed Micro-PIV techniques to study transition to turbulence in microtubes with a range of diameter from 184  $\mu\text{m}$  to 242  $\mu\text{m}$ . The measured centerline velocity was compared with predictions to identify the possible transition to turbulence. Zeighami et al. [34] studied the transition to turbulence in rectangular microchannels with a depth of 150  $\mu\text{m}$  and width of 100  $\mu\text{m}$ . Instantaneous vectors of velocity were obtained for different Reynolds numbers by Micro-PIV measurement. At a Reynolds number of 1600 temporally fluctuating asymmetric velocity was observed, and this was identified as the transition.

As mentioned earlier, the implementation of Micro-PIV requires that the entire flow volume be illuminated. The measured velocity is a volume average as particles out of focus also contribute to the correlation function. It is very important to quantify the effects of these out-of-focus particles. Meinhart et al. [35] defined the depth of measurement as the thickness beyond which the image intensity of the out-of-focused particles is less than a tenth of the intensity of those particles in-focus. An equation was proposed to estimate the depth of measurement considering the effects of the diffraction limit, geometric limit and the limited particle size.

Olsen and Adrian [36] derived an analytical model to quantify the effects of the out-of-focused particles on the image visibility and the correlation function. A weighting function was derived to take into account of the contributions of the out-of-focused particles to the correlation function at different depths. A depth of correlation was defined beyond which the weighting function is 1% of the particles in focus. The same

weighting function based on the curvature of the correlation functions was derived in Bourdon et al. [37]. These models were validated through computations and physical experiments.

Olsen and Bourdon [38] further considered the effects of the out-of-plane motion on the depth of correlation. It was found that out-of-plane motion would increase the depth of correlation by a factor larger than the traverse distance traveled by the particles during the time intervals between two laser pulses.

For applications with low velocities and small seeding particles, the effects of Brownian motion may be important. Olsen and Adrian [39] incorporated the Brownian motion effects into the same weighting function as defined in their previous model. It was subsequently shown that the depth of correlation was increased by a factor that is determined by the time intervals and the particle size.

Devasenathipathy et al. [40] applied particle imaging velocimetry and particle tracking velocimetry to measure flow velocity inside a straight rectangular channels fabricated in Silicon ( $100\text{ }\mu\text{m} \times 100\text{ }\mu\text{m}$ ) and a D-shaped channel fabricated in Acrylic. The effects of three-dimensional Brownian motion on the plane velocity measurement were discussed.

Liu et al. [41] demonstrated an Infrared micro-particle image velocimetry for silicon-based devices by measuring flow inside a  $255\text{ }\mu\text{m}$  capillary tube. A silicon wafer was placed between the incident laser beam (wavelength  $1.35\text{ }\mu\text{m}$ ) and the capillary tube to simulate transmission through silicon. Polystyrene particles of  $1.5\text{ }\mu\text{m}$  diameter without fluorescent coatings were used in the experiment. A NIR camera with  $30\text{ }\mu\text{m}$

pixel size was used to record the IR image of the seeding particles. The reported measurement depth was about 35  $\mu\text{m}$ .

Micro Particle Imaging Velocimetry (Micro-PIV) technique has been an active research topic of many studies. Most of the work reported focused on demonstrating the technique through measuring relatively slow velocity field in large channels or tubes [Park et al. 42].

In the current study, the velocity profiles were directly measured using the micro particle image velocimetry ( $\mu$ -PIV) for microchannels 34  $\mu\text{m}$  to 103  $\mu\text{m}$  wide. The whole flow field was resolved by scanning through the depth of the channel. The measured velocity profile for different focal planes were compared with the predicted results from laminar theory for rectangular and trapezoidal channels respectively. This work also measured the hydrodynamic entrance length for microchannels. To the best of the author's knowledge no other work has been reported on Micro-PIV measurement of velocity profiles inside channels of less than 35  $\mu\text{m}$  wide. The measurement of flow developing length using Micro-PIV for microchannels also appears to be the first ever effort.

### **1.3 Objectives**

This study aims at developing microchannel heat sinks that have not only high heat transfer coefficient but also low pressure drop penalty and good temperature uniformity. The main objectives of the current work are listed below.

- a) Design and fabricate the stacked microchannel heat sink.



- b) Evaluate thermal performance of the stacked microchannel heat sink for parallel and counter flow arrangement.
- c) Investigate the conjugate heat transfer for both parallel and counter flow microchannel heat sinks.
- d) Fundamental study of flow characteristics inside single microchannels by directly measuring the velocity profile inside the channel using Micro-PIV technique

#### **1.4 Overview of the current study**

Microchannel liquid cooling technique has emerged as an efficient thermal management technique for microelectronics as the requirement of cooling is moving beyond the limit of conventional air cooling technique. The present study aims at developing stacked microchannel heat sinks for high-end microelectronics with considerations on both application aspects and fundamental aspects.

Chapter 2 describes the experimental setup and procedures for both heat transfer study and Micro-PIV test. Details about test facility and the test modules are included. Experimental procedures and measurement uncertainties are discussed.

Chapter 3 details the micro-fabrication techniques used to fabricate the test structure. Effects of aspect ratio on the side wall profile produced in a standard Bosch process are discussed. Detailed steps on silicon-silicon direct bonding are described.

Chapter 4 examines the thermal performance of the fabricated stacked microchannel heat sink with either parallel flow or counter flow. Effects of interlayer flow rate ratio are discussed. Conjugate heat transfer inside stacked microchannels are numerically investigated to understand the thermal performance results.

Chapter 5 investigates the flow characteristics inside microchannels of different widths using Micro-PIV technique. Effects of the sidewall angle due to fabrication defects on flow and heat transfer are examined numerically.

Chapter 6 summarizes the study and makes recommendations for future work.

## **CHAPTER 2**

### **EXPERIMENTAL SETUP AND PROCEDURES**

Two sets of experiments were conducted in this study. The first set focused on the heat transfer characteristics of the stacked microchannel structure. Thermal performance of the stacked microchannel heat sink was evaluated in a single-phase close-loop. The second set aimed at measuring the velocity field inside microchannels directly. A whole field measurement technique called Micro Particle Image Velocimetry (Micro-PIV) was employed to measure the flow inside microchannels. Micro-PIV is a non-intrusive technique suitable for applications where the presence of even micro-scale probes would disturb the flow field. The purpose of the PIV measurement was to examine the validity of the laminar theory for micro-scale channels. The following sections detail the experimental setup and procedures for these measurements.

#### **2.1 Experimental setup for heat transfer study**

A schematic of the experimental setup is shown in Figure 2.1. A miniature diaphragm-pump drives de-ionized (DI) water from the reservoir through 8  $\mu\text{m}$  filters and flow meters to the test module. The cold DI water picks up the heat from the microchannel heat sink and passes through a liquid-liquid heat exchanger and rejects the heat to a recirculating chiller. A bypass loop is used to adjust the system flow rate and pressure. Two needle valves were used to control the flow rate to both flow meters. Two differential-pressure transducers were used to monitor the pressure drops across the test modules.

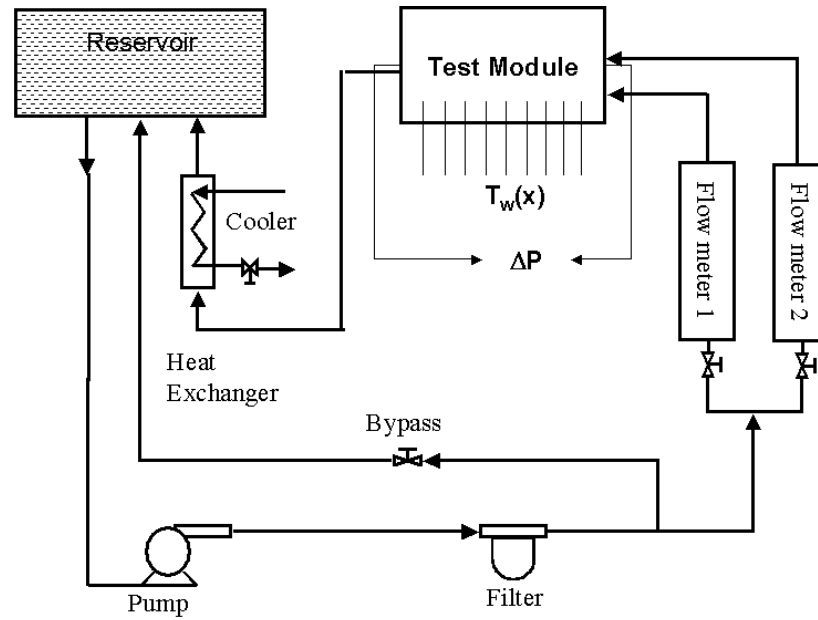


Figure 2.1 Schematic of the test flow loop

### 2.1.1 Test module

The test module, illustrated in Figure 2.2, consists of five layers of silicon plates. Two microchannel layers at the bottom provide the cooling. Two manifold layers above the microchannel layers distribute the fluid. The fifth layer with inlet and outlet ports is for fluid connection. The microchannels, manifolds and inlet-outlet ports were all fabricated using the deep reactive ion etching (DRIE) technique. The dimensions of the two layers of microchannels are shown in Figure 2.3 and Table 2.1. Although rectangular channels can also be fabricated by orientation dependent wet etching technique, manifolds and round inlet-outlet ports can only be etched in DRIE.

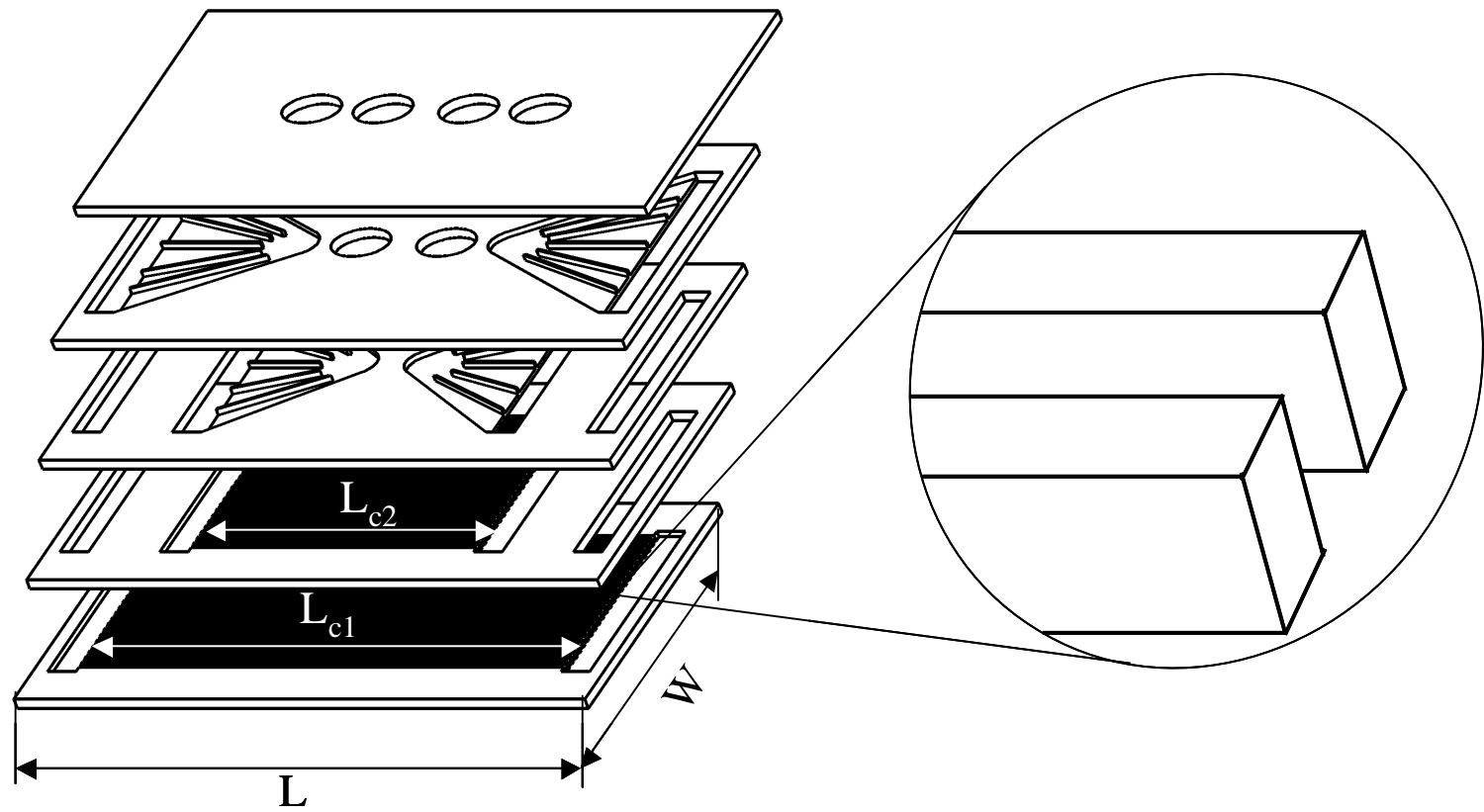


Figure 2.2 Schematic of the stacked microchannel test module

Table 2.1 Microchannel dimensions (mm)

$L_{c1}$	$L_{c2}$	$W_u$	$W_{c1}$	$W_{c2}$	$W_{c3}$
18	10	0.1	0.056	0.054	0.061
$W_{c4}$	$H_{c1}$	$H_{c2}$	$H_1$	$H_2$	
0.053	0.284	0.243	0.48	0.48	

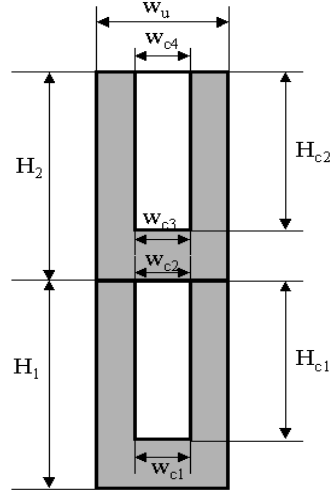


Figure 2.3 Dimensions of stacked microchannels

The five layers of silicon plates populated with respective features were bonded into a watertight stack through silicon-silicon direct bonding. Two separate flow networks were formed, as shown in Figure 2.4. Both flow rate and flow direction into these two networks can be controlled to achieve either parallel flow or counter-flow configuration.

Platinum heaters and resistive temperature sensors were deposited on the backside of the structure shown in Figure 2.4 to provide heating and temperature sensing respectively. Figure 2.5 shows a layout of the thin film heaters and sensors. The coarse lines are for heaters while the fine lines are for resistive temperature sensors. The heaters can be connected in three ways. Uniform heating is achieved if one terminal of the DC

power is connected to P2 while the other terminal is connected to both P1 and P3. Partial heating is achieved if only either of P1 and P3 is connected. An array of nine sensors measured the temperature distribution along the flow direction by measuring the resistances. The temperature sensors were calibrated to generate the calibration curve for the temperature measurement.

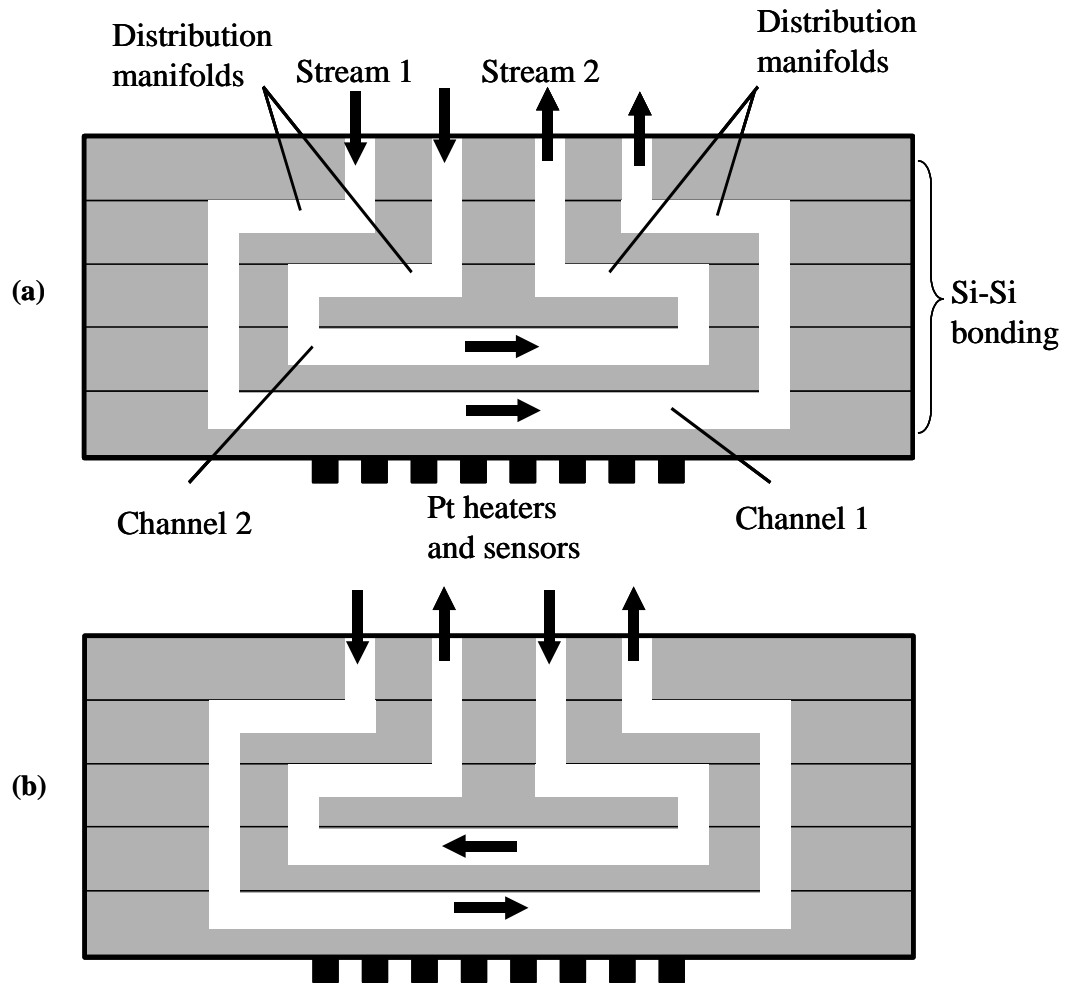


Figure 2.4 Schematic of the bonded prototype (a) Parallel flow arrangement (b) Counter flow arrangement

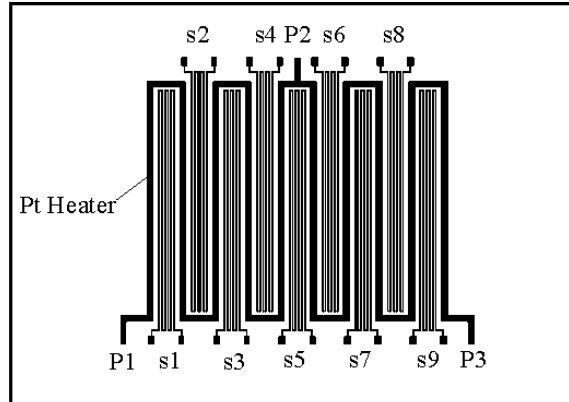


Figure 2.5 Thin film heaters and nine resistive temperature sensors (s1 to s9)

### 2.1.2 Test facilities

In this study, an Agilent DC power supply with the range of 0-100 V and 0-1 A is used to provide the heating. A Lytron liquid-liquid heat exchanger was used to cool the hot water from the microchannel heat sink. With one side connected to a Lauda recirculating chiller, the liquid-liquid heat exchanger was able to maintain the inlet temperature of the microchannels to be around 21 °C. This inlet temperature was selected according to the requirement of other instruments connected in the loop. A commercially available miniature pump from HARGRAVES was used to pump the DI water from a reservoir. The diaphragm pump has an overall dimension of 0.4" x 2" x 3". At 30 psi the miniature pump can deliver flow rate up to 300 ml/min.

For flow rate measurement, two types of flow meters were explored. A turbine flow meter with digital output is very convenient for data acquisition. Unfortunately, it was found that the output signal was very sensitive to the pressure which may be due to the deformations in the housing of the sensing unit. The accuracy of the measurement was also affected by air entrapped. A rotameter was found less sensitive to pressure. As



it was installed vertically, the effects of air-bubble are minimal. Therefore, rotameters with different ranges were eventually used for the experiments. The pressure drop was monitored using a diaphragm differential pressure transducer. The pressure transducer has an adjustable range of 0-17 psi to 0-100 psi. The output current signal was converted to voltage signal through a precision resistor.

The inlet and outlet water temperatures were measured using T-type thermocouples. These thermocouples were inserted into T-fittings mounted immediately before the inlet and after the outlet tubings. The actual power input to the chip was determined by measuring the current through, and the voltage across, the heaters.

The temperature, resistance, pressure, current and voltage signals were collected using an Agilent 34970a data acquisition unit with two 34901A Multiplexers. The data were eventually transferred to a PC through a GPIB interface card.

## **2.2 Test matrix and procedures for heat transfer experiments**

A list of controlling parameters are shown in Table 2.2. As mentioned in section 2.1.1, the heaters were connected such that three different heating map can be generated. In addition to a regular full heating, partial heating can be applied either on the upstream surface or the downstream surface. Here upstream and downstream are with respect to the flow direction in the first microchannel layer from the bottom (MC1). Although the actual CPU power map is neither uniform nor simply distributed over half of the chip area, the current experimental study does illustrate how the thermal performance of the stacked microchannel change with the power map. The flow direction inside each microchannel layer can be configured such that either parallel flow or counter flow

materialize. For a fixed overall flow rate, experiments were conducted for three different interlayer flow rate ratios.

Table 2.2 Testing matrix

Parameters	Value
Heating area	Full (1 cm x 1cm); Upstream (0.5 cm x 1 cm); Downstream (0.5 cm x 1 cm)
Flow direction	Parallel flow; Counter flow
Flow rate ratio between microchannel layer 1 (MC1) and layer 2 (MC2)	1:1; 2:1; 1:2

A typical test run starts from a degassing process. The trapped air was removed from the loop by running the system continuously for about one hour. The tested microchannel structure was located at the lowest point of the loop such that air-bubble is unlikely to be trapped. A later visualization for PIV measurement also confirmed that there was no air trapped inside microchannel. Air was also vented from the pressure transducer venting ports.

In the current experiments, the overall flow rate ranges from about 83 ml/min to 350 ml/min. For each flow rate, the power input was increased from zero to the maximum output available from the DC power supply used. The DC power supply has a limit of 100 V and 1 A. As the characteristic resistance was around 140  $\Omega$ , the maximum power input was around 70 W. For the half heating case, the maximum power input was around 35 W.

For each test run, the temperature and pressure drop were closely monitored. After about 30 minutes steady state was identified and data was sampled continuously for

one minute at one Hertz. After each test, an in-situ flow rate calibration was performed by collecting and weighting the DI water for certain amount of time.

### **2.3 Uncertainty analysis**

The inlet and outlet water temperature were measured using T-type thermocouples. The thermocouples and the data acquisition system were calibrated against a precision mercury thermometer at ice point to an uncertainty of  $\pm 0.2$  °C.

The wall temperature distributions were measured using the thin film resistive temperature sensors. Nine sensors were calibrated against a calibrated thermocouple attached to the chip surface in a convective oven. Resistance values of these sensors were recorded for each temperature setting. Very good linearity was observed.

Error sources for the wall temperature measurement include the calibration uncertainty due to the thermocouple and uncertainties due to curve fitting. The latter is estimated to be within  $\pm 0.4$  °C. Combining these effects gives an uncertainty of  $\pm 0.41$  °C.

The power dissipation is determined from the product of the voltage and current measured at the heaters. Uncertainties for direct voltage measurement are negligible. In this experiment, voltage input for the heaters were measured across the heater and the current meter with  $0.1 \Omega$  shunt resistance. For the current settings we have, this will cause 0.1 volts loss in the actual heaters. For a 70 volts case, this results in  $\pm 0.14\%$  uncertainty in voltage measurement. The current measurement has  $\pm 0.1\%$  uncertainty as indicated by the product manual. These uncertainties cause a  $\pm 0.2\%$  in power input measurement.

It is noted here that actual heat input may be less than measured value due to the losses to the environment. It was found that the power input measured agreed within 5% of the heat transferred to water.

Combining the uncertainties in temperature measurement and heat dissipation gives the uncertainties of thermal resistances at around 5%.

As for flow rate measurement, all the measurements were taken at calibration points. Therefore, no data reduction errors were introduced. The bias error due to calibration was estimated to be  $\pm 1\%$ . The bias error due to reading is  $\pm 0.75$  ml for all the readings. Therefore for flow rate of 50 ml/min, this is  $\pm 1.5\%$ . Combining these errors produces an uncertainty of  $\pm 1.8\%$  for 50 ml/min.

The channel dimensions were measured at 40 locations across the microchannels area using microscope for width measurement and Wyko optical profilometer for depth measurement. The uncertainty due to the microscope width measurement is estimated to be  $\pm 0.5$   $\mu\text{m}$ . The data scattering in width is around  $\pm 3\%$ . For depth measurement, the calibration uncertainty for the Wyko profilometer is  $\pm 0.85\%$ . The depth scattering uncertainty is estimated to be  $\pm 3\%$ . The combined uncertainty for hydraulic diameter is  $\pm 4.4\%$ .

## 2.4 Experimental setup for Micro-PIV measurement

Velocities inside microchannels were measured using Micro Particle Image Velocimetry technique (Micro-PIV). A schematic of the Micro-PIV system commercially available from DANTEC is shown in Figure 2.6. The imaging system includes an Epi-fluorescent inverted microscope (Nikon Eclipse TE2000-S), dual Nd: YAG lasers (Gemini PIV 200) and a cooled interline CCD camera. The Epi-fluorescent filter cube consists of an excitation filter, a dichromatic mirror and an emission filter. The pulsed green light from the dual lasers expands through a beam expander and pass through the diffuser and the excitation filter and the dichromatic mirror to the microscope objectives. Fluorescent particles (Nile Red, Molecular Probe) excited by this incident green light emits red light peaked around 560 nm. The emitted red light passes through the long pass emission filter to reach the CCD camera, which operates in the double-frame single exposure mode. Scattered green light from the background and ambient is blocked at the emission filter. Figure 2.7 shows the timing for the CCD camera and the laser. During the first laser pulse, the particle position is recorded in the CCD frame 1. This image is immediately transferred from the light-sensitive pixels in the CCD chip to the interline shift register. The second pulse is then fired after a pre-defined interval to record the particle position for the second frame. The laser has a pulse width of 3-5 ns and the time interval between the two lasers pulses is tunable from 0.2  $\mu$ s to 110 ms. However since the frame readout event is sequential the maximum measurement rate is no faster than 4.5 Hz.

A syringe pump ranging 0-10 ml/hour was used to deliver the seeded solutions to microchannels. The test microchannel module has microchannels of different dimensions

etched in silicon. These microchannels were etched in silicon using DRIE. Pyrex 7740 glass was bonded to the silicon structure to seal the channels. An illustration of the microchannels is shown in Figure 2.8. For each channel, the fluid was fed from the second square opening in silicon side to the channels and exited to the ambient. Pressure drop was measured between the first square opening and the ambient. Experiments were conducted separately for each channel.

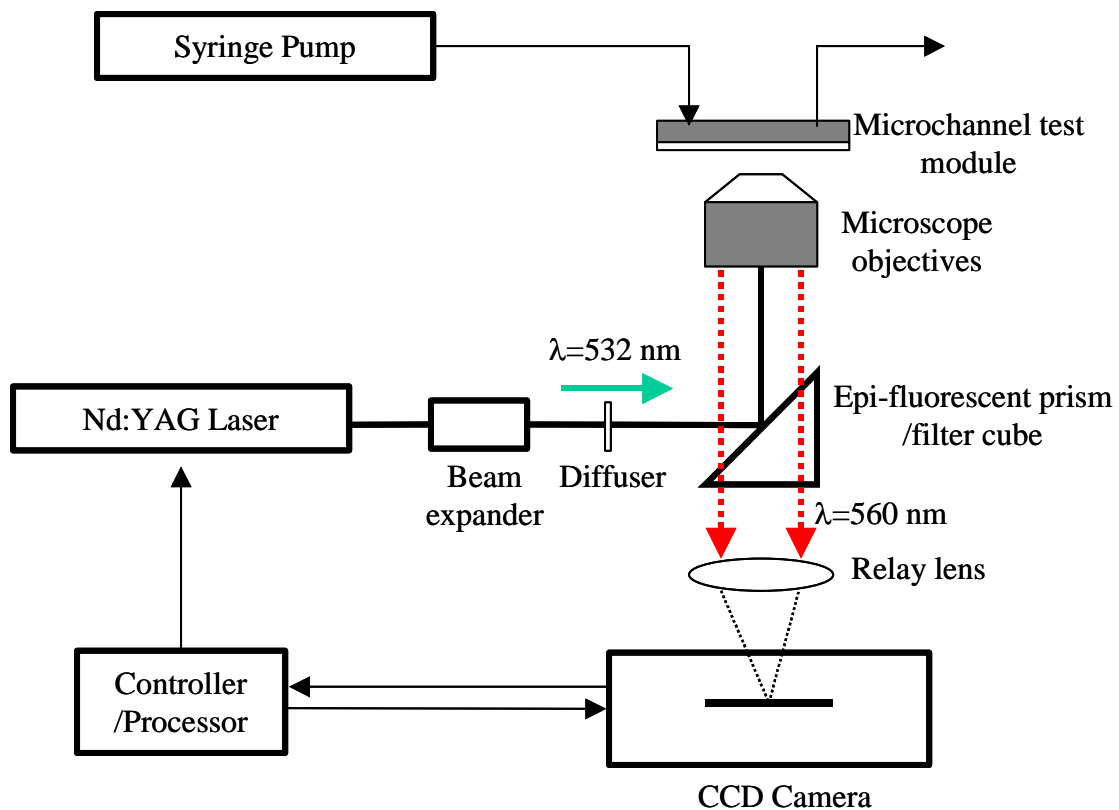


Figure 2.6 Schematic of a Micro-PIV test setup

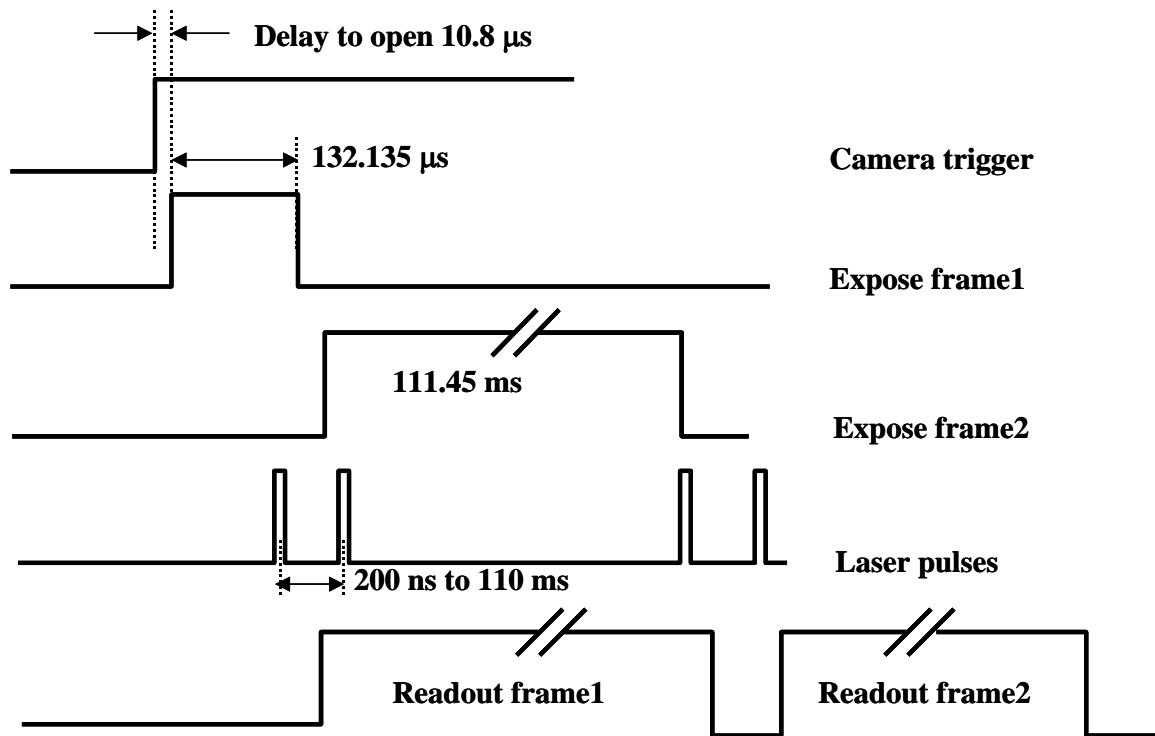


Figure 2.7. Double-frame camera timing and Nd:YAG laser Q-switch pulse firing for cross-correlation PIV data acquisition

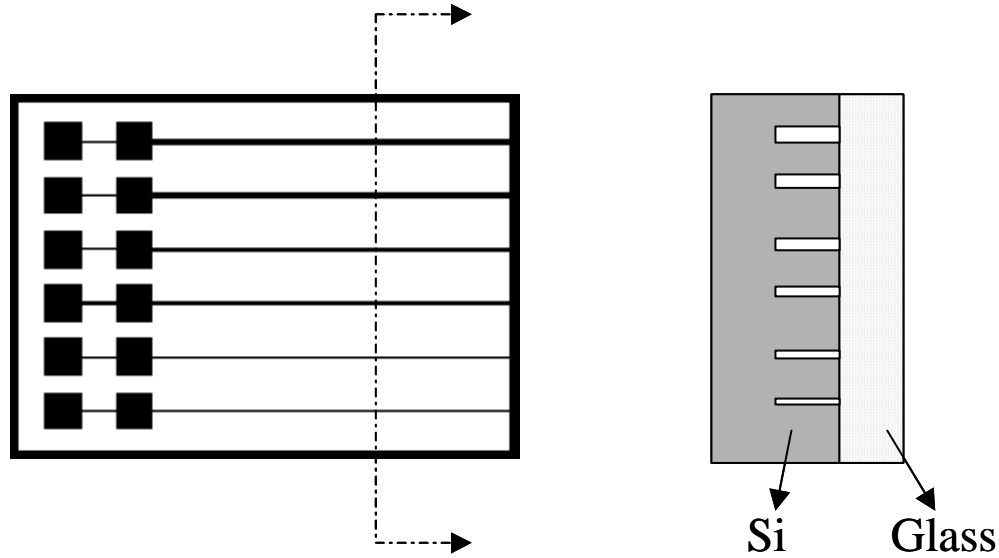


Figure 2.8 Schematic of the microchannel structure for using in micro-PIV measurement

## 2.5 Procedures for Micro-PIV measurement

Flow rate of the syringe pump was calibrated by weighing the mass changes over a period of time. It was found that the actual flow rate supplied by the syringe pump was less than the nominal flow rate. The discrepancy was generally within 3% depending on the flow resistance. At the beginning of each test, the image of channel wall boundary was aligned with the coordinates in the CCD sensor array by rotating the sample holder. A scale factor was determined to be the ratio of the known physical size of the channel width to the image size in the CCD camera array. This scale factor was used to obtain the actual displacement between two laser pulses.

Before taking images for velocity measurement, pressure drop and temperature were closely monitored for about 20 minutes when steady state was achieved. In this experiment, the measurement plane was always parallel to the top surface of the



microchannels. By rotating the fine focus knob for the microscope objectives, measurement plane (x-y) can be translated along z direction, as shown in Figure 2.9. Two-dimensional velocity measurement was thus obtained at different depths of the channel.

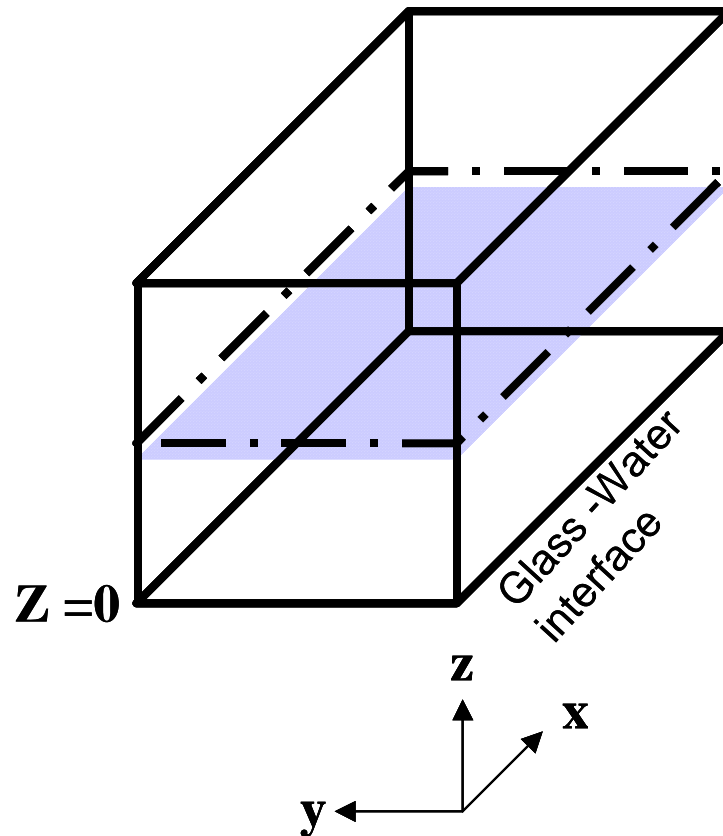


Figure 2.9 Reference coordinates for the velocity measurement

## CHAPTER 3

### FABRICATION OF THE STACKED MICROCHANNEL STRUCTURES

Performance, cost and manufacturability are the important factors to be considered when selecting the materials and fabrication processes for the stacked microchannel structures described in the experiment setup (chapter 2). From thermal performance perspective, materials with high thermal conductivity such as diamond are ideal candidates. However, the high cost and poor manufacturability for diamond substrate made it less attractive. Copper and Aluminum are the common materials used for air-cooled heat sink. Conventional manufacturing techniques such as casting are suitable for these materials. Unfortunately, to make microchannels of less than 100 microns in substrates of these materials is still very hard. On the other hand, silicon has relatively high thermal conductivity (148 W/K-m at 27°C) and low cost due to its large supply. Microfabrication techniques on silicon substrate have been well developed along with the recent advancement of MEMS technology. In the current study, the stacked microchannel structures have been fabricated on silicon wafers using the approaches described below.

A schematic of the stacked microchannel structure is shown in Figure 3.1. A typical prototype consists of five layers of silicon. From the bottom, MC1 and MC2 are the first and second layer populated with parallel microchannels which provide cooling to the chip. MN2 and MN1 are the third and fourth layer for the fluid distribution to the second and first microchannel layer respectively. PT is the fifth layer that seals the structure from the top. Holes for fluid connections were etched in this layer. All the five

layers were bonded into a stack using the procedure described below. A thin layer of platinum was deposited to form the heaters simulating the actual chip and to form temperature sensors for temperature measurement. The prototype chip was wire bonded to a printed circuit board (PCB) to provide electrical connections for heating and sensing. It is noted here that more microchannel layers can readily be added to the stack if desired.

The main steps to fabricate the current prototype are listed in Table 3.1. Details of the techniques in some of the steps are described in the following sections.

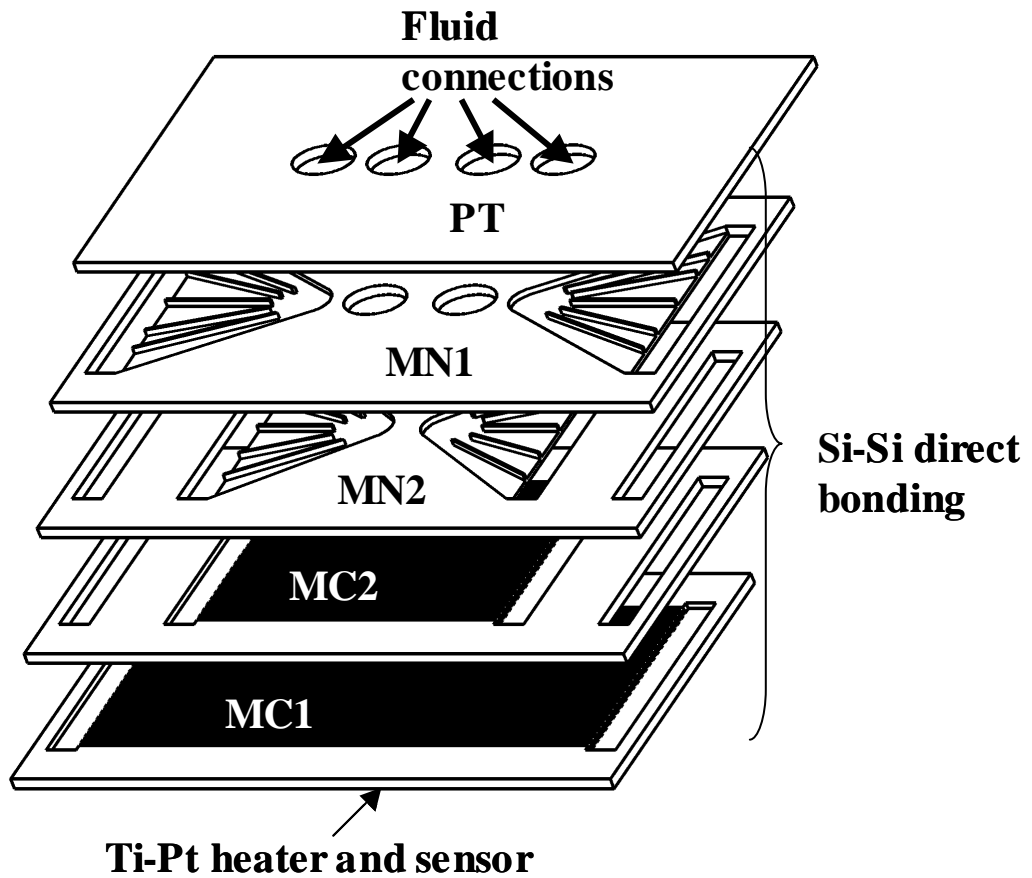


Figure 3.1 Schematic of a stacked microchannel (STMC): All layers have the same overall dimension

Table 3.1 Fabrication steps for STMC

Step	Process
1 Etching of the first microchannel layer with blind headers in silicon wafer (MC1)	Start with cleaning of the double polished bare wafer Form 0.5 $\mu\text{m}$ $\text{SiO}_2$ to protect the back side Photo-resist coating and exposure (AZP 4620) Etch microchannels and headers using Plasma ICP Strip $\text{SiO}_2$ in HF (49%)
2 Etching of the second microchannel layer with through headers in silicon wafer (MC2)	Etch headers on the back side of the wafer using the same procedure used in step 1 Form 0.5 $\mu\text{m}$ $\text{SiO}_2$ layers on the back side with headers Photo-resist coating and exposure on the front side (AZP 4620) Bond the wafer to another carrier wafer as the headers are through Etch microchannels and rectangular headers using Plasma ICP Strip $\text{SiO}_2$ in HF (49%)
3 Etching of manifolds in silicon wafer (MN2 & MN1)	Follow the same procedures as in step 2
4 Etching of the inlet and outlet holes in the fifth layer (PT)	Follow the processes in step 1
5 Bonding of MC1 and MC2	Dicing silicon wafers into rectangular chips Cleaning all chips in Piranha Dip in diluted HF. Surface treatment in RCA-I solution Room temperature bonding Annealing with pressure ( $\sim 32$ psi) at 500 $^{\circ}\text{C}$ in air After this step MC12 forms
6 Adding MN2 to MC12	Using the same procedure described in step 5, bond MN2 to the two layer stack of MC12 to form three layer structure of MC12MN2
7 Adding MN1 to MC12MN2	Using the same procedure described in step 5, bond MN1 to the three layer stack of MC12MN2 to form four layer structure of MC12MN21
8 Adding PT to MC12MN21	Using the same procedure described in step 5, bond PT to the four layer stack of MC12MN21 to form the final five layer structure of MC12MN21PT
9 Final annealing	Anneal the five layer structure in $\text{N}_2$ ambient at 1100 $^{\circ}\text{C}$ for 2 hours
10 Formation of heaters and sensors using lift-off	Form insulating $\text{SiO}_2$ layer on the back of the five layer STMC structure Photo-resist coating and patterning (NR9-8000) DC sputter Ti and Pt Strip off PR with acetone Form oxide to insulate the platinum layer Photo-resist coating and patterning (NR9-8000) Open window in oxide using ICP Descum in $\text{O}_2$ plasma Evaporate 0.5 $\mu\text{m}$ gold Remove PR with acetone
11 Electrical connection	Wire-bonding bond pads in the chip to a PCB
12 Fluid connection	Attach Pyrex capillary tube to the inlet and outlet holes in the top layer using two-part epoxy

### 3.1 Etching of microchannels and manifolds

Etching of parallel microchannels can be achieved with a chemical etching method such as wet etching or dry etching. In this work the Deep Reactive Ion Etching (DRIE) technique was used for both microchannels and manifolds. A standard Bosch process was implemented using an inductively coupled plasma (ICP) etcher in which RF induced plasma accelerates the free ions causing chemical reaction and bombardment of the surfaces to be etched. Compared with a conventional RIE, ICP can achieve better anisotropy as two power supplies are used to generate denser plasma and accelerate the free ions respectively. The Bosch process includes three steps which are repeated throughout the etching cycles. The first step is isotropic etching of the exposed area in the silicon wafer using  $\text{SF}_6$ . A fluorinated polymer is subsequently deposited on both the trench sidewalls and bottom walls using  $\text{C}_4\text{F}_8$ . In the third step  $\text{SF}_6$  is used to etch the polymer anisotropically as it etches the bottom faster than the sidewalls. In the subsequent step, the sidewall is effectively protected by the polymer so that silicon etching only occurs at the bottom of the trench. With appropriate masking layer, Bosch process can be used to etch deep features with aspect ratio up to 20. The selectivity to oxide mask and photo-resist is around 150:1 and 75:1 respectively.

Two key process issues need to be considered particularly. One is the effect of the channel aspect ratio on the sidewall profile. Although a perfectly vertical sidewall profile is usually desired, deviations can occur by about  $1^\circ$ . In general high aspect ratio channels appear to be tapered positively while low aspect ratio channels appear to be negatively tapered (to form re-entrant profile). This is clearly illustrated in Figure 3.2. For a particular aspect ratio it is possible to form perfectly vertical wall through iterations

of fine adjustment of parameters such as RF power, etch time and deposition pressure. The second issue is the decrease of the etch rate as the etching depth increases. As the etching front goes deeper, it is more difficult for the reacting species to arrive at the bottom of the channel and for the etch by-product to leave. This effect is particularly significant for deep and narrow features. Effectively the mean etching rate for the overall process is reduced. This can be seen from Figure 3.3. The data from the manufacture [43] clearly indicates this trend. This effect is not significant for the current study which tested only shallow channels approximately 100  $\mu\text{m}$  deep.

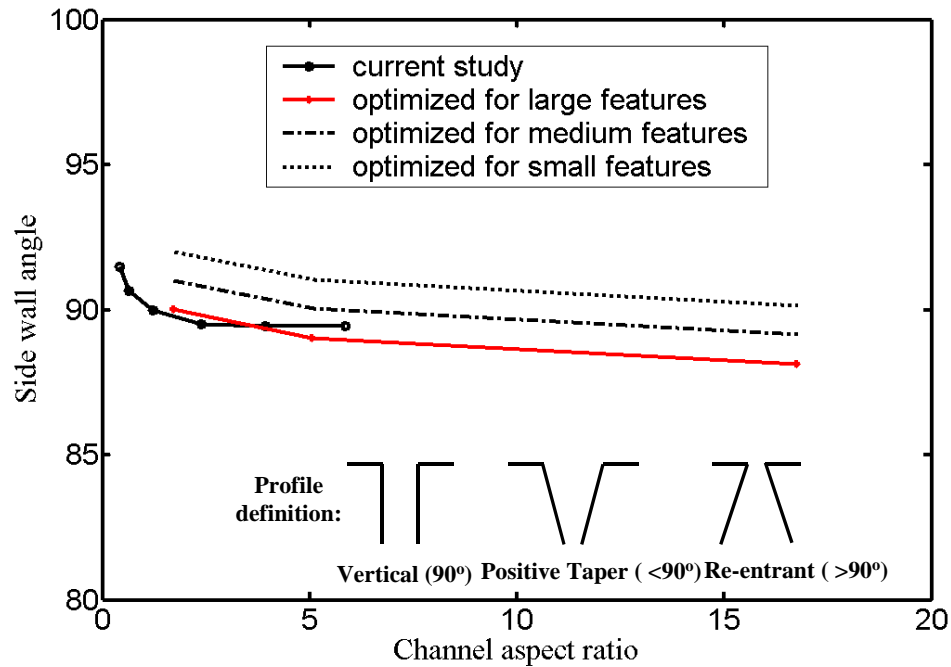


Figure 3.2 Effects of channel aspect ratio on the sidewall profile.

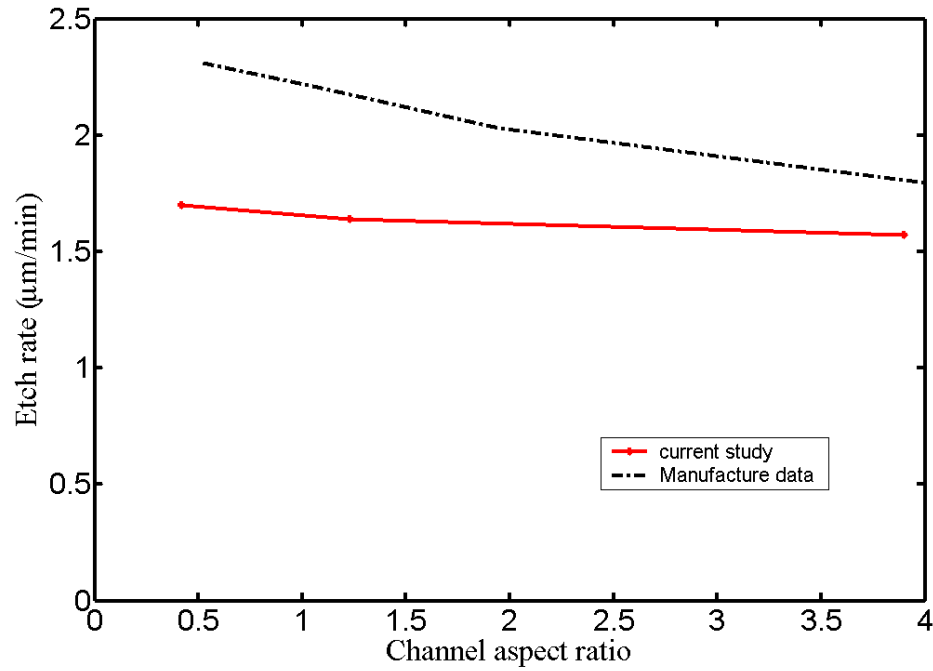


Figure 3.3 Effects of channel aspect ratio on the etching rate

Figure 3.4 shows the fabrication steps for microchannels with through headers. Since headers are through while microchannels are blind, etching has to be done in two steps. Headers are etched initially to a certain depth. Microchannels and headers are etched in the second step until the headers are through. The two etching steps can be performed on the same side of the wafer or on opposite side of the wafer. For the former, a uniform photo-resist coating may be difficult to achieve as the surface has already been patterned with headers. This may cause difficulties as the process window for thick photoresist AZP 4620 is rather narrow. For the latter backside alignment is necessary for the photolithography of the second step. In this work the second method was used where two etching steps were performed on different sides of the wafer. As shown in Figure 3.4 (a), the process started with the deposition of a thick layer of  $\text{SiO}_2$  on the backside of a double-polished silicon wafer. The purpose of the  $\text{SiO}_2$  layer was to protect the backside

of the wafer from scratches and contaminations. In step (b), 14  $\mu\text{m}$  positive photo-resist AZP 4620 was spun on the front side of the wafer and patterned using a standard photolithography process in a Karl-Suss MA6 mask aligner (h-line). The exposed wafer was developed in 1:3 diluted AZ400K developer. Before the Bosch process the photo-resist was fully baked as required by the ICP machine. This caused photoresist reflow and loss of pattern fidelity. After the front-side etching was done in step (c), the photoresist was removed in heated SHIPLEY MICROPOSIT remover 1165A. Silicon dioxide was then removed from the backside. After thorough clean in Piranha solution, silicon dioxide was deposited by PECVD on the front-side of the wafer to protect the surface for future bonding. An AZP 4620 photolithography was performed for the backside of the wafer. Openings were made for both headers and microchannels which allowed ICP etching from the backside as shown in step (d). After the headers were etched through silicon dioxide and photoresist were stripped-off and the wafers were cleaned in Piranha again.

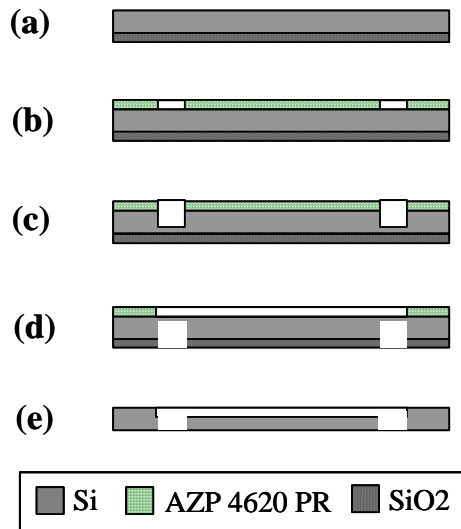
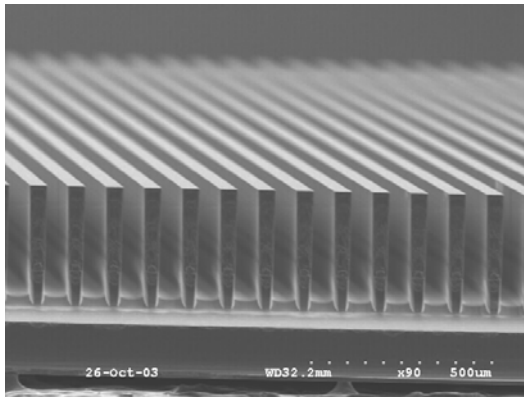


Figure 3.4 Fabrication steps for microchannels with features on both sides

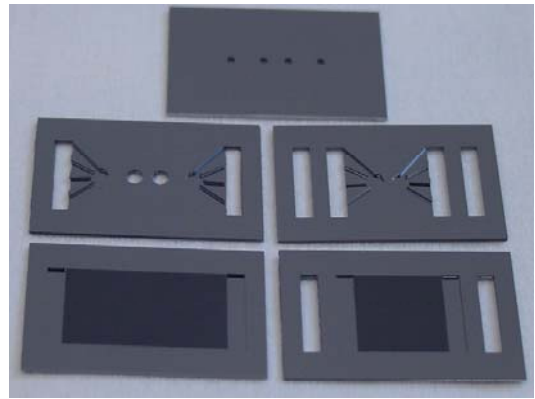


It is noted here that during ICP etching the wafer was cooled from the backside by Helium flow. This is important in order to protect the photo-resist integrity. When there are through features, there will be helium leakage which can cause the machine to shut-down as helium pressure is not able to be maintained. To prevent this, the working wafer was bonded to a carrier wafer using either thin photoresist or thermal conducting grease.

Following similar steps, the manifolds and fluid connection holes are also fabricated on silicon wafers. In the end, five component layers are fabricated in silicon, as shown in Figure 3.5.



**(a) Microchannel array for MC1**



**(b) All five layers fabricated in silicon**

Figure 3.5 Samples fabricated using DRIE etching

DRIE etching usually results in two types of surface roughness on the sidewalls of the microchannel [44]. One is the scallop pattern ( $\sim 0.5 \mu\text{m}$ ) due to the Bosch process. The other is the irregular vertical grooves the dimension of which is process dependent. The causes of the latter are not well understood so far. For the current study, surface

roughness is considered to have little effects as the channel dimensions are much larger. Similar observations have been made in Baviere [24].

### **3.2 Bonding component layers into a stack**

Considering the applications of the current work, two types of bonding methods were explored. They were eutectic bonding and direct bonding. Eutectic bonding uses metals as intermediate layers to form eutectic bond between wafers. Gold and aluminum are known to form eutectic with silicon at 363 °C and 577 °C respectively. A Au-Si eutectic bonding method was performed on testing bare silicon chips. Ti-Au are deposited on bare silicon, and the structure was clamped and heated to 500 °C on the hotplate. The resulted bonding was sufficiently strong such that razor blade testing resulted in breaking silicon. However, for silicon chips with a microchannel pattern the bonding was not strong enough to pass a hydraulic test. This is believed to be due to the significantly reduced bonding area caused when the bonding surface is populated with microchannels. Al-Si eutectic bonding was tested for bare silicon and patterned silicon. Thin foil of Aluminum was sandwiched between silicon ships, and the stack was clamped and annealed at 650 °C for one hour. The bond was strong even for patterned silicon chips. However, it is difficult to control the bond thickness and the introduction of aluminum may contaminate the microchannels through capillary flow.

In the current study, silicon-silicon direct bonding was employed to fabricate the final prototype. The process flow is listed as steps 5 to 7 in Table 3.1.

A typical bonding procedure started with wafer cleaning. The standard cleaning procedure for the CMOS process is the so-called RCA-I and RCA-II cleaning. The two-step cleaning removes organics particles and metals from the wafer surface. However, it

was found that RCA cleaning was not sufficient for the processed wafers in our study. Polymer residuals formed during the DRIE etching were left inside the channels. These polymers are very difficult to remove. Even oxygen plasma cannot completely remove them. With these considerations, Piranha solution was used to perform the cleaning before the bonding. This solution consists of a ratio of 3  $\text{H}_2\text{SO}_4$  and 1  $\text{H}_2\text{O}_2$  by volume. This sulfuric-based solution was found to be very effective in removing the organic contaminations as well as the metallic ones. SEM pictures taken before and after Piranha cleaning show that the polymer residuals left in the Bosch process are significantly less.

After Piranha cleaning and a thorough DI water rinse, the wafer was dipped in dilute 1% high-purity HF for 15 seconds and then rinsed in DI water. The wafer was then treated in a RCA-I solution for about 10 minutes to achieve a hydrophilic surface. Although there are reports that hydrophobic surface can be bonded at room temperature [45], it was found to be rather difficult. After rinsing in DI water and blow-drying with filtered  $\text{N}_2$ , the two wafers were brought together to initiate room temperature bonding. This bonding was achieved by the hydrogen bond between the hydrogen atom and the oxygen atom. Hydrogen bond is a strong dipole-dipole Van Der Waals attraction force. Since the surface is hydrophilic, water molecules are present between the two mating surfaces. These water molecules provide linkages which may help to bridge the gap between the two silicon surfaces [45]. For example, three water molecules could bridge a gap of up to 10 Angstrom [45].

In the present work, a Teflon jig was built to help align the silicon chips. Since all chips have same size and straight edges, the alignment was achieved by flushing all the edges of the chips against three posts in the Teflon jig. After the chips were aligned

properly, a small pressure was applied at the center of the chip to initiate the bonding. A bonding wave was seen through IR imaging to spread from the bond of initial contact towards the perimeter.

The bonded structure was then examined in an Infra-Red Imaging system. An example of the IR image of the interfaces of the two microchannel layers MC1 and MC2 is shown in Figure 3.6. As can be seen the image of the first layer with long channels is superimposed onto that of the second layer. Air gaps are found at the upright corner. This was possibly due to micro-particles caused by the tweezers. This figure also indicates that the alignment between the two layers are good judging from the shadows of the microchannels for the first layer and those of the second layer.

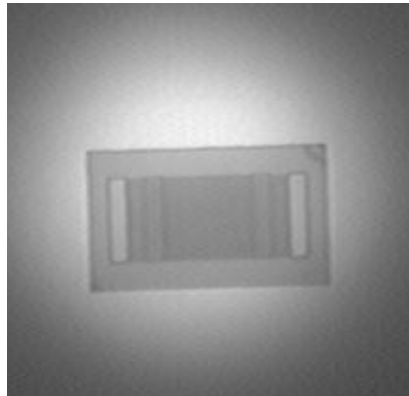


Fig 3.6 IR image of a bonded stack of MC1 and MC2

If the non-bond area is not significant the room temperature bond is considered successful. Otherwise rework is necessary. To rework, the two bonded wafers or chips were immersed in DI water for about 5 to 10 minutes until de-bond to happen.

Room temperature bonding alone is not strong enough for our application. A two-step annealing process was implemented to enhance the bonding strength. At first, the bonded structure was heated at around 500°C in air with a large pressure (~32 Psi) applied by metal block. After about 10 hours the structure was cooled down in air. The pair was then annealed inside a furnace with N<sub>2</sub> flow at about 1100°C for one hour.

The effect of the annealing temperature was investigated. SEM pictures of the bonding interfaces formed at 1100 °C and 300 °C are shown in Figure 3.7. A small gap appears at the interface for 300 °C annealing case while no interface can be identified for 1100 °C annealing at magnitude of 600 x. The latter was also reported in Lasky [46]

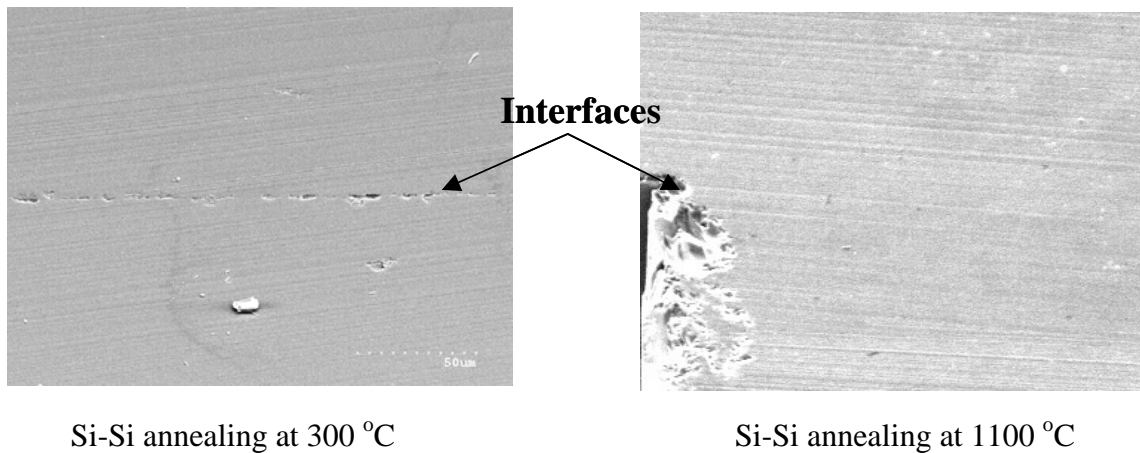


Figure 3.7 Effects of annealing temperature on bonding interface (600x)

The prototype chip has five silicon layers. The two microchannel layers were bonded at room temperature and annealed at 500°C first. Then a third layer of manifold was bonded to the two-layered structure followed by annealing at 500 °C. The rest of the layers were then added to the stack one by one in the same manner. In the end, a five-

layer structure was bonded into a stack. This five-layer structure was finally annealed at 1100°C at the furnace for one hour to close micro-gaps at the interfaces.

Hydraulic test was performed on the stacked structure. No leakage occurred for a pressure of 3 bar which is already beyond the actual test requirement of the experiment. In fact, it is believed that the actual strength of the prototype is much larger than 3 bar as indicated in the literature. [47] and [48].

### **3.3 Metallization**

Figure 3.8 illustrates a simple lift-off process used to form heaters and sensors on the backside of the stacked microchannel structure. The detailed steps are described below.

A 1.2  $\mu\text{m}$  field  $\text{SiO}_2$  was first deposited by PECVD on the backside of the stacked microchannel structure. The surface was then coated with 9  $\mu\text{m}$  negative photo-resist NR9-8000 which subsequently was exposed in the I-line of MA6 mask aligner. After a three-minute post bake at 100 °C in the oven, it was developed in the RD6 developer. A thin layer of Ti/Pt ( $\sim 300/3000 \text{ \AA}$ ) was then deposited on the surface by DC sputter. Upon immersed in acetone, metals on top of photo-resist would be lift-off. One key consideration is that the side wall profile has to be negative in order for the lift-off process to be successful using a DC sputtering machine (isotropic deposition). A Dc sputter instead of E-beam evaporator was used because the process temperature for E-beam was too high for the photoresist. After lift-off of the Ti/Pt, another layer of  $\text{SiO}_2$  was deposited on top of the Ti/Pt layer to provide insulation. Following the NR9-8000 photolithography, contact openings to Ti/Pt were made by etching the  $\text{SiO}_2$  layer using

CF<sub>4</sub> gas in the ICP machine. Ti/Au was then deposited to form the bond pad using E-beam evaporator.

It is noted that before each lift-off process the chip was put in a reactive ion etching machine (RIE) to perform a de-scum process in O<sub>2</sub> for 1 min which can remove photo-resist residuals.

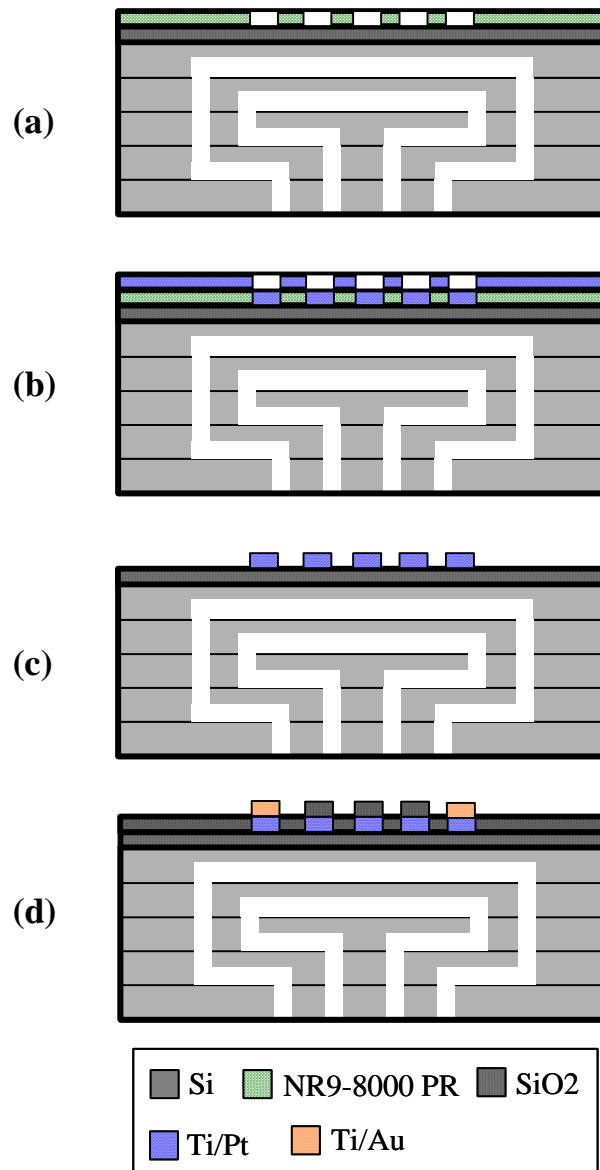


Figure 3.8 Lift-off process steps for heaters and temperature sensors

### 3.4 Packaging

For the experimental test, a PCB type surf-board was used to provide electrical connections. Usually the surf-board comes with copper trace and solder coating. To make wire bonding possible, the solder layer was removed and an extra gold layer was deposited on the copper trace. A cavity was milled at the center of the board to provide spaces for the inlet and outlet tubings to be connected to the test chip. The chip was first attached to the board using epoxy. Electrical connections were established through wire bonding. It is noted that for wire bonding, the wedge bond is rather difficult because the surf board is very compliant. It is important to provide proper clamping to the board and to use low ultrasonic power for a long time.

At this point, the temperature sensors were calibrated inside an oven. The resistances of the sensors were compared with the reference temperature of a thermocouple which was located very close to the surface of the sensors.

The package was finally attached to an acrylic chassis which mechanically supports the package.

Four capillary tubes of 1 mm inner diameter and 1 cm length were glued to the fluid ports of the stacked microchannel structure. High temperature epoxy was used to avoid detachment of the tubing. It is likely that some of the epoxy will penetrate into the ports and may clog the channels. To avoid such problems a more sophisticated fluid ports can be built on the top layer silicon using DRIE etching. Another option was to use a Vinyl sleeve to help seal the gaps between the capillary tube and the silicon wafer surface. After heated to over 180 °C, Vinyl sleeve melts and fills the gap and prevent any penetration of the epoxy applied subsequently.



### 3.5 Fabrication of the test chip for Micro PIV measurement

The microchannel structure shown in Figure 2.8 was etched in silicon using the standard Bosch process. To provide optical access the channels were sealed at the top with glass wafers. In the present work, Pyrex 7740 glass was bonded to silicon using field-assisted anodic bonding. The stack of Glass-Silicon was heated on a hotplate. At 450 °C, 400 V DC voltages were applied. A bonding wave was seen to propagate from the contact point of the probe to the rest of the chip surfaces. Figure 3.9 shows the cross section of the bonded channel.

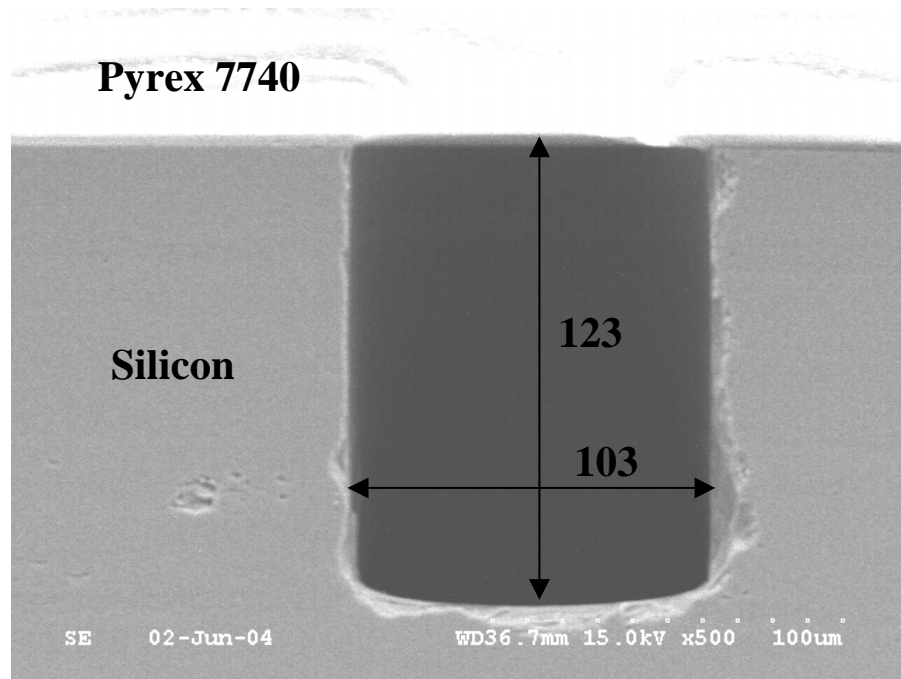


Figure 3.9 SEM picture of the cross section of a bonded microchannel for Micro-PIV. All dimensions are in  $\mu\text{m}$ .

### **3.6 Summary**

Microchannels and manifolds were fabricated in silicon using the standard Bosch process. Aspect ratio effects on the sidewall profile and the etching rate were tested and the results were compared with manufacture's data. The fabricated silicon layers were bonded into a stack using silicon-silicon direct bonding. Integrated thin film heaters and sensors were deposited on the backside the stacked microchannel structure using standard lift-off process. Test structure for Micro PIV measurement was also fabricated.

## **CHAPTER 4**

### **EVALUATION OF THE THERMAL PERFORMANCE OF STACKED MICROCHANNEL HEAT SINKS**

Experiments were conducted to evaluate the thermal performance of the stacked microchannel device fabricated using the approaches described in Chapter 3. Both counter flow and parallel flow configurations were tested for uniform heat flux up to  $70 \text{ W/cm}^2$  over flow rate range of 90 to 350 ml/min. The effects of flow rate ratio between the two microchannel layers were also investigated. Experiments were also carried out to study the thermal performance of the stacked microchannel heat sink under non-uniform heating conditions. Numerical simulations were performed to study the conjugate heat transfer effects for both parallel and counter flow configurations.

#### **4.1 Experimental study**

The test module illustrated in Figure 2.2 includes two layers of microchannels and two layers of manifolds with one layer on the very top to provide the fluid-connecting holes. As the flow passages in each layer are separate, either counter flow or parallel flow can be configured. Thin film platinum heaters and temperature sensors were directly deposited on the backside of the microchannel stack to provide heating and temperature sensing respectively. As mentioned in section 2.1.1, the heaters can be configured to provide either uniform heating or partial heating. A partial heating case can be further categorized as upstream heating or downstream heating depending on the relative location of the heated section of the heaters with reference to the flow direction in MC1.

The temperature sensors were calibrated in an oven with reference to a thermocouple attached to the surface. Figure 4.1 shows the typical calibration curve. Very good linearity is shown for the range tested. These curves were used to determine the wall temperature according to measured the resistance of the sensors. It is believed that the non-uniformity of the oven does not significantly affect the accuracy of the platinum sensors as the chip size is much smaller than the chamber.

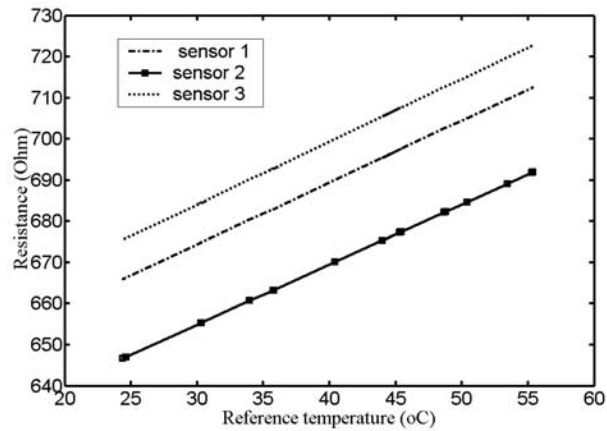


Figure 4.1 Typical calibration curves for the resistive sensors

#### 4.1.1 Uniform heating

The heaters were powered up by a DC power supply to supply heating over 1 cm x 1 cm area. The inlet fluid temperature was kept between 20 and 22 degree Celsius by the recirculating chiller. Through out the experiments flow rate at each layer was controlled independently. For convenience it is necessary to define some terminology. To quantify the overall thermal performance of heat sinks, historically a thermal resistance is defined as the maximum temperature difference divided by the heat flux. In this case, the maximum temperature difference is between the maximum wall

temperature and the coolant inlet temperature. Another term called on-chip thermal resistance is also defined to describe the across-chip temperature uniformity. This resistance is based on the maximum temperature difference over the back side of the chip. Conventionally a bulk resistance is also defined based on the bulk mean temperature rise along channel. Convection resistance is defined based on the temperature difference between the average wall temperature and the local bulk resistance.

To differentiate flow conditions, two series of terms are used here. For parallel flow (PF), it is referred as PF-NM, where “N” represents the relative flow rate of the bottom layer and “M” represents the relative flow rate of top layer. Similarly for counter flow (CF) it is CF-NM. The interlayer flow ratio is one to one if it is not specified.

Figure 4.2 and Figure 4.3 show the wall temperature distribution along the flow direction for parallel flow and counter flow respectively for uniform heating with  $71 \text{ W/cm}^2$ . Both cases have equal flow rate at each layer. For parallel flow shown in Figure 4.2, along the flow direction wall temperature increases almost linearly as a result of the uniform heating. The slope decreases as the flow rate increases. For counter flow in Figure 4.3, the temperature is more uniform and the maximum temperature exists closer to the middle of the chip along the flow direction. Comparing the results shown in Figure 4.2 and Figure 4.3 reveals that the maximum temperature for counter flow is higher than for parallel flow. As a result, the overall thermal resistance is higher for counter flow than for parallel flow. This effect on the overall thermal resistance is less significant as the total flow rate increases. Above certain flow rate there are negligible differences in total resistances between counter flow and parallel flow. This is evidently shown in Figure 4.4. For large flow rate, the overall thermal resistances for both parallel flow and

counter flow are both less than  $0.1\text{ }^{\circ}\text{C}/(\text{W}/\text{cm}^2)$ . For counter flow and small flow rate, the fluid temperature rises rapidly such that near the ends of the microchannel the temperature of the hot fluid in one layer is actually higher than the temperature of the adjacent solid regions where cold fluid in the other layer just starts. In these regions, the heat flux is negative as heat flows from liquid to solid. This effect diminishes as flow rate increases. More on this subject is discussed in section 4.2.

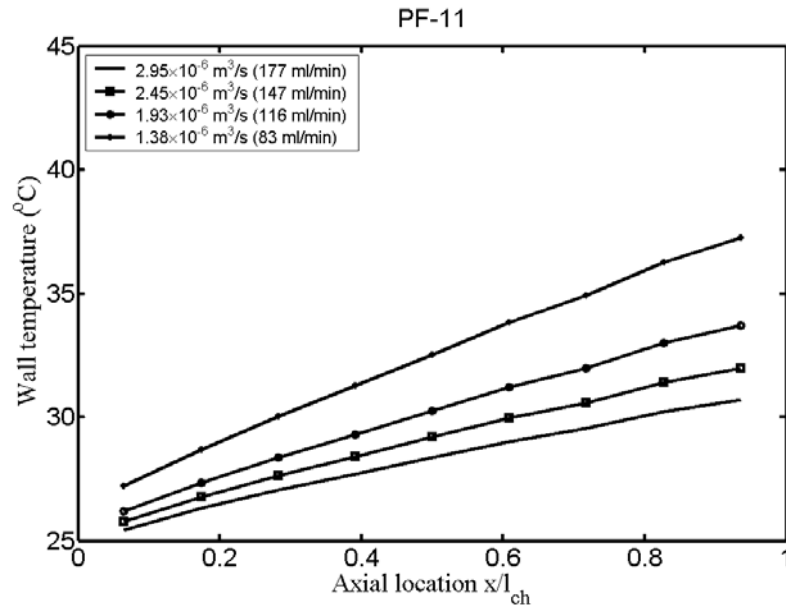


Figure 4.2 Wall temperature distribution for parallel flow and uniform heating

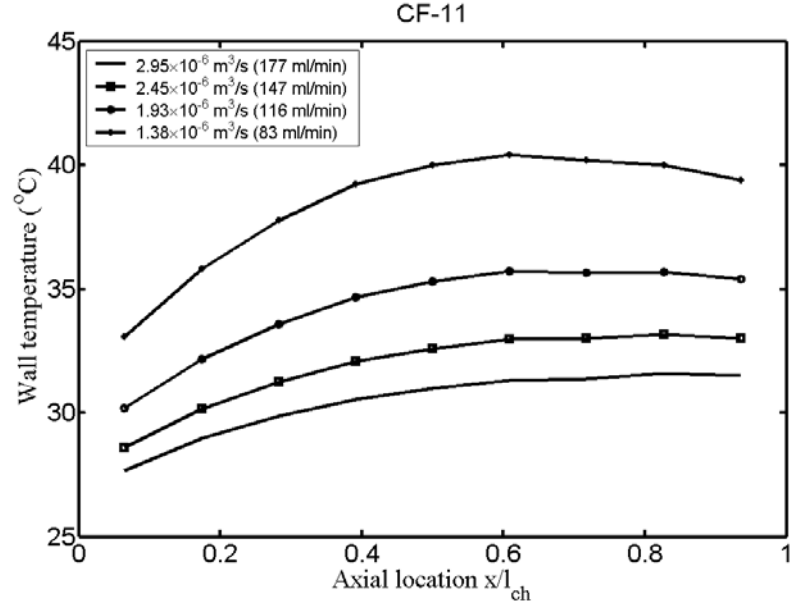


Figure 4.3 Wall temperature distribution for counter flow and uniform heating

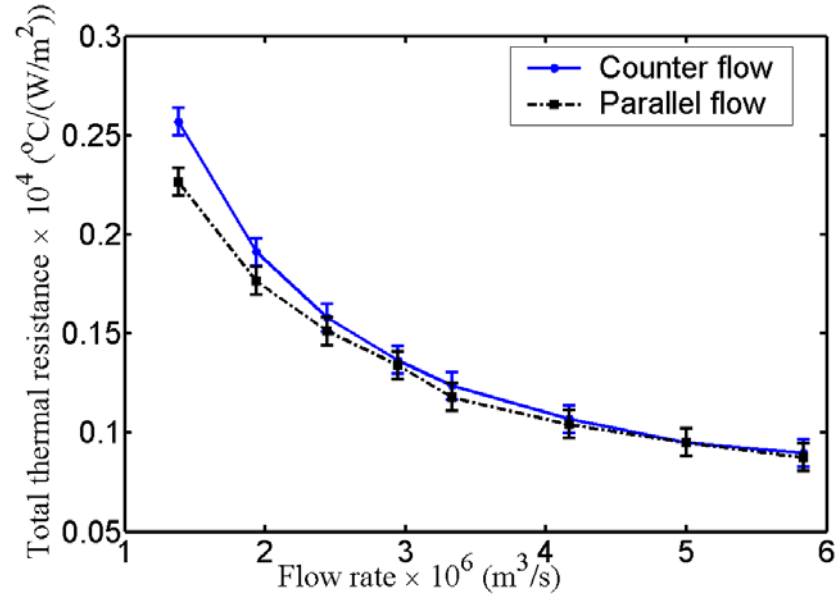


Figure 4.4 Total thermal resistances for parallel flow and Counter flow with equal flow rate at each of the two microchannels layers

Figure 4.5 and Figure 4.6 depict the effects of the different flow combinations on the overall thermal resistance for parallel flow and counter flow. Clearly for both flow

direction configurations, the more flow is passing through the bottom layer the lower the thermal resistance is. However, the pressure drop will drastically increase.

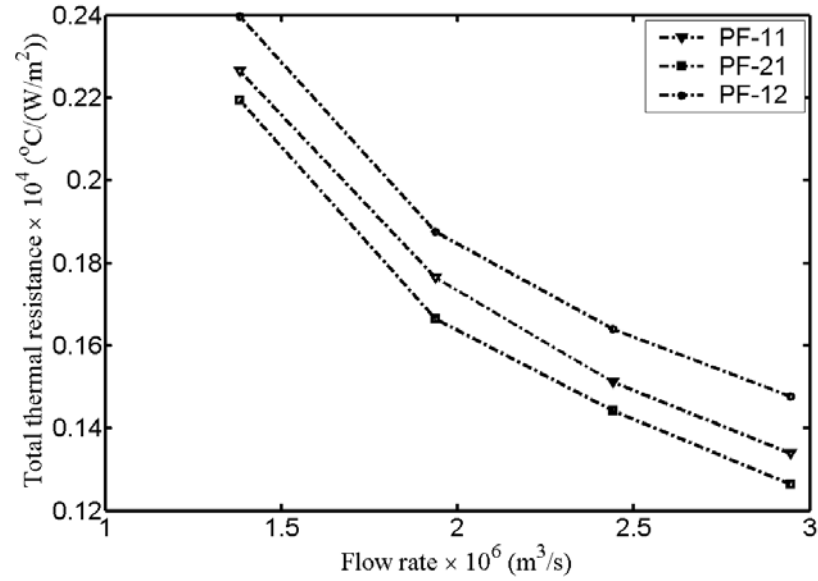


Figure 4.5 Total thermal resistances for parallel flow with different interlayer flow rate ratio

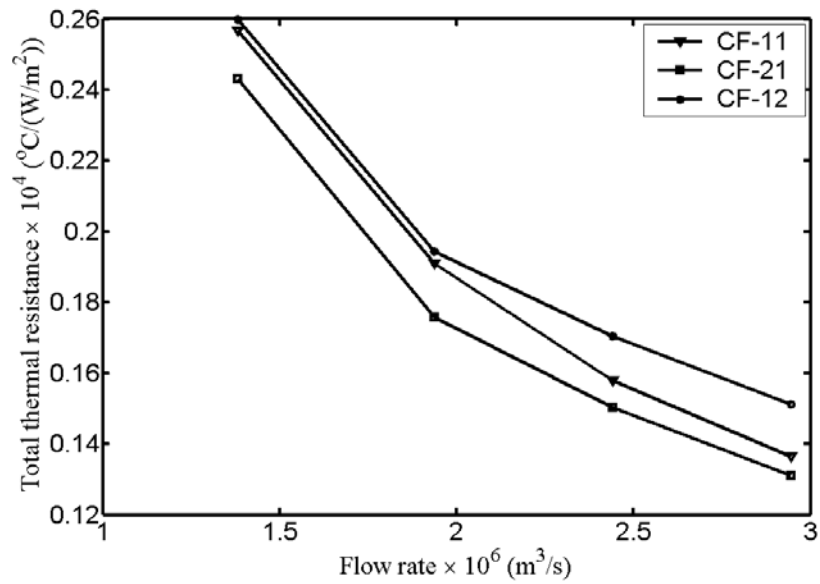




Figure 4.6 Total thermal resistances for counter flow with different interlayer flow rate ratio

The total thermal resistance decreases as the total flow rate increases because both bulk resistance and convection resistance decrease with flow rate increases. It is interesting to note that the total thermal resistance for counter flow decreases faster than for parallel flow. As a result at large flow rate counter flow and parallel flow have almost the same total thermal resistance. For counter flow, increasing flow rate not only reduces the bulk resistance and convection resistances, but also reduces the negative heat flow presented near the ends of the channel.

Flow rate combinations also affect the temperature uniformity across the chip. Figure 4.7 shows the on-chip resistances for three interlayer flow rate ratios for both parallel flow and counter flow. As expected counter flow has significantly smaller temperature non-uniformity than parallel flow. For instance at the lowest flow rate tested, the temperature non-uniformity for counter flow is 40% less than for parallel flow. For counter flow, contrary to the trend of the total resistance, the on-chip resistances increase when more flow passes the bottom layer. For parallel flow the trend in on-chip resistances agrees with the total resistances. The on-chip resistances decrease as more flow passes the bottom layer. Clearly, for counter flow, there is an optimum flow rate combination where both total resistance and on-chip resistance can be minimized. For parallel flow, if pressure drop penalty is not considered, to reduce both the total resistance and on-chip resistance, most of the flow should pass the bottom layer, which is closer to the heat source.

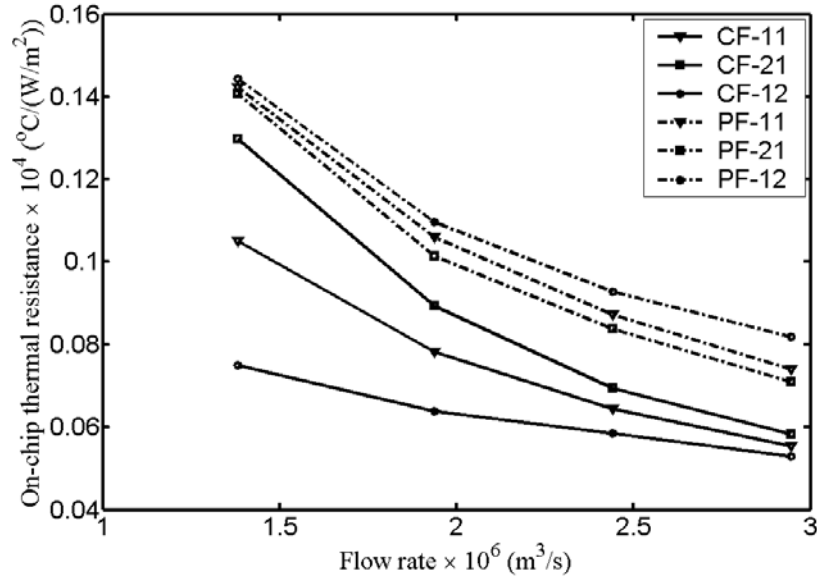


Figure 4.7 On-chip thermal resistances for different flow combinations

Total thermal resistances for different power input level are shown in Table 4.1 and Table 4.2 for counter flow and parallel flow respectively. For both counter flow and parallel flow, the total thermal resistance increases slightly with increasing power input. As power input increase, coolant temperature increases. For DI water the viscosity decreases and the thermal conductivity increases as temperature increases. This would be beneficial to the heat transfer. On the other hand, thermal conductivities of semiconductors such as silicon are usually sensitive to the temperature. Thermal conductivity of silicon decrease considerably as the temperature increases. These two effects compete against each other such that the overall thermal resistance is not sensitive to the power input level.

Table 4.1 Thermal resistances for different power input for counter flow

Flow rate (ml/min)	83	116	147	177
$Q_{\text{input}} = 70 \text{ W}$	0.257	0.191	0.158	0.137
$Q_{\text{input}} = 18 \text{ W}$	0.251	0.181	0.151	0.129

Table 4.2 Thermal resistances for different power input for parallel flow

Flow rate (ml/min)	83	116	147	177
$Q_{\text{input}} = 70 \text{ W}$	0.226	0.176	0.151	0.134
$Q_{\text{input}} = 18 \text{ W}$	0.223	0.174	0.148	0.133

#### 4.1.2 Partial heating

Figure 4.8 to Figure 4.13 present results where only half of the heaters are powered up. For all these cases, equal flow rate is applied at each layer and the total power input is approximately 35 Watts. Figure 4.8 and Figure 4.9 show the measured wall temperature for parallel flow and counter flow respectively. Only the downstream half heaters are powered up. For both cases temperature increases along the reference flow direction. Due to heat spreading, the temperature of the upstream walls also increases. This is more evident for counter flow cases. Clearly parallel flow has a lower peak temperature for the flow rate range studied.

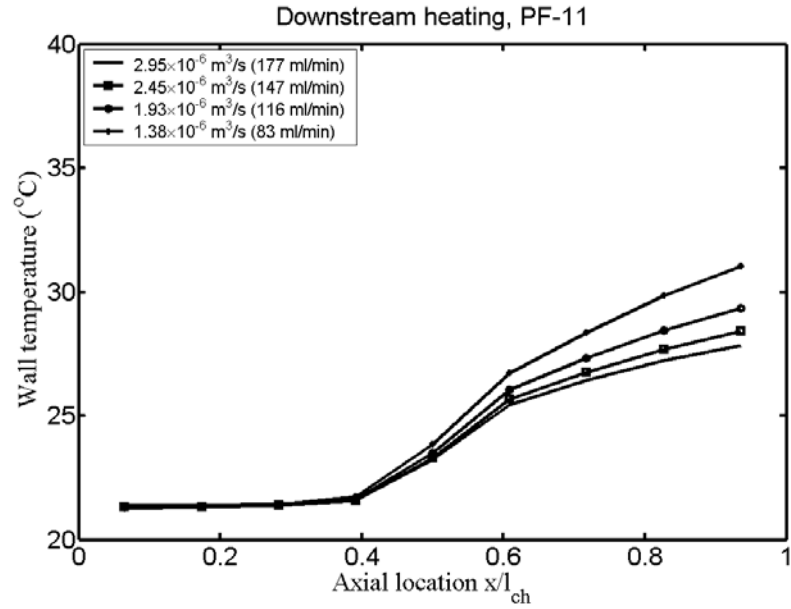


Figure 4.8 Temperature distribution for parallel flow with downstream half heating

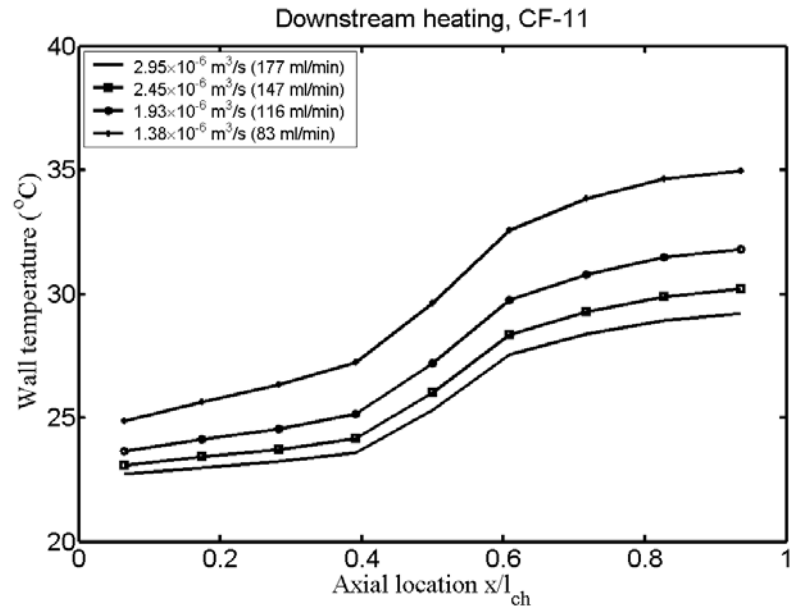


Figure 4.9 Temperature distribution for counter flow with downstream half heating

Upstream heating cases are plotted in Figure 4.10 and Figure 4.11. For parallel flow, upstream heating has better temperature uniformity as well as a smaller peak

temperature than for downstream heating. This is because for upstream heating heat source is localized near the entrance of the channel where the heat transfer is most efficient; whereas, for downstream heating heat source is localized near the exit of the channel where heat transfer coefficient is considerably smaller than entrance region. Similar to the case of downstream heating, the peak temperature for counter flow is higher than for parallel flow.

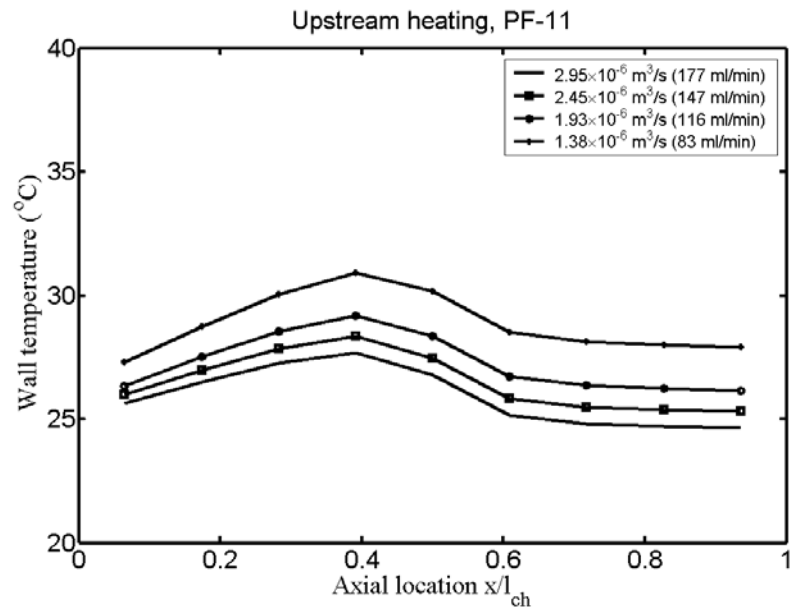


Figure 4.10 Temperature distribution for parallel flow with upstream half heating

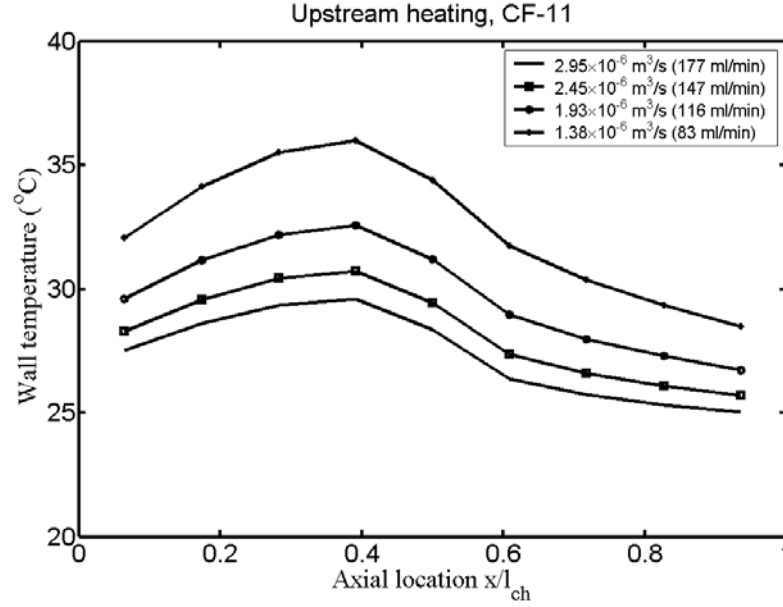


Figure 4.11 Temperature distribution for counter flow with downstream half heating

As expected the total thermal resistance for half heating is higher than uniform heating as the heat is more localized and the effective heat transfer area is less. Figure 4.12 and Figure 4.13 plot the ratio of total resistance for half heating to that of uniform heating for parallel and counter flow respectively. For both cases, the increase in thermal resistance due to half heating intensifies as the flow rate increases. This indicates at high flow rate thermal resistance is more sensitive to the distribution of the heat source. As shown in Figure 4.12, for parallel flow the ratio for upstream heating is lower than the ratio for downstream heating. This is because heat source in upstream heating is closer to region of high heat transfer coefficient. For counter flow, this ratio is lower for downstream heating than for upstream heating as shown in Figure 4.13. This is possibly due to the less severe negative heat flux for downstream heating than for upstream heating. However, for both counter flow and parallel flow, the difference between downstream and upstream heating is rather small.

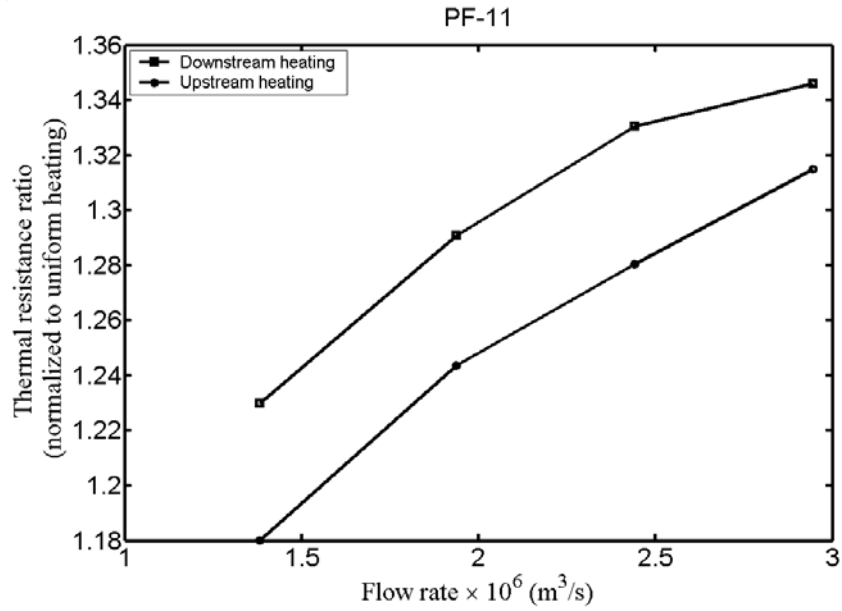


Figure 4.12 Increases in thermal resistance for parallel flow cases undergoing localized heating

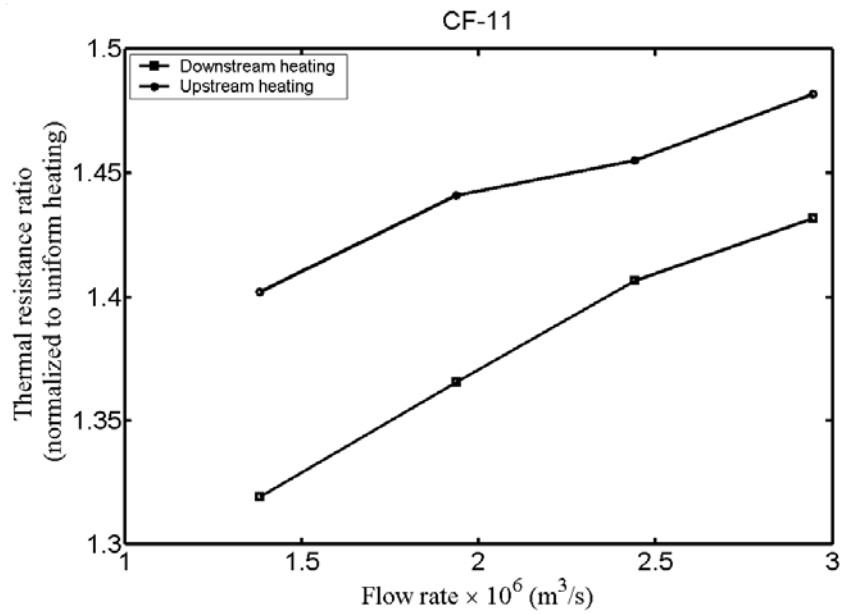


Figure 4.13 Increases in thermal resistance for counter flow cases undergoing localized heating

## 4.2 Numerical study of the conjugate heat transfer for stacked microchannels

Figure 4.4 revealed that for low flow rate conditions, the total thermal resistance for parallel flow is considerably smaller than that of counter flow. However, as the flow rate increases the difference decreases, and for certain large flow rate there is virtually no difference between the total thermal resistances of the two flow configurations. To better understand the thermal performance for parallel and counter flow microchannel heat sinks, numerical simulations were conducted to study the conjugate heat transfer effects.

### 4.2.1 Model construction and validation

The computational domain, shown in Figure 4.14, is essentially a unit cell of microchannel arrays. It includes both solid and fluid regions.

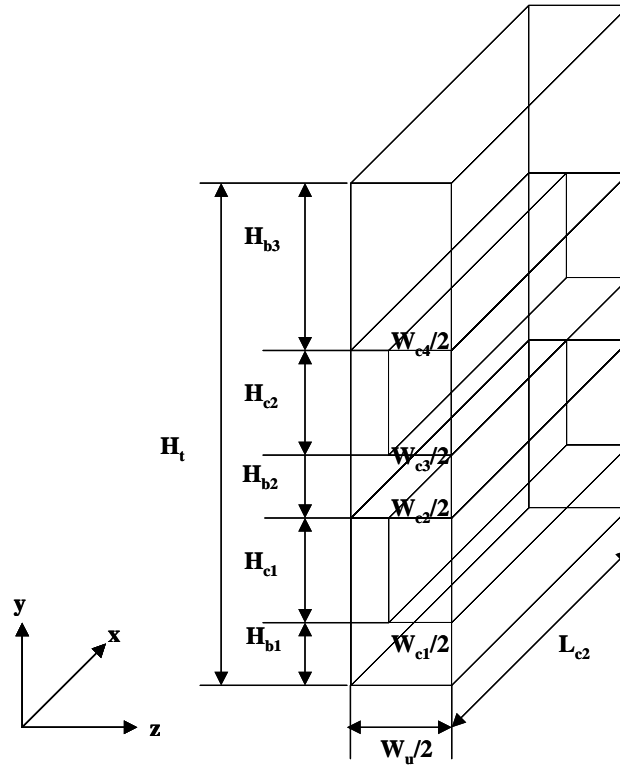


Figure 4.14 Domain of computation for numerical modeling



The dimensions of the computational domain can be determined from Table 2.1. A top cover plate with the same thickness as the microchannel layers is added to the computation domain to simulate the conduction and convection effects of the manifold layers above the microchannels.

Conservation equations for mass, momentum, and energy for laminar flow were solved for the domain using a CFD package FLUENT. The boundary conditions used for the simulation are described below. At the inlets uniform velocity and temperature conditions are assumed. These values are taken from experimental results. Outflow conditions are applied at the outlets. Uniform heat flux is applied at the bottom of the silicon structure, and. symmetric boundary conditions are applied at the vertical centerplanes located at the midpoint of the channel width. All other walls are considered adiabatic. Temperature-dependent thermophysical properties are used for water and silicon.

Tables 4.3 and 4.4 list the input conditions used for the simulation performed in FLUENT. For both counter flow and parallel flow conditions, a small flow rate scenario and a large flow rate scenario conditions were considered.

Table 4.3 Computational conditions for parallel flow

Total flow rate (ml/min)	$T_{f,1}$ (K)	$T_{f,2}$ (K)	$V_1$ (m/s)	$V_2$ (m/s)	Heat flux ( $W/cm^2$ )
83	294.59	294.26	0.4421	0.5127	71
300	294.56	294.61	1.62	1.83	71

Table 4.4 Computational conditions for counter flow

Total flow rate (ml/min)	$T_{f,1}$ (K)	$T_{f,2}$ (K)	$V_1$ (m/s)	$V_2$ (m/s)	Heat flux ( $W/cm^2$ )
83	295.55	295.67	0.4421	0.5127	70
300	294.8	294.85	1.62	1.83	71

Grid sensitivity study was conducted and a grid system of 40x120x120 was used finally for all the computations as further refinement (40x120x200) results less than 0.1% changes in the maximum temperature differences on the bottom wall.

To validate the modeling technique, Figure 4.15 compares the wall temperature calculated from numerical simulations with experimental measurements for the cases of counter flow configuration with the smaller flow rate 83 ml/min. The maximum difference between experimental measurements and simulations results regarding temperature distribution is 1°C. In terms of total thermal resistance, this results in about 5% differences. As can be seen the peak temperature from the experiment is lower while near the edge of the heat source the wall temperature measured in the experiment is higher. The differences are believed to be mainly due to the spreading effects that were not included in the numerical model. As the chip is actually larger than the heat source, thermal spreading would help smooth out the temperature profile. Another possibility is that the uniform inlet velocity and temperature boundary conditions applied in the model may not be accurate. A more detailed model including the spreading effects and boundary conditions that are more realistic should match the experiment better.

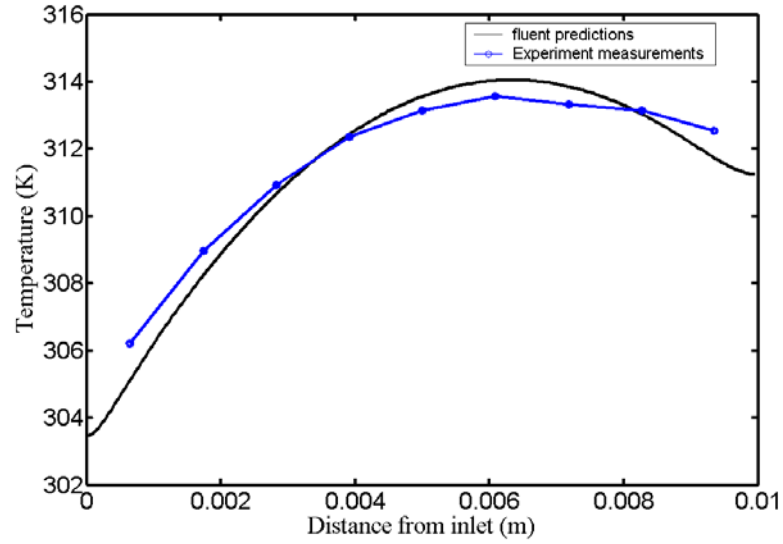


Figure 4.15 Wall temperature distribution along the flow direction for counter flow with 83 ml/min total flow rate

#### 4.2.2 Modeling results and discussion

Figure 4.16 displays the heat fluxes at the six solid-liquid interfaces for the parallel and counter flow conditions. For both cases the flow rate is 83 ml/min. The numbers on the contour lines indicate the heat flux value in  $\text{kW/m}^2$ . For parallel flow in Figure 4.16 (a), the coolant flows along the positive x-direction in both layers. For counter flow in Figure 4.16 (b), the coolant flows along the positive x-direction in the bottom layer and the negative x-direction in the top layer. For parallel flow, the heat flux at the bottom layer peaks at the entrances for each of the three interface walls. As the flow moves along x-axis, the boundary layer thickness increases, and the heat flux decreases rapidly. This is evident from the temperature contour plot shown in Figure 4.17 for different axial locations along the flow directions. The same trend was also reported in Fedorov and Viskanta [4] for a single-layered microchannel. However, the heat flux pattern for the sidewall of the top layer is significantly different. Near the

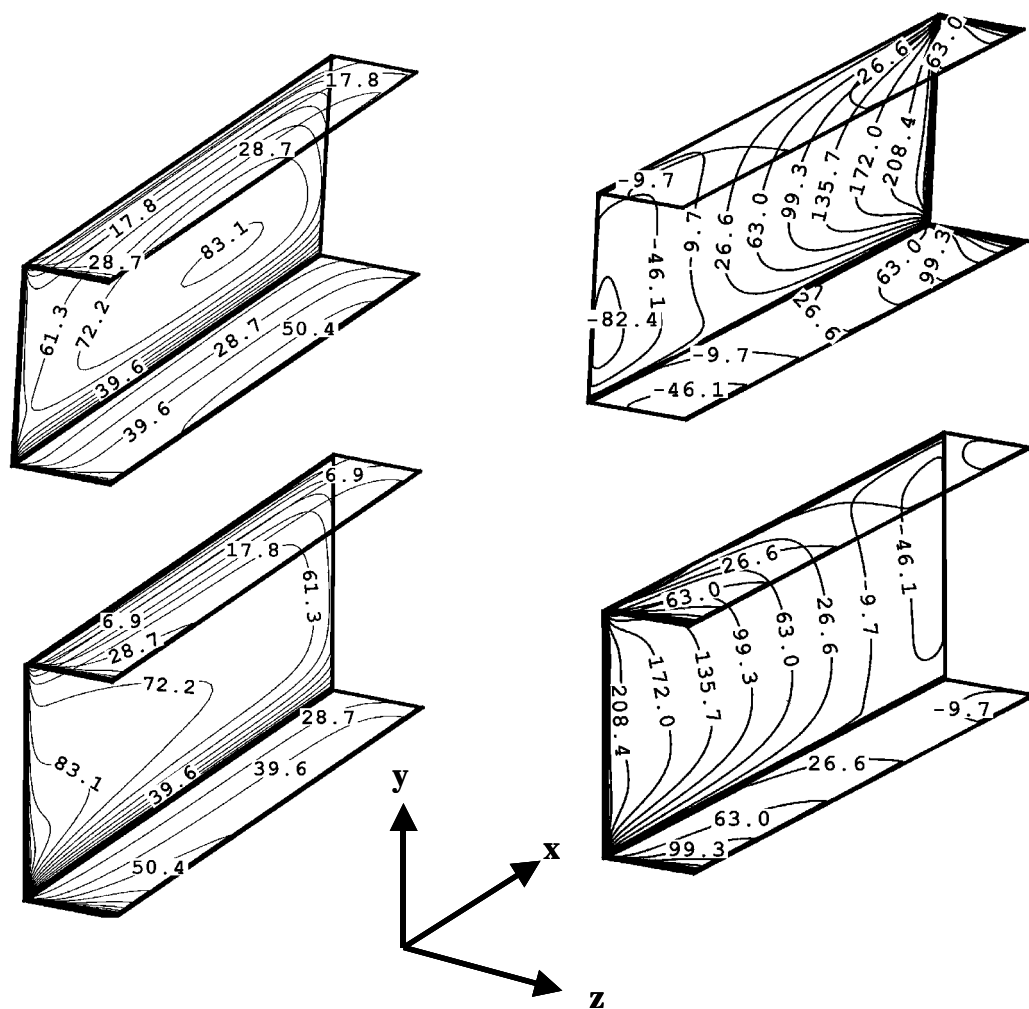
entrance, the heat flux drops initially because of the boundary layer development. After a short distance, it starts increasing. Near the exit (around 7 mm from inlet for the side wall) it approaches a local maximum after which the heat flux drops again. The fact that heat flux increases along the flow direction for the major portion of the channels is rather surprising. This is the unique feature of stacked microchannels. Heat distribution between different layers of channels varies along the flow directions due to the relative importance of the thermal resistance for each layer. Near the inlet the bottom layer dominates the heat transfer such that there are much more heat dissipated from the bottom layer than from the top layer. As the flow progresses through the microchannel, the boundary layer thickness for the bottom layer increases. Although the boundary layer thickness for the top layer also grows, the relative importance of the thermal resistance for the bottom layer increases. Therefore the amount of heat transferred to the top layer increases. As the boundary layer for both layers becomes more developed, the relative importance of the thermal resistance for the top layer increases which causes a reduction in heat flux near the exit. A close look at the heat flux across the interlayer borders supports this argument, although this not shown here. For larger flow rates, this effect is even more pronounced as shown in Figure 4.19 (a). The local maximum heat flux at the sidewall is located further away from the inlet (about 9 mm) as the boundary layer develops over longer distance compared to the scenarios of lower flow rate.

Figure 4.16 (b) depicts the heat flux across interface walls for the counter flow configuration at a flow rate of 83 ml/min. The most striking feature is that near the outlets of the channels of both layers the heat flux is negative such that heat is locally dissipated from the heated water to the surrounding cooler silicon. This is because the

solid region near the outlets is also cooled by fresh water entering the inlets of the other layer. At low flow rates the temperature of the heated fluid is actually higher than the surrounding solid. This is clearly shown in the temperature plot of the bottom layer in Figure 4.18 (c) and top layer in Figure 4.18 (a). An effective heat exchange between the hot fluid and cool fluid exists. This helps to smooth out the temperature gradient as reported in the experimental results in section 4.1. However, the effective heat transfer area is also reduced since not all the channel surfaces are contributing to cooling positively. This has a negative effect on the thermal performance as identified in Figure 4.4.

It is interesting to point out that heat flux variations along the flow direction for counter flow are more dramatic than those for parallel flow. Generally, heat flux near the entrance region for counter flow is larger than that of parallel flow. This is true for both small and large flow rate scenarios.

Comparing temperature plots in Figures 4.17 and 4.18, the maximum temperature for counter flow is located near the center; whereas, for parallel flow it is located at the outlet.



(a) Parallel flow

(b) Counter flow

Figure 4.16 Heat flux at solid-liquid interfaces in  $\text{kW/m}^2$  for a total flow rate of 83 ml/min

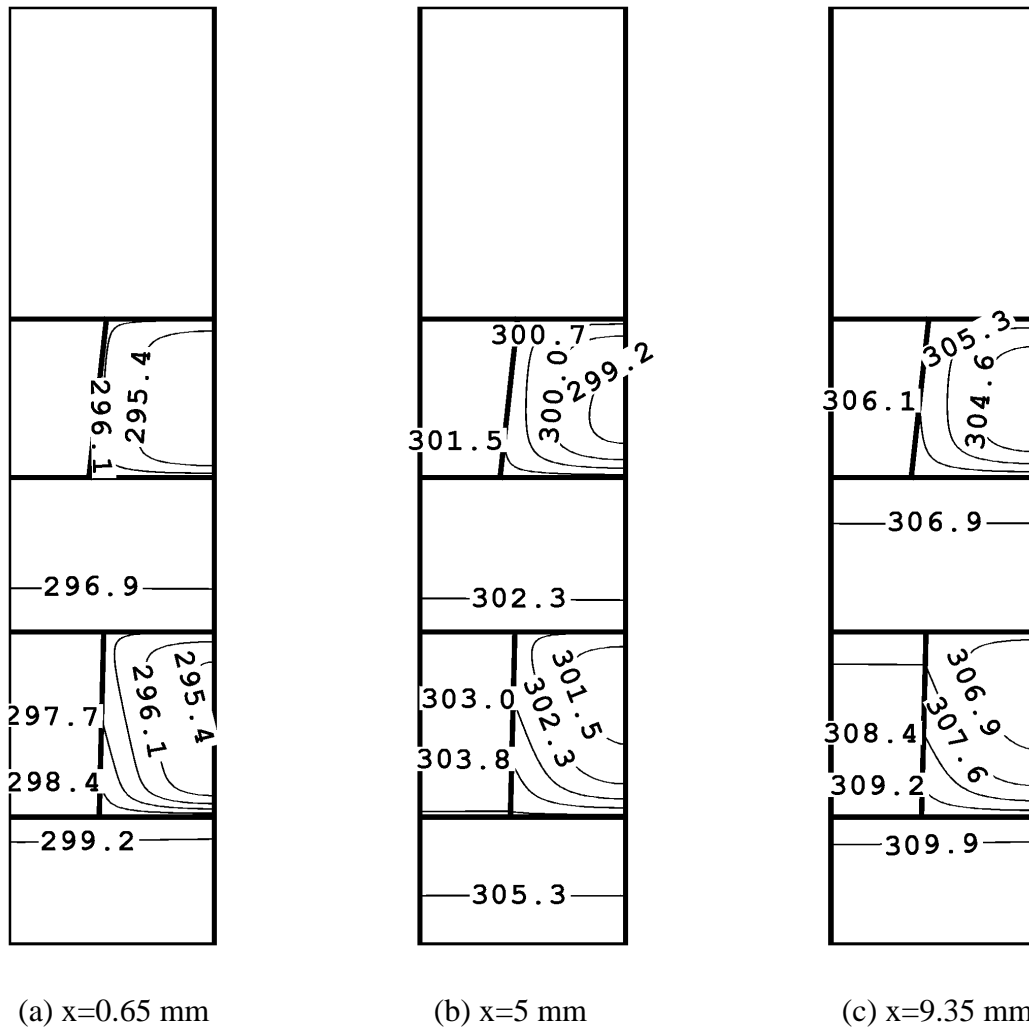


Figure 4.17 Temperature contour map for the cross-sections (Z-Y plane) at different axial position, parallel flow with total flow rate 83 ml/min

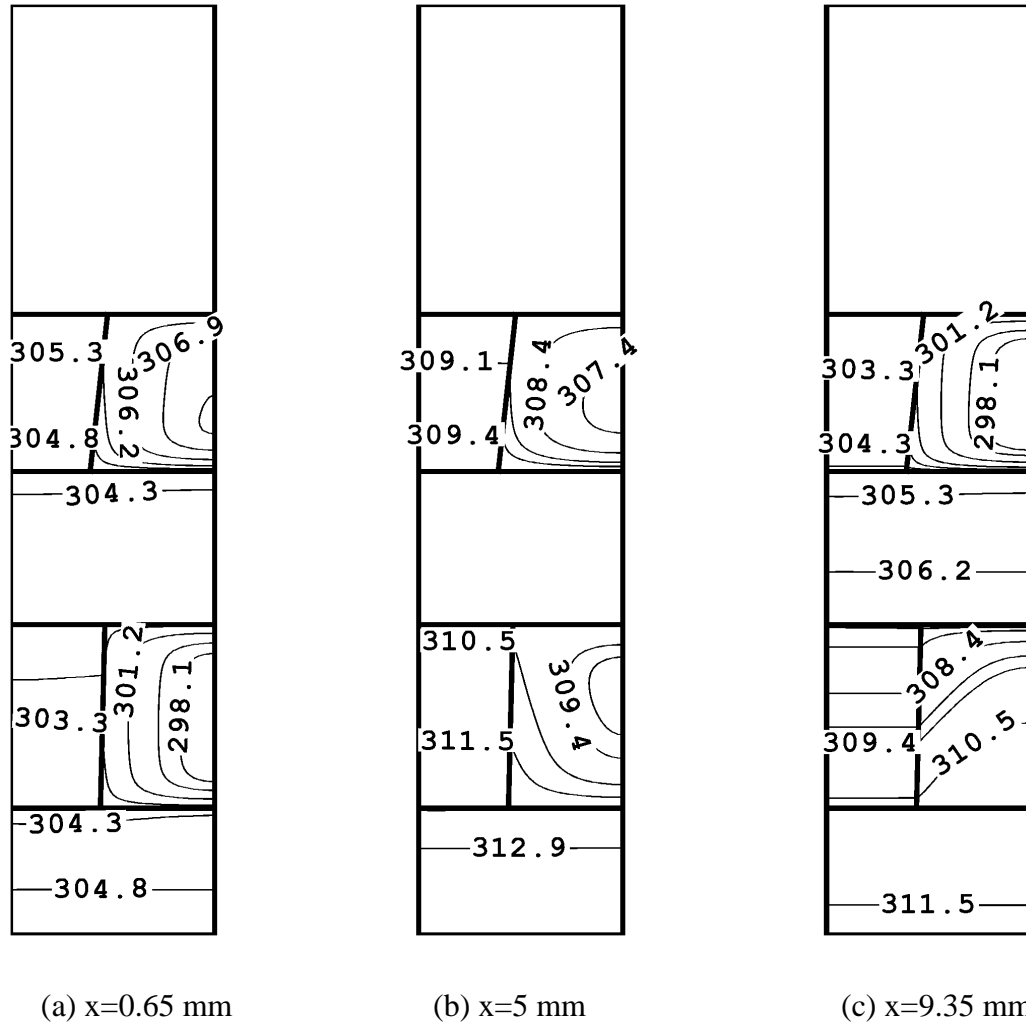


Figure 4.18 Temperature contour map for the cross-sections at different axial positions for counter flow at a total flow rate of 83 ml/min

A similar analysis can be performed for the case of a larger flow rate (300 ml/min) as shown in Figure 4.19. As previously discussed, for parallel flow the effect of the heat flow distribution between the microchannel layers is even larger since the boundary layer develops over longer distance. As a result, heat flux in the top layer increases along the flow direction for a larger portion of the channel. For counter flow the



negative heat flux effect near the outlet is much weaker compared to low flow rate scenario. As can be seen from Figure 4.19 (b), only a small portion of the channel experiences a negative heat flux. This is again consistent with the results reported in Figure 4.4. Figures 4.20 and 4.21 depict the cross-sectional temperature distribution. It is seen that for larger flow rates, the location of the maximum wall temperature is pushed away from the center of the channel length towards the outlet region for the bottom layer.

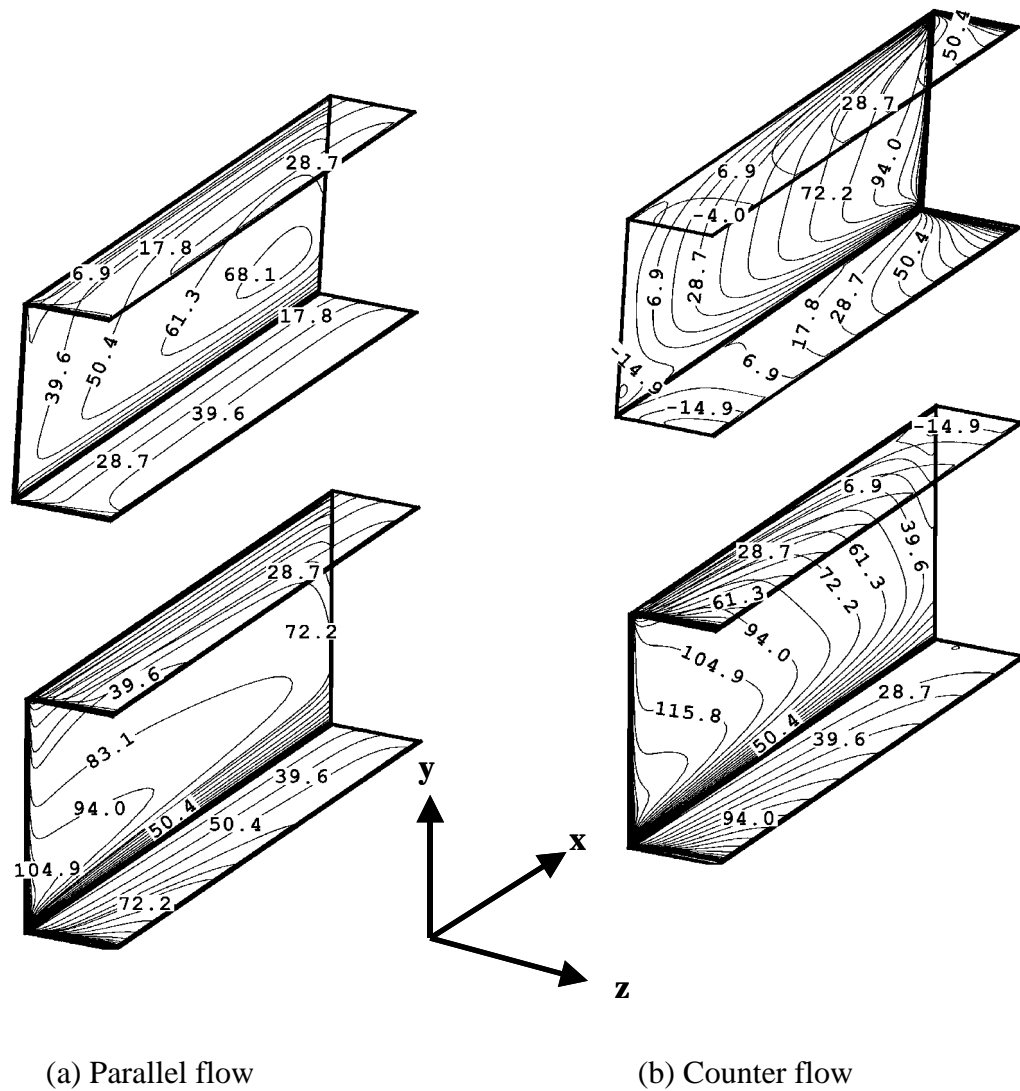


Figure 4.19 Heat flux at solid-liquid interfaces in  $\text{kW/m}^2$  for a total flow rate is 300 ml/min

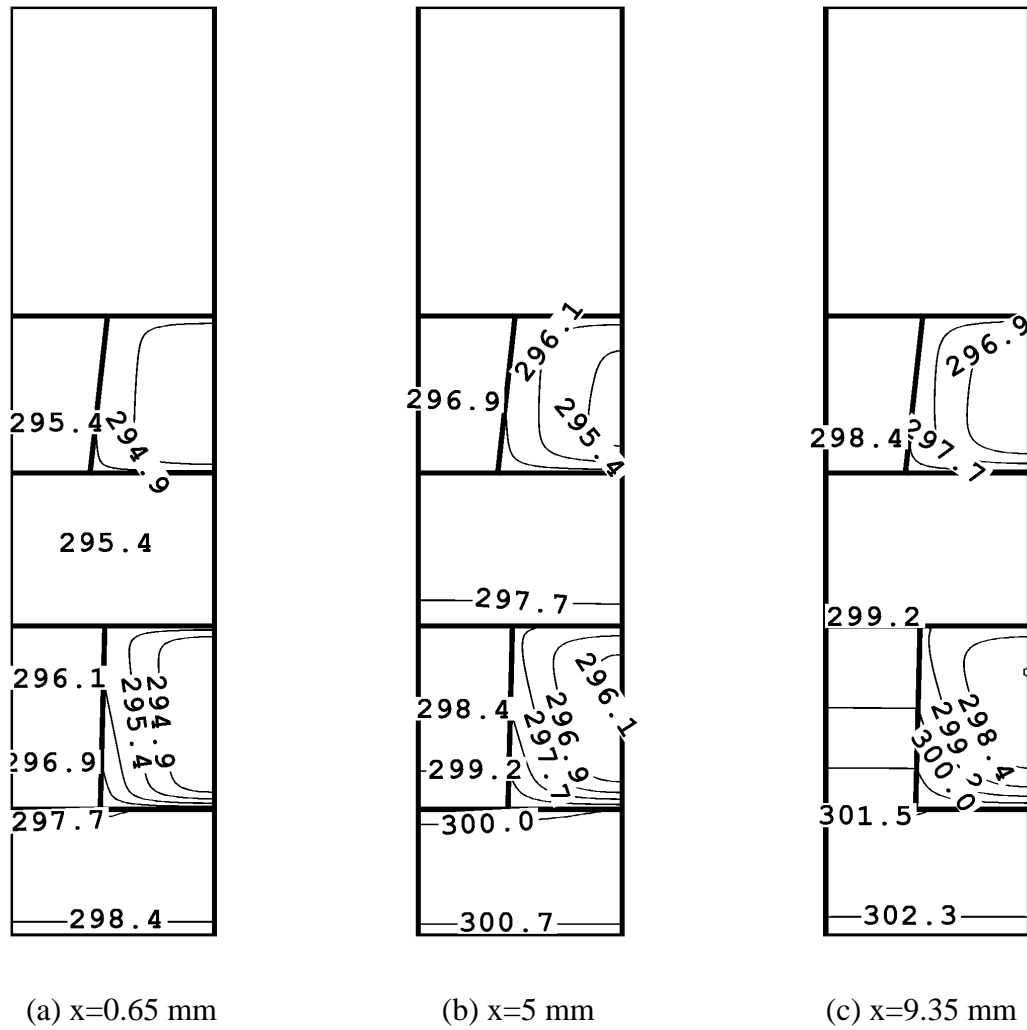


Figure 4.20 Temperature contour map for the cross-sections at different axial positions for parallel flow at a total flow rate of 300 ml/min

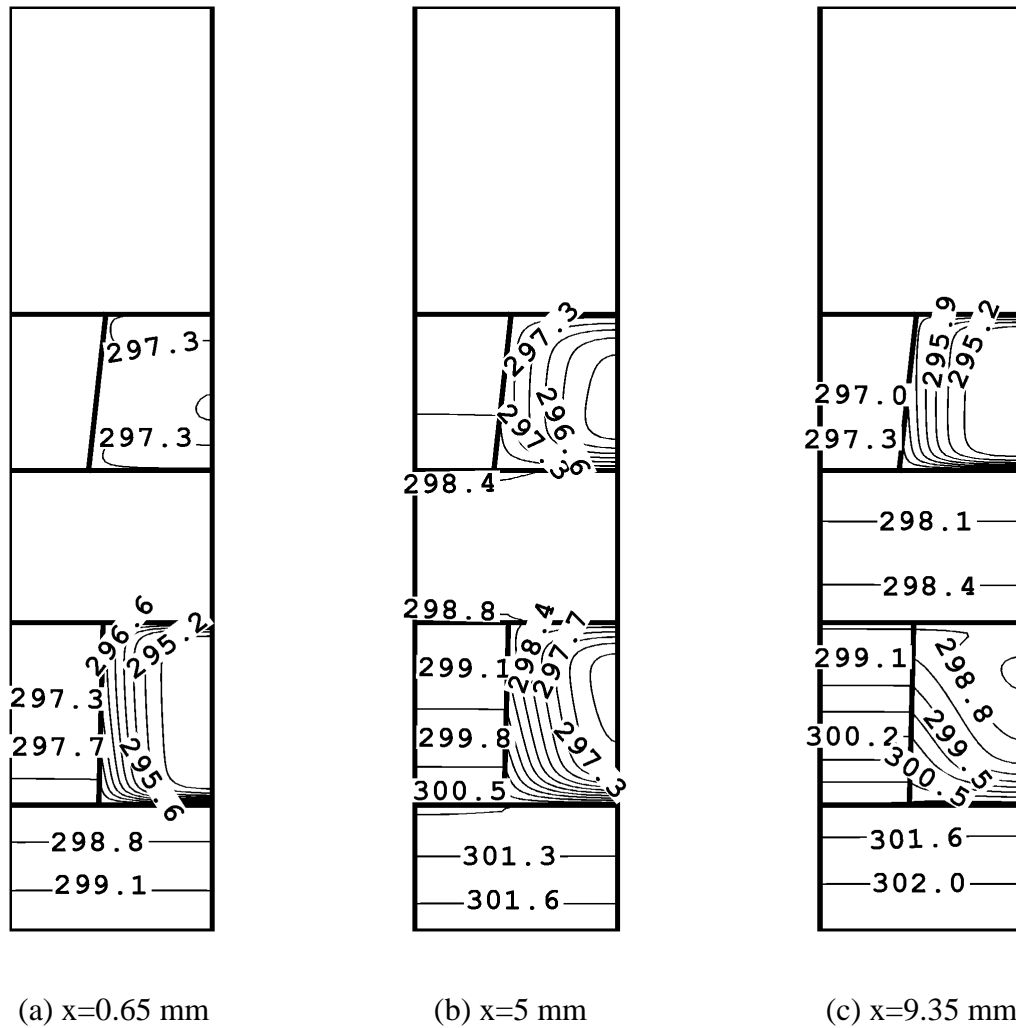


Figure 4.21 Temperature contour map for the cross-sections at different axial positions for counter flow at a total flow rate of 300 ml/min

### 4.3 Summary and conclusions

Experiments and numerical simulations were performed to study the heat transfer process for stacked microchannels. The effects of flow direction and the interlayer flow ratio were investigated. The primary conclusions are listed below.

- a) Thermal resistance as low as  $0.09\text{ }^{\circ}\text{C}/(\text{W}/\text{cm}^2)$  was demonstrated for both counter flow and parallel flow configurations.
- b) It was shown for the small flow rate range that parallel flow configuration has a lower total thermal resistance while the counter flow provides better temperature uniformity.
- c) For both counter flow and parallel flow, total thermal resistance decreases as more fluid is pumped through the bottom microchannel layer. However, the pressure drop significantly increases.
- d) For parallel flow, on-chip resistance decreases as more flow is pumped through the bottom microchannel layer. For counter flow on-chip resistance decreases as more flow was pumped through the top microchannel layer.
- e) Partial heating cases which simulate the non-uniform heat flux of microchips result in a significantly higher total thermal resistance than full heating due to the localization of the heat source. This effect increases with flow rate.
- f) It is revealed through numerical simulation that for the counter flow configuration the heat flux is negative for some regions of the microchannel structure. This effect is less important for larger flow rates.
- g) For parallel flow the heat flux in the top layer increases along the flow direction for the majority of the channel length due to the heat transfer interaction between the top and the bottom layers. This effect is more important for large flow rate.

## **CHAPTER 5**

### **CHARACTERIZATION OF LAMINAR FLOW INSIDE MICROCHANNELS USING MICRO PARTICLE IMAGE VELOCIMETRY**

Existing studies of microchannel flow focused on measuring bulk properties such as pressure drop which are usually lumped with other uncertainties. The scattering of the experimental data indicates that measuring pressure drop alone is insufficient for microscale applications. In this study, a non-intrusive and direct measurement of velocity was performed using Micro Particle Imaging Velocimetry (Micro-PIV). The whole flow field was resolved by scanning through the depth of the channel. The measured velocity profiles for different focal planes were compared with the predicted results from laminar theory. Pressure drop was measured simultaneously. Numerical simulations were conducted to study the effects of the sidewall profile.

#### **5.1 Considerations for Micro-PIV measurement**

The accuracy and spatial resolution of a Micro-PIV measurement are determined by the hardware used and the image and data processing techniques. The effects of seeding particles and optics are described here. An image processing technique is also introduced.

##### **5.1.1 Seeding particles**

In selecting particles sizes, considerations was given to tracking fidelity, visibility, spatial resolution, and Brownian motion effects. A convenient measure of particle tracking fidelity is the relaxation time which basically describes how long it takes

for the particle to attain velocity equilibrium with the fluid. For Stokes flow the relaxation time is proportional to the square of the particle diameter [49]. Small particles should be used in order to track the fluid flow faithfully. For the particles used in the current study the relaxation time is in the order of  $10^{-8}$  s. However, particles should also be large enough to be visible by the imaging optics.

Another issue closely related to the particle size is the Brownian motion effects. Brownian motion results from the random collisions between the fluid molecules and the suspended microparticles. The relative error in measuring velocity caused by the Brownian motion is estimated to be [30]

$$\varepsilon_B = \frac{1}{u} \sqrt{\frac{2D}{\delta t}} \quad (5.1)$$

where  $u$  is the fluid velocity,  $\delta t$  is the time interval and  $D$  is the Brownian motion diffusion coefficient defined as

$$D = \frac{\kappa T}{3\pi\mu d_p} \quad (5.2)$$

In this equation  $\kappa$  is the Boltzman's constant,  $T$  is absolute temperature, and  $\mu$  is the dynamic viscosity. Clearly smaller particles will cause larger uncertainties in the velocity measurement due to Brownian motion. For this study, the relative error due to Brownian motion is typically less than 2%. The error due to Brownian motion is unbiased and can be further reduced by ensemble averaging over repeated measurements. This diffusive error is inversely proportional to the square root of the size of the ensemble.

Particle concentration is another important parameter to be considered in a Micro-PIV experiment. Too many particles will increase the background glow and thus reduce

the signal-to-noise ratio (SNR). On the other hand, insufficient seeding will result in a weak signal. In general at least 2-3 particles are required for each interrogation area. The SNR can be enhanced by the ensemble averaging technique as described in Meinhart et al. [50]. It was shown that ensemble averaging of the correlation function before the peak detection is superior to averaging the image or the vector map to enhancing the SNR.

In this study, the volumetric concentration of the fluorescent particles was maintained in the range of 0.05% to 0.07%. An average correlation was performed over 40 consecutive realizations. The size of the ensemble was found to sufficiently enhance the SNR and reduce the uncertainties caused by Brownian motion.

#### 5.1.2 Spatial resolution and depth of measurement

The spatial resolution of any PIV measurement is defined by the size of the interrogation area and ultimately limited by the effective particle image size. The image of a finite-diameter particle is the convolution of the diffraction limited point response function with the geometric image of the particle [29]. If both the Airy function and the geometry images can be approximated as Gaussian functions, the effective image diameter is

$$d_e = \left( M^2 d_p^2 + d_s^2 \right)^{1/2} \quad (5.3)$$

where  $M$  is the magnification,  $d_p$  is the particle diameter and  $d_s$  is the diameter of the diffraction limited point response function, which is given by

$$d_s = 2.44(1 + M)f^\# \lambda \quad (5.4)$$

where  $\lambda$  is the wavelength of the recording light and  $f^\#$  is the f-number for the objective lens and is generally related to the numerical aperture as

$$f^\#_p = \frac{1}{2NA} \quad (5.5)$$

The above relationship between f-number and numerical aperture breaks down when the paraxial assumption is not satisfied. A more general equation is given as in Meinhart and Wereley [51]

$$f^\#_\infty = \frac{1}{2} \left[ \left( \frac{n}{NA} \right)^2 - 1 \right]^{1/2} \quad (5.6)$$

In the present study a long working distance objective with magnification  $M=60$  and numerical aperture  $NA=0.7$  is used to resolve the  $0.5 \mu\text{m}$  particles. From Equation (5.3), (5.4), and (5.6) the effective image diameter is about  $52 \mu\text{m}$  and  $0.87 \mu\text{m}$  when projected back to the flow field. The particle image is resolved by at least 4 pixels in the CCD array. According to Parasad [52], the uncertainty in identifying the centroid of the cross-correlation peak is approximately one-tenth of the particle image diameter. This indicates an uncertainty of 87 nm in the flow field.

One important parameter in interpreting the velocity data is the depth of measurement since the out-of-focused particles also contribute to the correlation function. Meinhart [35] added up the effects due to the diffraction limit, geometric optics and the finite size of the particle, as shown in Equation (5.7).

$$\delta z_m = \frac{3n^2\lambda}{NA^2} + \frac{2.16d_p}{\tan\theta} + d_p \quad (5.7)$$



Olsen and Adrian [36 ] derived the depth of correlation based on the assumption that the particle image intensity follows Gaussian distribution and the illumination over the interrogation area is uniform. The depth of correlation is given in Equation (5.7).

$$\delta z_{corr} = 2 \left[ \frac{(1 - \sqrt{\varepsilon})}{\sqrt{\varepsilon}} \left( f^{\#2} d_p^2 + \frac{5.95(M+1)^2 \lambda^2 f^{\#4}}{M^2} \right) \right]^{1/2} \quad (5.8)$$

A threshold  $\varepsilon$  is defined as the ratio of the weighting function for the out-of-focus particles to that for the in-focus particles and is typically 0.01.

For the current imaging settings Equation (5.7) gives a measurement depth about 5  $\mu\text{m}$ . The depth of measurement from Equation (5.8) is 4.76  $\mu\text{m}$  if the f-number is determined using Equation (5.5) and 2.65 if Equation (5.6) is used.

Table 1 lists values for effective particle image diameter and depth of measurement calculated using different equations. In this table,  $f_p^{\#}$  is calculated using Equation (5.5) assuming paraxial condition.  $f_{\infty}^{\#}$  is calculated using Equation (5.6). The measurement depth  $\delta z_m$  is calculated using Equation (5.7) and  $\delta z_{corr, p}$  is determined using Equation (5.5) and (5.8) while  $\delta z_{corr, \infty}$  is determined using Equation (5.6) and (5.8).

Table 5.1 The effective particle image sizes and depths of measurement using f-number described in Equation (5.5) and Equation (5.6)

M	NA	n	$d_p$ ( $\mu\text{m}$ )	$f_p^{\#}$	$f_{\infty}^{\#}$	$d_{e,p}$ ( $\mu\text{m}$ )	$d_{e,\infty}$ ( $\mu\text{m}$ )	$\delta z_m$ ( $\mu\text{m}$ )	$\delta z_{corr,p}$ ( $\mu\text{m}$ )	$\delta z_{corr,\infty}$ ( $\mu\text{m}$ )
10	0.25	1	1	2	1.94	31.7	30.8	36.2	38	35.7
20	0.6	1	1	0.83	0.67	31.2	27.7	8.5	7.8	5.5
40	0.6	1	1	0.83	0.67	61.5	54.7	8.5	7.7	5.5
40	0.6	1	0.5	0.83	0.67	50.8	42.4	6.6	6.3	4.2
60	0.7	1	0.5	0.71	0.51	66.7	52.0	5.0	4.8	2.7

### 5.1.3 Refractive index correction for Micro-PIV measurement

In this experiment, the measurement plane was always parallel to the top surface of the microchannels, as shown in Figure 2.9. By rotating the fine focus knob of the microscope objectives, the measurement plane (x-y) can be translated along the z-direction, as shown in Figure 2.9. Two-dimensional velocity measurement was thus obtained at different depths of the channel.

It is noted here that the displacement of the objectives is different from the displacement of the objective planes. In this experiment, an air-immersion lens was used to record the image and the objective plane was located in water which has a different refractive index.

From Figure 5.1 Equations (5.9) and (5.10) can be derived based on the geometry and the Snell's law of refraction. The ratio of the measurement plane displacement to that of objective lens displacement is equal to 1.333, which is the ratio of the refractive index of water to air. A near optical axis condition is assumed in deriving Equations (5.9) and (5.10).

$$L_o = (s_o - L_i) \frac{n_w}{n_a} \quad (5.9)$$

$$\Delta L_o = -\Delta L_i \frac{n_w}{n_a} \quad (5.10)$$

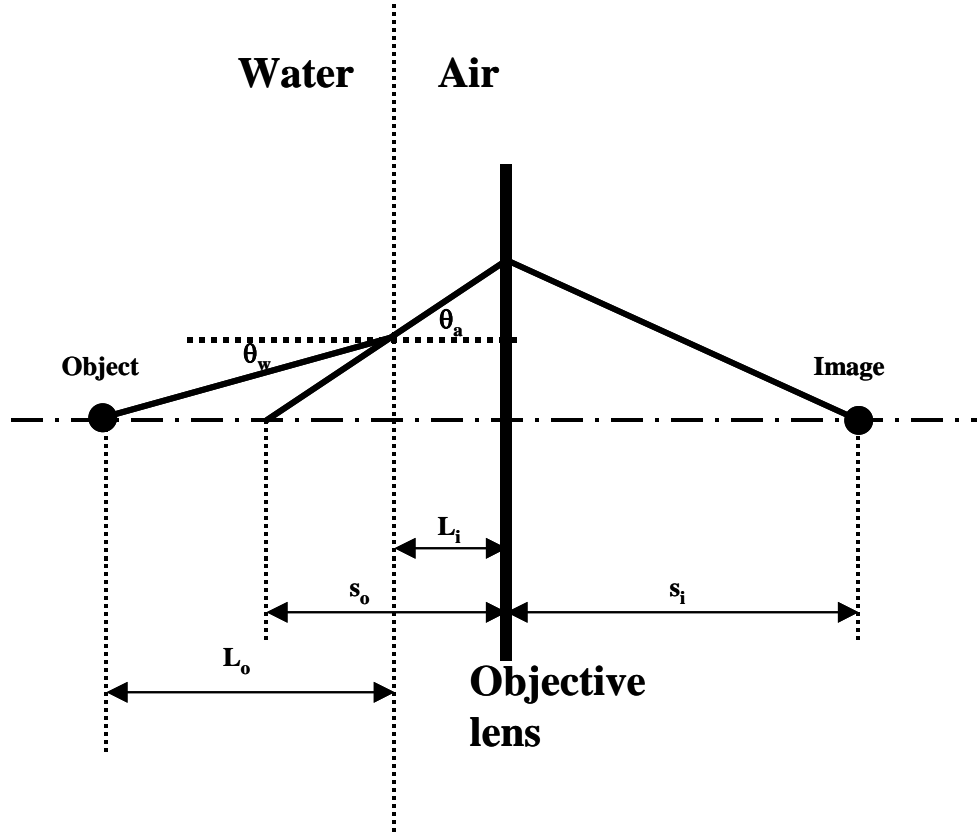


Figure 5.1 Effects of the refractive index on the object plane displacement

One important parameter for PIV measurement is the time interval between the two laser pulses. The displacement between the two interrogation pairs is the product of the time interval and the velocity. An insufficient time interval will make it difficult to detect a slow velocity whereas an excessive time interval will cause severe loss of pairs as a lot of particles will travel out of the second interrogation area during the interval. As a general rule the time interval for cross-correlation is selected so that the particles will travel no larger than one fourth of the interrogation window width. For the current experiments conditions, the time interval was in the range of  $5\ \mu\text{s}$  to  $100\ \mu\text{s}$ .

#### 5.1.4 Image processing and correlation analysis

Following the procedures described in the previous sections, images at different focus planes were recorded for the correlation analysis of each channel. As described in Meinhart et al. [50], for applications requiring low seeding particle density such as Micro-PIV, if the flow is steady state or periodic, ensemble average technique can be used to enhance the signal-to-noise ratio. In this study the average correlation algorithm was performed over 40 consecutive measurements. To determine the velocity vectors, adaptive correlation was first conducted to the image maps. The average velocity map obtained was then used as the offset for the average correlation. This offset was applied to reduce the loss-of-pair issue.

The velocity profile for a channel is shown in Figure 5.2 together with the predicted velocity profiles for trapezoidal and rectangular cross-sections. The effective rectangular channel is  $34\text{ }\mu\text{m}$  wide and  $118\text{ }\mu\text{m}$  deep. As revealed in a close examination by Scanning Electron Microscopy (SEM), the sidewall of the microchannels fabricated using the DRIE process has a positive slope of about  $0.5$  degree. A closer model is a trapezoidal channel that is  $35\text{ }\mu\text{m}$  wide at the top and  $33\text{ }\mu\text{m}$  at the bottom. As indicated in Figure 5.2, the measured velocity matches reasonably well with the predicted values near the center of the channel where y-coordinates are zero. However, in the near-wall region discrepancies are evident. Two factors may contribute to this. One is the noise caused by the reflected light from the wall and the background. The second is the fact that interrogation windows may actually span both fluid and solid walls such that there is a discontinuity in the velocity gradient along the vertical direction. The latter effect is discussed below.

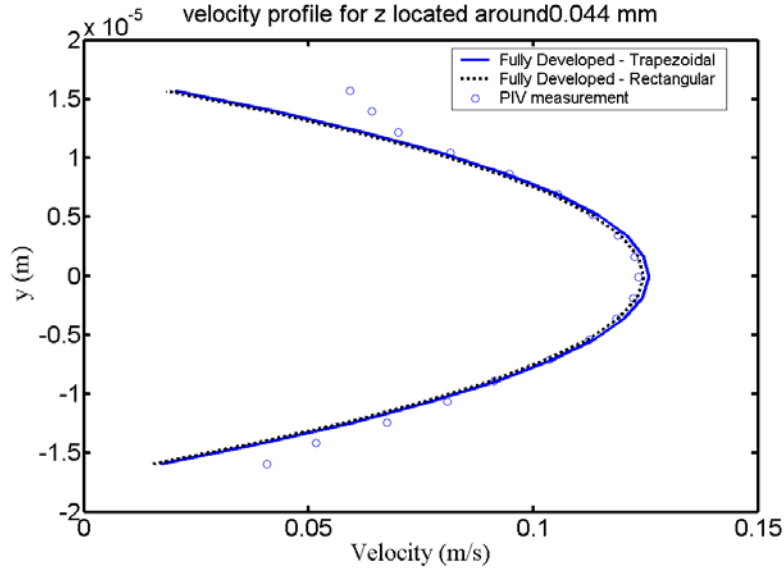


Figure 5.2 Typical velocity profile after correlating two raw image maps

In PIV, the measured velocity is defined by the particle image displacement divided by the product of the magnification and the time intervals. The image displacement is determined by locating the correlation peak where the first derivative of the correlation function is zero. Effectively the velocity is thus given by [36]

$$u_m = \frac{\int u(X,t)W(X)dX}{\int W(X)dX} \quad (5.11)$$

where  $W(X)$  is the weighting function which determines the relative contribution to the correlation function at different positions of the interrogation area. This velocity is essentially an average value over the interrogation area and is assigned to the centroid of the interrogation area. Clearly, the velocity is biased when there is a velocity gradient within the interrogation area.

If the velocity is fully developed, it is only dependent on the y-coordinates as shown in Figure 5.3. The velocity within the interrogation area can be expanded into Taylor series around the centroid of the interrogation area

$$u(y) = u_0 + \left. \frac{\partial u}{\partial y} \right|_{y_0} (y - y_0) + \frac{1}{2} \left. \frac{\partial^2 u}{\partial y^2} \right|_{y_0} (y - y_0)^2 + O(y - y_0)^3 \quad (5.12)$$

where  $u_0$  is the true velocity at the centroid.

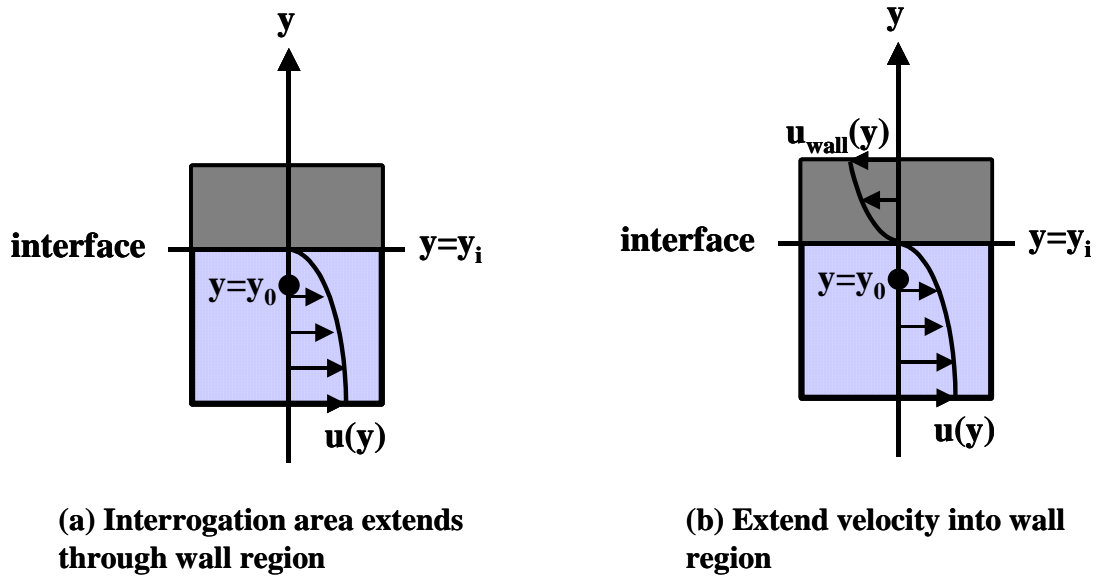


Figure 5.3 Effects of the presence of wall boundary inside interrogation area on the velocity measurement

Clearly, for an interrogation area which covers only the fluid field, the measurement bias is determined by the velocity gradient. If a uniform weighting function is used the measurement bias is the second order as the first-order term is terminated during the integration across the interrogation area.

If the interrogation area extends beyond the wall boundary, the flow field beyond the boundary is not defined, and the velocity is thus biased towards the velocities in the

flow domain within the channel. The largest bias occurs when the centroid of the interrogation area is located on the solid-liquid interface. As the velocity should be zero for the no-slip boundary condition, a non-zero velocity will be measured as only the bottom half of the interrogation area contributes to the correlation function. This issue could be addressed if the velocity field can be extended to the wall area according to Equation (5.11). Unfortunately it is impossible as the velocity and gradient at the centroid are unknown. Instead velocity profile specified in Equation (5.13) is constructed in the wall region as proposed by Tsuei and Savas [52].

$$u_{wall}(y) = 2u(y_i) - u(2y_i - y) \quad (5.13)$$

If Equation (5.12) is applied for the terms in the right hand side of Equation (5.13) and the third or higher order terms are neglected, Equation (5.13) can be written as

$$u_{wall}(y) = u_0 + \left. \frac{\partial u}{\partial y} \right|_{y_0} (y - y_0) + \frac{1}{2} \left. \frac{\partial^2 u}{\partial y^2} \right|_{y_0} [(y - y_0)^2 - 2(y_i - y)^2] \quad (5.14)$$

Comparing Equation (5.14) and (5.12) it is found that such an extension described in (5.13) is accurate to the first order. This is sufficient as both Equations (5.12) and (5.14) produce second order bias in velocity measurement.

Implementation of Equation (5.13) is straightforward. With reference to Figure 5.3, point  $y$  in the wall region and point  $(2y_i - y)$  inside the channel are symmetric about the interface located at  $y_i$ . Since the interface velocity  $u(y_i)$  is zero for the no-slip boundary condition, Equation (5.13) indicates a reflection and a reverse of the velocity field inside the channel about the interface. This is achieved through the image process steps illustrated in Figure 5.4 such that images for both frames are reflected about the interface. The wall region of the second frame is replaced with the reflected image of the

fluid region in the first frame and vice versa. This process is referred to as Image Parity Exchange (IPX) in [53] and will be used hereafter. In micro-PIV measurement, the wall boundary is usually hard to define as it blurs as a result of defocusing. In the present study, a Matlab function which searches for the maximum image intensity gradient is used to locate the channel boundary.

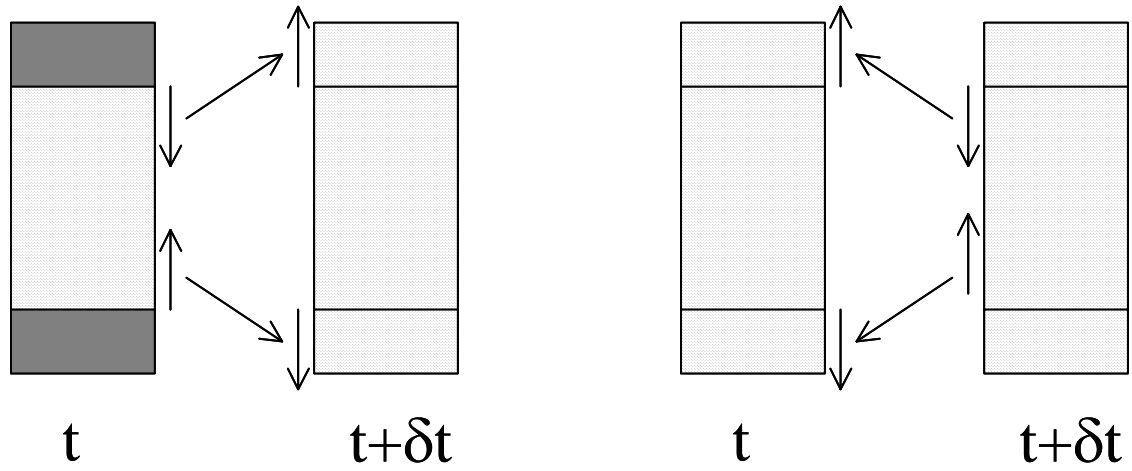


Figure 5.4 Implementation of Equation (5.12) to extend the velocity field to the wall region

It is noted here that before the IPX process mean pixel intensity value is subtracted from the raw image maps to reduce the background noise. To identify the effects of IPX, correlation analysis is also performed on the image maps where only mean intensity is subtracted. These results are compared with predicted velocity profiles from the series solution for rectangular channel [54] and numerical solution for trapezoidal channel. As can be seen from Figure 5.5 applying IPX before the correlation significantly improves the accuracy of the velocity profile prediction near the wall. This is particularly useful for measuring velocity for very narrow channels where boundary effects are significant.



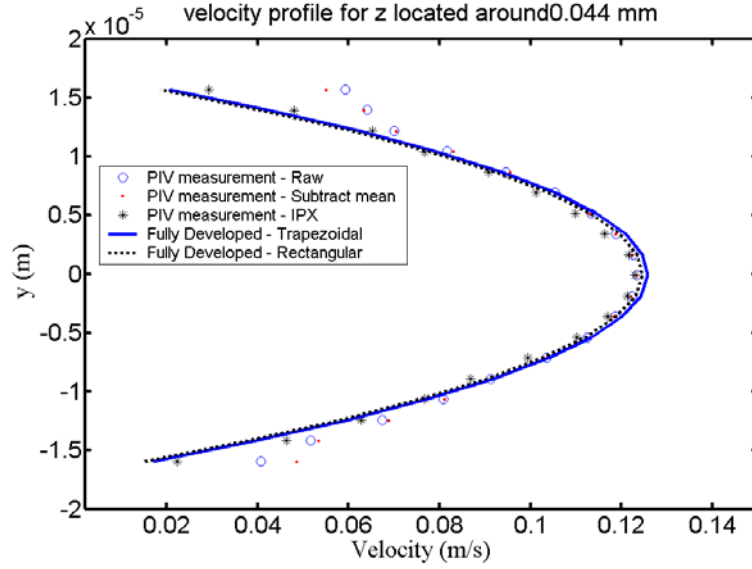


Figure 5.5 Velocity profile using different image processing techniques

## 5.2 Results and discussion

### 5.2.1 Fully developed velocity profile

Experiments were conducted for channels of various dimensions, as shown in Table 5.2 and Figure 5.6. The sidewalls of channel SG34 and SG53 are slightly tapered such that the opening near the silicon-glass interface ( $z=0$ ) is wider than at the bottom of the channel ( $W_{c1\_SG} > W_{c2\_SG}$ ). The measurement results of the velocity profile are compared with those predicted from laminar theory for the actual trapezoidal channel and the effective rectangular channel with the same area. To the best of the author's knowledge, the minimum channel width studied using Micro-PIV in the literature is 50  $\mu\text{m}$ . The current study appears to be the first to measure sub-50  $\mu\text{m}$  channels.

Table 5.2 Dimensions of the channels for Micro-PIV measurement

Channel	SG34	SG53	SG103
$W_{c1\_SG}$	35	54	103
$W_{c2\_SG}$	33	52	103
$H_{c\_SG}$	118	119	123

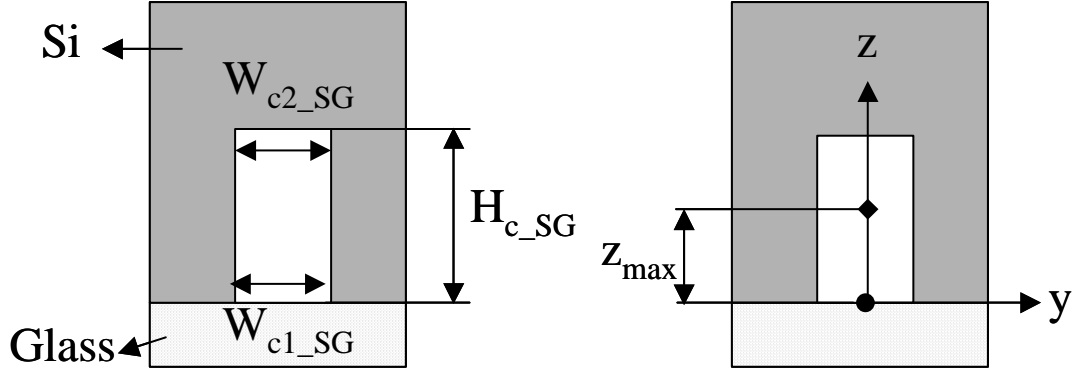


Figure 5.6 Cross-section of a microchannel for Micro-PIV test

Figure 5.7 and 5.8 plot the velocity profile at different  $Z$  planes of channel SG34 for flow rates of 1 ml/hour and 4 ml/hour respectively. For a flow rate of 1 ml/hour, the mean velocity is 70 mm/s, and the measured velocity profile matches very well with results predicted from laminar theory for all the planes measured. The trapezoidal model results agree better with experimental measurements than the rectangular model, particularly away from the geometric symmetry plane.

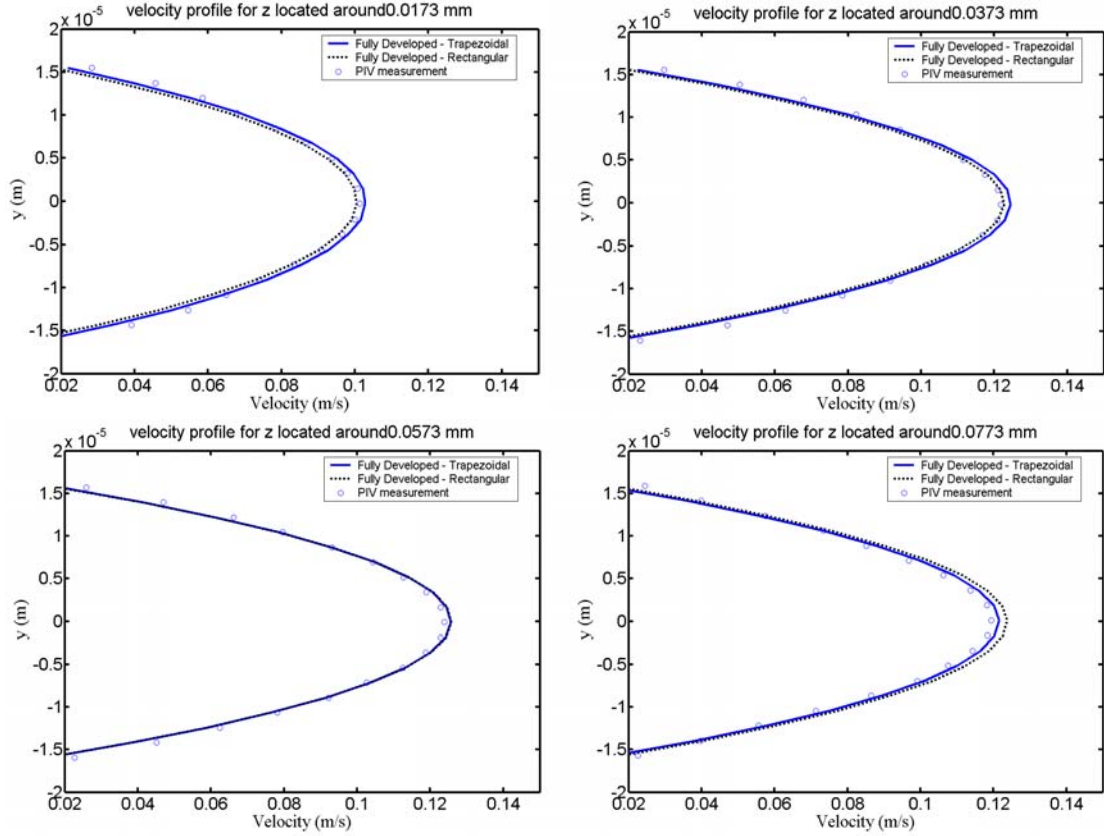


Figure 5.7 Velocity profile for SG34 channel (1 ml/hour or 0.07 m/s)

For the 4 ml/hour flow rate case, as shown in Figure 5.8, a small discrepancy is noticed between the measured velocity and the predicted values at the center of the channel. The measured velocity seems to be negatively biased by 3%.

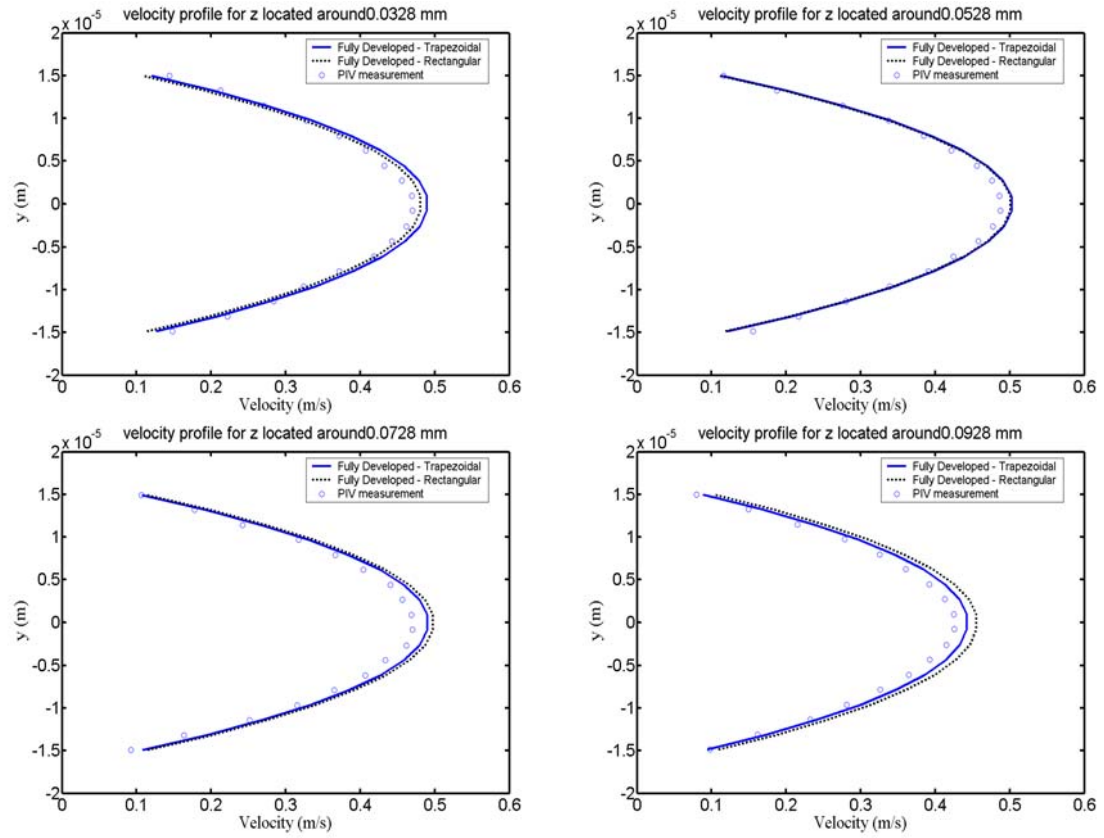


Figure 5.8 Velocity profile for SG34 (4 ml/hour or 0.28 m/s)

Figure 5.9 shows the velocity profile for SG53. In general the measured velocity agrees with predicted results from laminar theory. Again near the center of the channel the Micro-PIV results are about 4% less than the predicted results.

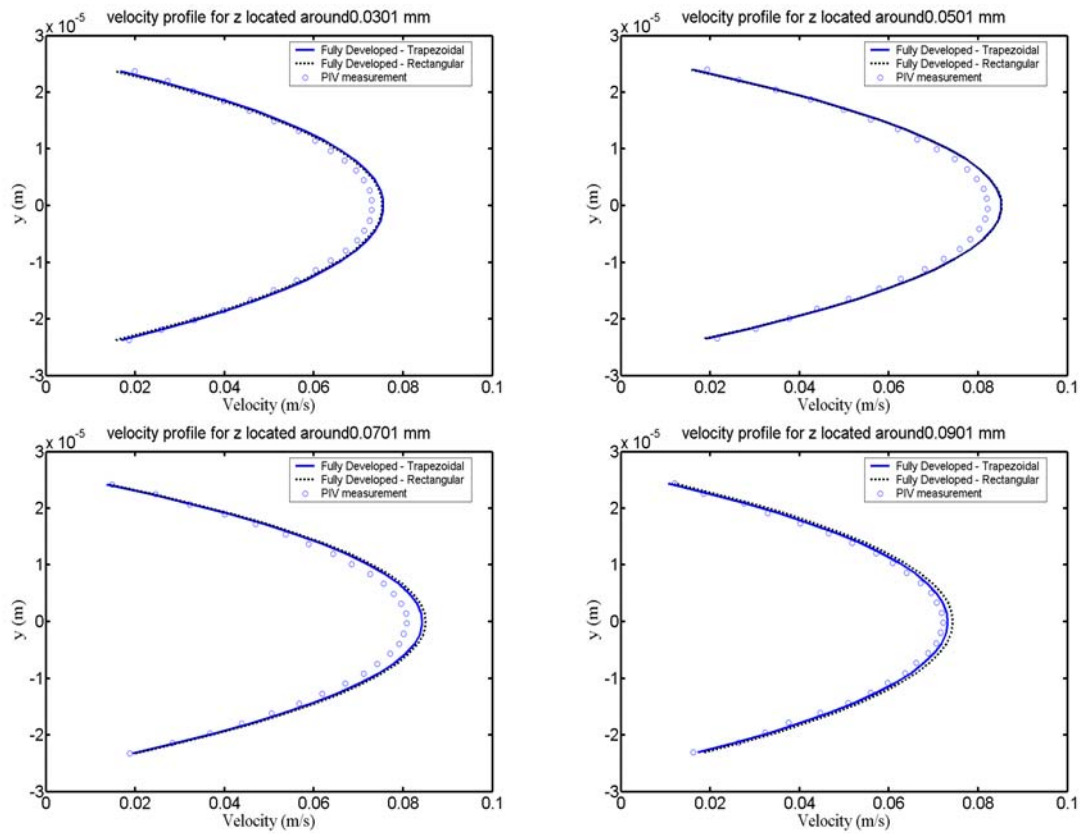


Figure 5.9 Velocity profile for SG53 (1ml/hour or 44 mm/s)

Figures 5.10 and 5.11 show the velocity profile for SG103 for different flow rates. The overall agreement is acceptable, but considerable deviation is seen near the center of the channel.

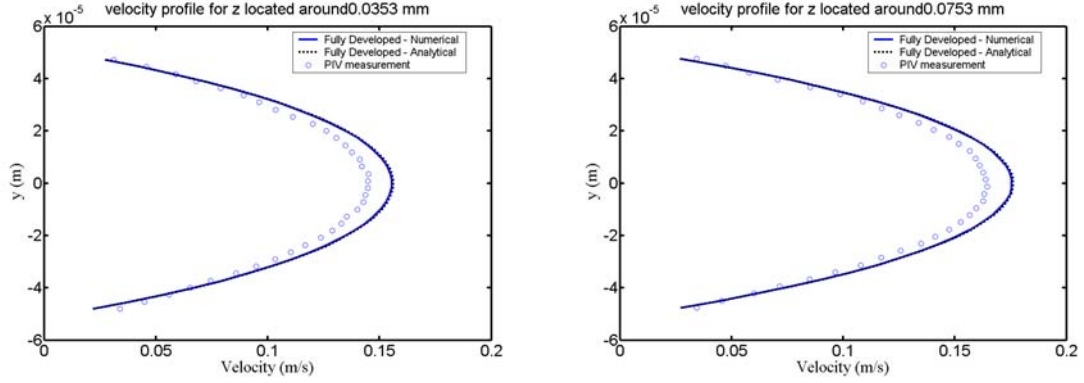


Figure 5.10 Velocity profile for SG103 (4 ml/hour or 88 mm/s)

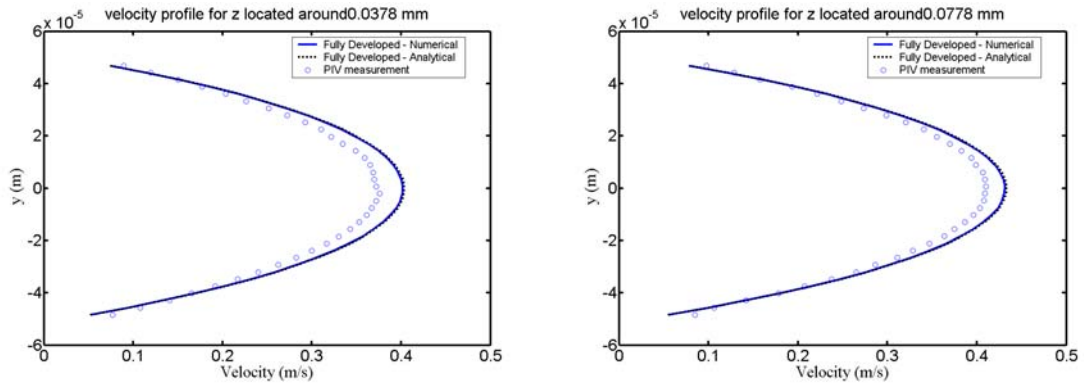


Figure 5.11 Velocity profile for SG103 (10 ml/hour or 0.22 m/s)

There are several possible reasons for this negative bias error. The first reason is the effects of both velocity gradient within the interrogation area and large velocity measurement volume. Velocity gradient can reduce the SNR ratio as the peak of the signal height will reduce due to the spread of the signal width. Meanwhile velocity is determined by averaging over the interrogation volume. The presence of large velocity gradient will make it less accurate to assign the average velocity to the centroid. Considering Equation (5.11) and (5.12), if a uniform weighting function is used, the difference between the mean velocity and the velocity at the centroid is proportional to

the second derivative of velocity and the extent of the measurement volume. As the velocity profile for microchannels is similar to a parabolic distribution, the second derivative is always negative. This may result in the negative bias in the velocity measurement. For SG103 a 40x0.6 lens and 1  $\mu\text{m}$  particles were used to image the channel. The resulted depth of measurement is much larger than the lens used for SG34 and SG53. This increases significantly the interrogation volume and thus the negative bias. A similar large deviation in velocity measurement for 100  $\mu\text{m}$  micro-tube was reported in [42].

The second reason is loss-of-pairs. Near the centerline, the local velocity peaks such that within the fixed time interval, the probability of losing particles from the interrogation area is larger. Loss-of-pair can be worse if the seeding particle density is low which is true for Micro-PIV applications. In the interrogation area fast particles are more likely to escape the interrogation such that slow particles will dominate the calculation of the average particle displacement. Even though offsetting the interrogation area was used in the current study it is still impossible to completely eliminate the problem of loss of pair.

To reduce the bias it is important to use sufficient seeding particle density. The optics of the Micro-PIV system should be optimized to achieve small measurement volume.

### 5.2.2 Developing flow near entrance

Figure 5.12 and 5.13 present results measured near the entrance of the SG103 channel. A typical velocity vector is shown in Figure 5.12 (a). In the manifold the flow is slow and subsequently accelerated upon entering the channel. At beginning the

velocity is nearly uniform and an approximately-parabolic profile establishes after about 0.1 mm from the entrance. Figure 5.12 (b) shows the mean velocity average along Y-direction at the Z-plane. As the flow approaches fully developed condition, the mean velocity for this plane stabilizes. The non-dimensional hydrodynamic developing length is determined to be 0.091 after which the variations of the mean velocity are within one percent of the fully developed value. This result matches very well with the result reported in [54].

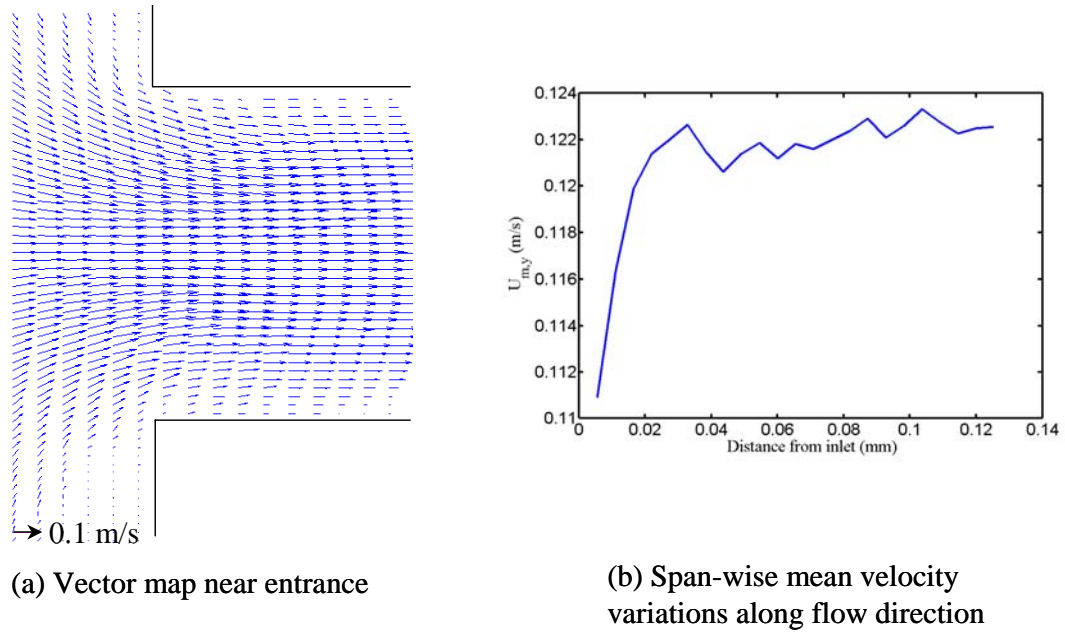


Figure 5.12 Velocity profile development for SG103 ( $Re = 9.8$ )

Figure 5.13 depicts the developing velocity profile for 10 ml/hour. As can be seen from Figure 5.13 (a), near entrance the velocity profile is almost flat at the center. As the effects of viscosity propagate into the flow core gradually, the velocity profile grows towards fully developed shape. The span-wise mean velocity increases monotonically



along the flow direction within the current field of view. Due to the limited size of the field of view, flow is still developing.

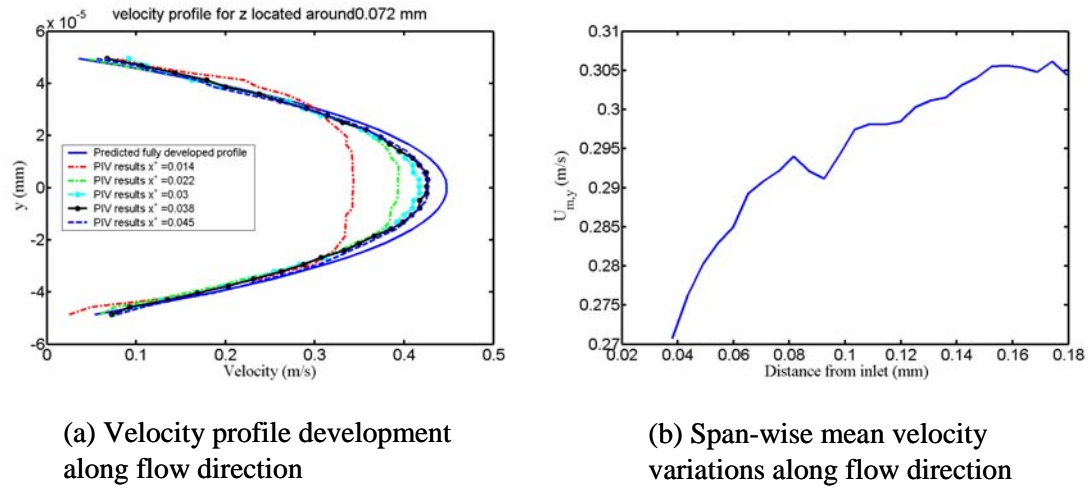


Figure 5.13 Velocity profile developing for SG103 ( $Re = 25$  or  $0.22$  m/s)

### 5.2.3 Pressure drop

Figure 5.14 shows the pressure drop measured for six different channels including the three channels studied using Micro-PIV. For all six channels, pressure drop were measured across the manifold and the atmosphere to which the end of the microchannels are open, as illustrated in Figure 2.8.

For all six cases the measured pressure drop match well with predicted pressure drop from laminar theory. The deviations are generally within 5% for all cases.

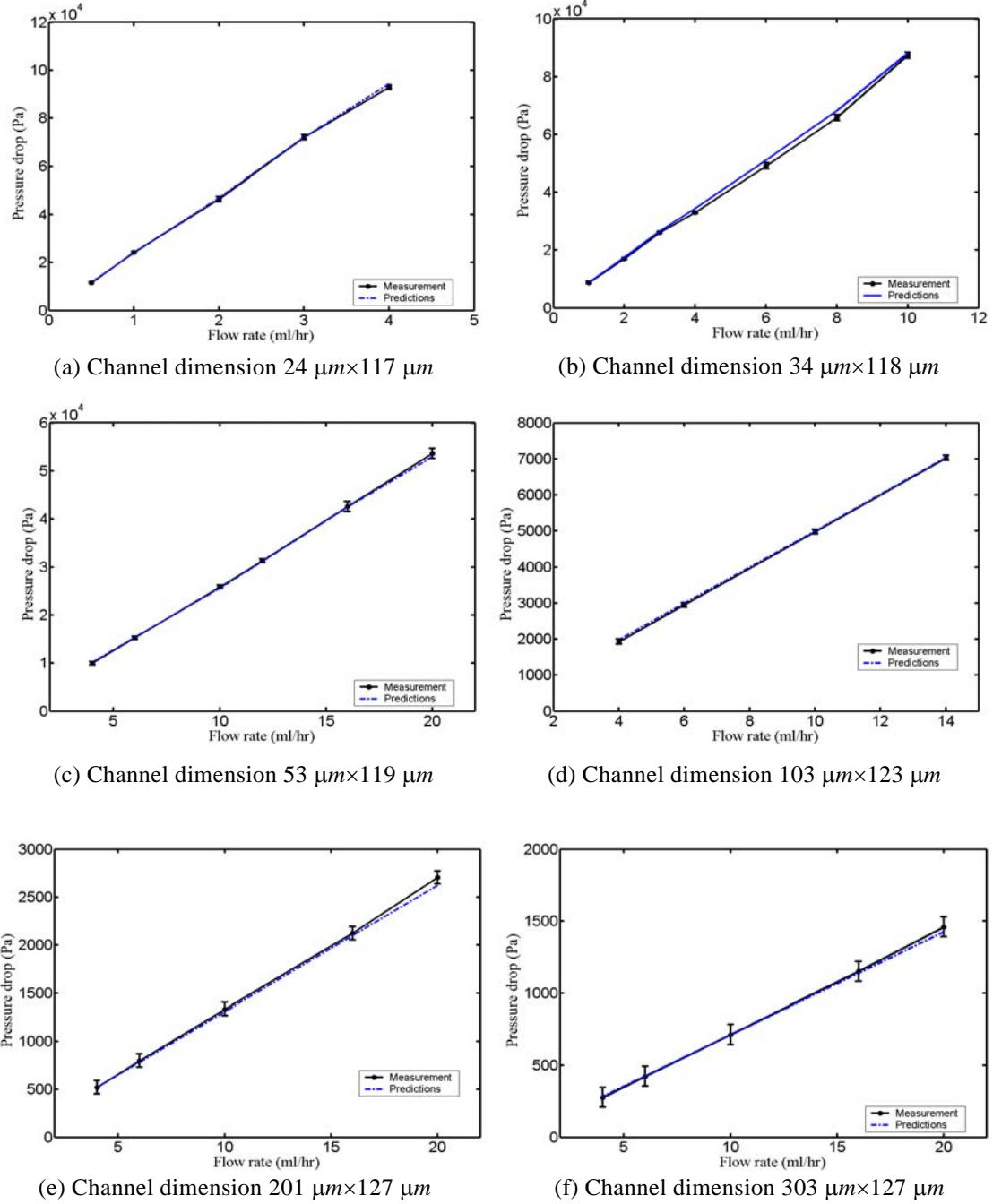


Figure 5.14 Pressure drop for microchannels of various dimensions

### 5.3 Effects of the sidewall profile on flow and heat transfer

The microchannels tested in the current study were fabricated using DRIE technique. A standard Bosch process was used to etch channels in silicon. Bosch process

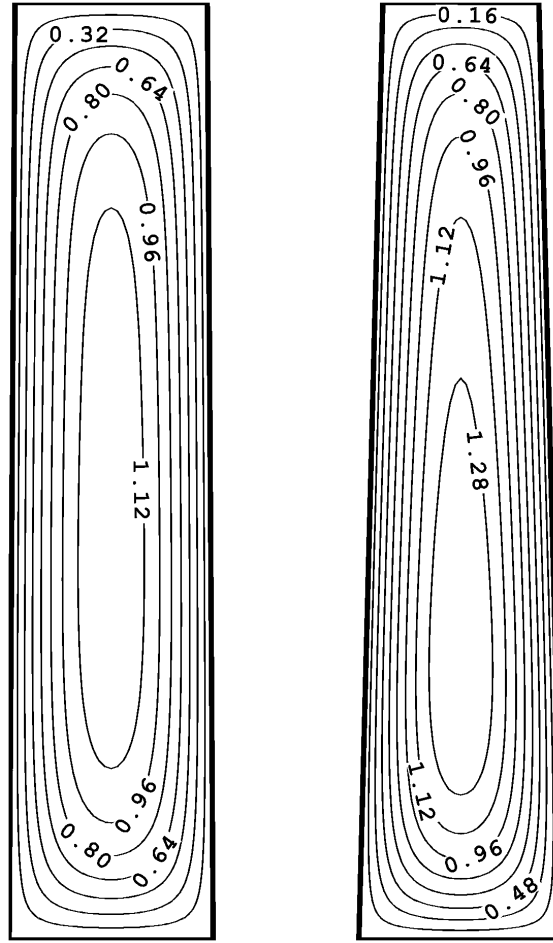
results in side wall profiles that are less than perfectly vertical. The degree of deviation depends on the aspect ratio of the etched channel, as shown in Figure 3.2. For the current study, channels SG34 and SG53 have about 0.5 degree positive slope.

The effects of this microfabrication defect were examined for channel SG34 through Micro-PIV measurement and numerical modeling. Numerical models were also developed to characterize the flow and heat transfer inside microchannels with larger slopes. The flow rate, channel depth and opening width are fixed for these studies. Effects of boundary condition and boundary layer developing were also explored through numerical modeling. The numerical modeling was validated against the results for fully developed case reported in [54].

### 5.3.1 Velocity profile and pressure drop

Deviations from rectangular cross-section ( $90^\circ$  side wall) cause deviations in velocity profiles. Figure 5.15 shows the predicted velocity contour for channels with 0.5 degree and 2 degree slope respectively. For both cases, the depth and the width of the bottom opening are the same. As the slope increases, the channel top becomes narrower such that the fluid core is pushed towards the bottom opening. This effect can be quantified by looking at  $Z_{\max}$ , the vertical location of the maximum velocity over the cross section, as defined in Figure 5.6.

Table 5.3 lists the results of  $Z_{\max}$  from Micro-PIV measurement and compares them with predicted results from modeling of a trapezoidal channel and rectangular channel for three different flow rates.



(a) SG34 ( $0.5^\circ$ )

(b) SG31 ( $2^\circ$ )

Figure 5.15 Velocity contour plot for cross-sections of different channels

Table 5.3 Location of the plane with maximum velocity for channels SG34

Flow rate (ml/hour)	1	4	10
$Z_{\max}$ ( $\mu\text{m}$ ), Micro-PIV	50.8	46.2	48.5
$Z_{\max}$ ( $\mu\text{m}$ ) rectangular model	59	59	59
$Z_{\max}$ ( $\mu\text{m}$ ), trapezoidal model	48.5	48.5	48.5

If the channel cross section is rectangular then the velocity profile should be symmetric about the  $Z=0.5H_c$  or  $59\text{ }\mu\text{m}$  plane. For the channel with  $0.5^\circ$  (SG34) the difference of the  $Z_{\max}$  between Micro-PIV measurement and rectangular assumptions is about 20%. This is rather surprising considering the channel cross-section is only  $0.5^\circ$  degree tapered. Further modeling results from numerical simulation of trapezoidal channels agree well with the measured results from Micro-PIV. If the maximum velocity plane was assumed as the symmetric plane and was used as a reference to compare the PIV measurement results with modeling results, large discrepancies would occur.

As the sidewall slope increases, this effect becomes even more dramatic. Figure 5.16 indicates the shift of maximum velocity plane from symmetric plane increases significantly with the angle. For the case of  $5^\circ$  angle, the plane of maximum velocity is located at almost one tenth of the total depth from the bottom of the channel. 72% of the total flow rate passes the lower half cross-section.

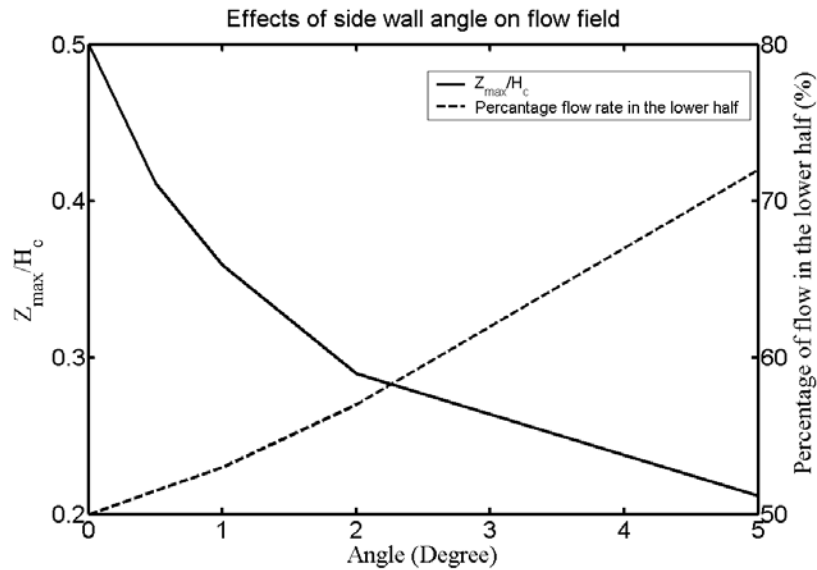


Figure 5.16 Angle effects on flow characteristics

One key parameter of microchannel flow is the pressure drop. Figure 5.17 indicates for the fixed bottom width and channel depth, as the angle increases, the pressure drop increases due to the smaller flow area. For each angle, the ratio between the friction factor for the trapezoidal channel and that for corresponding rectangular channel is generally smaller than one. This means for the same flow area trapezoidal channel has less friction loss. This reduction in friction loss is about 7% for a 5 degree angle. For small angle this effect is minimal.

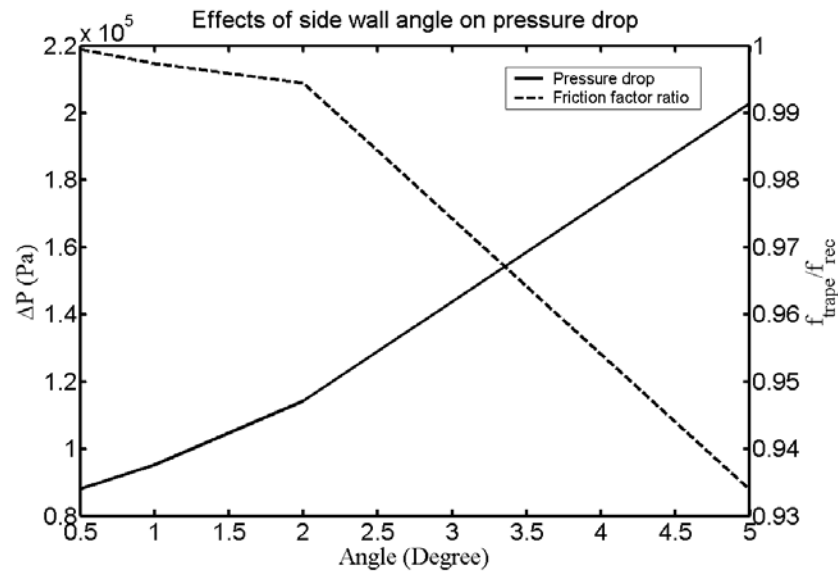


Figure 5.17 Effects of sidewall angle on friction losses. Pressure drop are for trapezoidal channel while friction factor ratio is the ratio between the trapezoidal and the corresponding rectangular channel with equal flow area.

### 5.3.2 Heat transfer

Numerical modeling was conducted for trapezoidal channel with 5° sidewall slope. Constant heat flux condition was assumed at all four walls. This is also referred as H2 condition in Shah and London [54] and other literature. For fully developed

condition, the predicted Nusselt numbers from current study agree well with results reported in Shah and London [54], which validated the modeling technique. As shown in Table 5.4, compared with rectangular channels of the same flow area, Nusselt number for a tapered channel is significantly lower. At fully developed condition, the degradation in Nusselt number is about 60%. It is interesting that near the entrance this degradation is not as significant because there the boundary layer development just starts and the velocity and temperature profile are rather close to uniform.

Table 5.4 Local Nusselt number for 5° trapezoidal channel and rectangular channel

$\frac{x}{d_H \cdot \text{Re} \cdot \text{Pr}}$	0.09	0.18	0.45	0.85	Fully developed
$\text{Nu}_{\text{H2}, x}$ rectangular	3.89	3.44	3.09	2.96	2.94
$\text{Nu}_{\text{H2}, x, 5^\circ}$ sidewall	2.7	2.09	1.56	1.35	1.21
Degradation in Nu	30%	40%	50%	54%	60%

Figure 5.18 shows temperature contour at the cross-sections of a rectangular channel and a trapezoidal channel with 5° sidewall slope. Clearly temperature gradient along the side wall of the trapezoidal channel is much steeper than the rectangular channel. As the flow core area shifts towards the bottom, the heat transfer efficiency of the upper half channel decreases significantly. As constant heat flux boundary conditions are applied, temperatures near the upper corners are significantly higher. Near the bottom, heat transfer is enhanced due to much thinner boundary layer. However, the overall heat transfer for trapezoidal is significantly lower as heat transfer degradation for side wall and top wall dominates any heat transfer enhancement for bottom wall. This is

clearly shown in Figure 5.19, where a heat transfer performance parameter is defined. This ratio lumps the effects of heat transfer degradation and pressure drop reduction due to the presence of sidewall slope.

Constant heat flux condition usually implies large ratio of heat transfer coefficient to thermal conductivity. For applications such as micro-heat-exchanger, heat transfer is usually conjugate as the highly conductive solid region also participates in heat transferring.

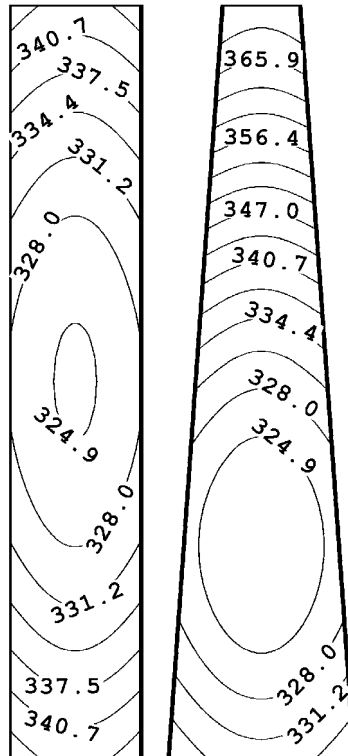


Figure 5.18 Contour map of temperature at the cross-section of rectangular and trapezoidal channel with  $5^\circ$  sidewall angle for H2 boundary condition.



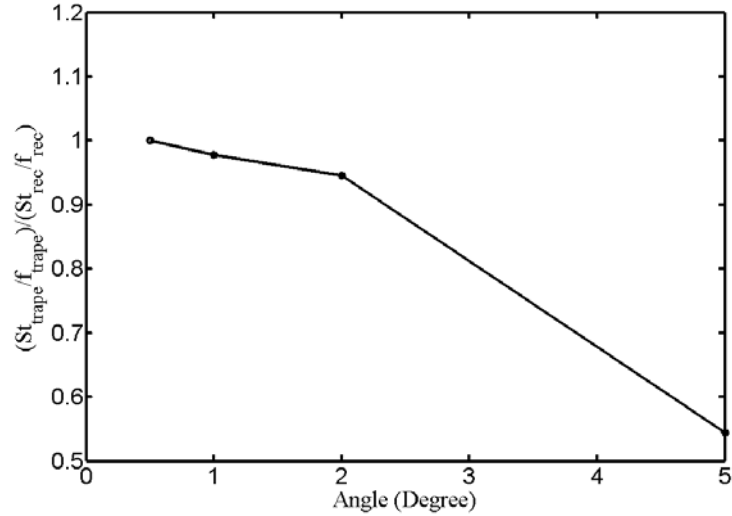
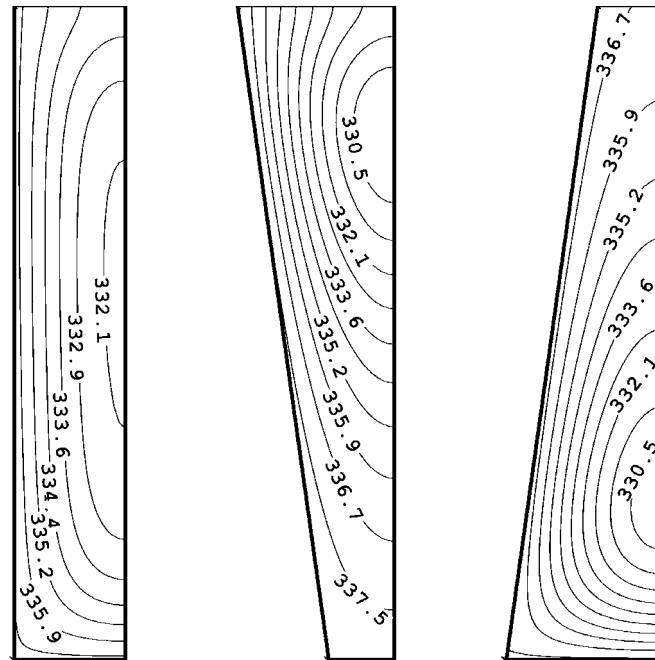


Figure 5.19 Heat transfer performance variations with sidewall angle, H2 boundary condition

Numerical modeling was conducted for conjugate heat transfer inside microchannels. Three different cases were studied in which the channel profiles were rectangular, positively-tapered and re-entrant respectively. Uniform heat flux condition was applied at the bottom of the solid region while the top of the channel was assumed adiabatic. Figure 5.20 depicts the temperature distribution across the fluid region only. In sharp contrast to the H2 condition, temperature along the side and bottom walls are almost uniform for all three cases as the temperature contour lines are nearly parallel to the boundaries. This is clearly due to high thermal conductivity of silicon (148 W/mK). Compared with rectangular channel 5.20 (a), cold cores for positively tapered channel 5.20 (b) and re-entrant channel 5.20 (c) shift towards top and bottom respectively. Consequently, heat transfer near lower left corner of 5.20 (b) and upper left corner of 5.20 (c) are significantly reduced. However, as the solid region surrounding the channels is very conductive, more heat is dissipated near the flow and cold core area which is

impossible for H2 condition. This is evidently shown in Figure 5.21. Therefore the overall degradation in heat transfer for conjugate heat transfer is much less as is shown in Table 5.5. It is interesting that for conjugate heat transfer, re-entrant channel is more efficient than a positively tapered channel. There are two reasons for this. First as the top wall is adiabatic, the total heat transfer area for re-entrant channel is slightly larger. Secondly and more importantly, the bottom wall of the re-entrant channel contributes more efficiently to heat transfer as the boundary layer is much thinner while for the positively tapered channel this contribution is much less. As indicated in Table 5.5, mean Nusselt number for bottom wall is 2.93 for the re-entrant channel and 0.6 for the positively tapered case.



(a) Rectangular (b) 5° (positive taper) (c) -5° (re-entrant)

Figure 5.20 Contour map of temperature at the cross-section of channels for conjugate heat transfer (only half of the fluid cross-section is shown). Uniform heat flux is applied at bottom of the silicon and the top surface is adiabatic.

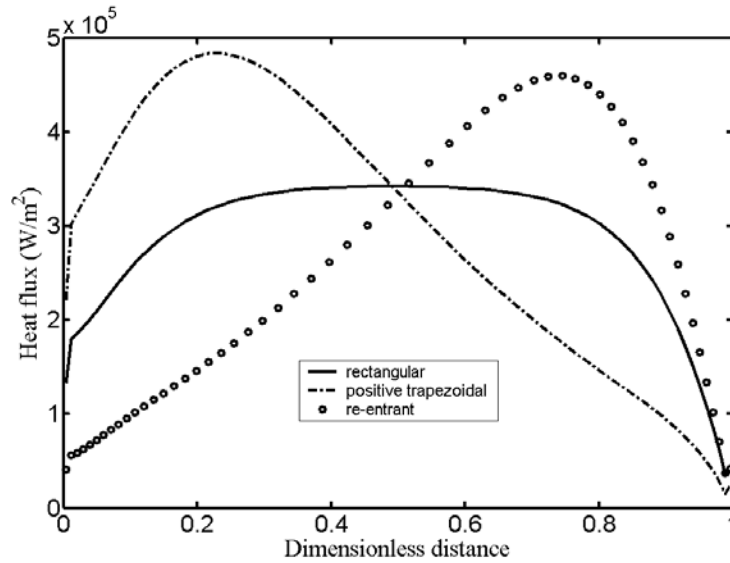


Figure 5.21 Heat flux distribution along the sidewalls of all three channels

Table 5.5 Nusselt numbers for rectangular, positively tapered and re-entrant channels for H2 boundary condition or conjugate heat transfer ( $x^+=0.45$ )

Angle	$Nu_{H2, m}$	$Nu_{conj, m}$	$Nu_{H2, side}$	$Nu_{conj, side}$	$Nu_{H2, bot}$	$Nu_{conj, bot}$	$Nu_{H2, top}$
$0^\circ$	3.05	5.19	4.43	5.58	1.13	2.02	1.13
$-5^\circ$	1.56	4.13	1.69	4.33	0.41	2.93	4.56
$5^\circ$	1.56	3.93	1.69	4.18	4.56	0.6	0.41

In summary, the effects of sidewall tapering due to micro-fabrication defects were examined. Even  $0.5^\circ$  slope in channel sidewall can cause 20% deviation on the location of the maximum velocity. As the angle increases, the flow and cold core is shifted towards wider side of the channel cross-section. For constant heat flux condition, serious degradation in overall heat transfer occurs for channel with  $5^\circ$  slope. For conjugate heat

transfer, the degradation in heat transfer is much less and re-entrant channel has better heat transfer performance than positively tapered channel.

#### **5.4 Summary and Conclusion**

Microchannels of different dimensions were studied using Micro-PIV imaging technique. Detailed 2-D velocity profiles were obtained for different planes thus overall velocity map of the 3-D structure were resolved. Numerical modeling were performed to investigate the effects of the side wall slope due to microfabrication defects on the flow and heat transfer characteristics. It is concluded that:

- a) Measured velocity profile at different planes generally match with results predicted from laminar theory for channel SG34 and SG53. Considerable deviation near the center of the channel for SG103 was observed and believed to be measurement bias error due to large measurement volume.
- b) Measured boundary layer developing length agrees with the result from literature for the rectangular channel SG103.
- c) Measured pressure drop for six different channels agree well with laminar theory for the flow rate range tested.
- d) Sidewall slope has significant impact on the velocity distribution over the cross-section of microchannels. For the channel SG34 with 0.5 degree slope, the location of maximum velocity deviates from the nominal symmetric plane by 20%. This deviation increases dramatically as the angle increases. For 5 degree slope, 72% percent of the total flow rate passes from the lower half of the channel. The effects of the sidewall slope on pressure drop are not significant.

- e) Sidewall slope has significant impacts on heat transfer. For constant heat flux condition H2, 60% degradation in fully developed heat transfer was found for 5 degree slope case. For developing flow and conjugate heat transfer the degradation is less evident. For conjugate heat transfer, re-entrant channel has better heat transfer efficiency than positively tapered channel.

## CHAPTER 6

### SUMMARY, CONCLUSIONS, DESIGN GUIDELINES AND RECOMMENDATIONS FOR FUTURE WORK

#### 6.1 Summary

The advantages and limitations of liquid cooling employing microchannels for microelectronics were outlined based on the scaling law. A stacked microchannel heat sink was fabricated using microfabrication techniques to address the limitations of single-layered microchannel heat sinks. Experiments were conducted to study thermal performance of the stacked microchannel structure. Total thermal resistance of less than 0.1 K/W was demonstrated. The effects of flow direction and flow rate ratio in each microchannels layer were investigated. Both uniform heating and partial heating conditions were evaluated. Numerical simulations were conducted to study the conjugate heat transfer inside stacked microchannels. Micro-PIV measurements were conducted for laminar flow inside channels of different width.

#### 6.2 Conclusions

- a) Stacked microchannel heat sink with two layers of microchannels results in thermal resistance as low as  $0.09\text{ }^{\circ}\text{C}/(\text{W}/\text{cm}^2)$  for both counter flow and parallel flow configurations. For the flow rate range tested the counter flow microchannel heat sink has better temperature uniformity. At 83 ml/min, counter flow produces 40% less temperature non-uniformity than parallel flow. For small flow rate range parallel flow configuration has lower total thermal resistance. At high flow rate thermal performance for both are indistinguishable.

- b) For both counter flow and parallel flow heat sinks total thermal resistance decreases when more fluid flows through the bottom layer microchannels than through the top layer. However, the pressure drop significantly increases. The flow ratio between the top and bottom layer can be customized to achieve both low pumping power and good overall thermal performance.
- c) For parallel flow, on-chip resistance decreased as more flow was pumped through the bottom layer microchannels. For counter flow, on-chip resistance decreased as more flow was pumped through top layer microchannels. Therefore, there is an optimum ratio between top layer and bottom layer microchannels to minimize both total thermal resistance and on-chip resistance for counter flow heat sinks.
- d) Partial heating cases have significantly higher total thermal resistance than full heating due to the localization of heat source. For the smallest flow rate tested, thermal resistance for partial heating increases compared to uniform heating by about 20% for parallel flow and 30%-40% for counter flow cases. This effect increases as flow rate increases.
- e) It is revealed through numerical simulation that for counter flow heat flux is negative for part of the microchannels if the flow rate is small. This is considered responsible for the higher thermal resistance for counter flow than for parallel flow. This effect is less important for the larger flow rate. For parallel flow, the heat flux at the top layer increases along the flow direction for the majority of the channel due to the heat transfer interaction between the top and bottom layer. This effect is more important for large flow rates.

- f) Velocity profiles at different channel depths were measured using Micro-PIV technique. The results generally match with predicted values from laminar theory. Considerable deviation near the center of the channel for SG103 was observed and believed to be measurement bias error. Possible reasons include large measurement volume and loss of pairs. Measured pressure drop for six channels of different dimensions agree well with laminar theory for the flow rate range tested.
- g) Boundary layer development length was measured using Micro-PIV and the result agrees with the value predicted from laminar theory for a rectangular microchannel.
- h) Sidewall slope has significant impact on the velocity distribution over the cross-section of microchannels. For 0.5 degree slope, the location of maximum velocity deviates from the nominal symmetric plane by 20%. This deviation increases dramatically as the angle increases. For 5 degree slope, 72% percent of the total flow rate passes from the lower half of the channel. The effects of the sidewall slope on pressure drop are not significant.
- i) Effects of sidewall slope on heat transfer can be significant. For constant heat flux condition H2, 60% degradation in heat transfer coefficient was found for 5 degree slope for fully developed conditions. For developing flow and including conjugate heat transfer the degradations are also significant but less dramatic. With conjugate heat transfer included there is 25% degradation in the mean Nusselt number for 5 degree slope. It is also found that re-entrant channels have better heat transfer performance than positively tapered channels.



### **6.3 Design guidelines for stacked microchannel heat sinks**

Based on the current work and previous related researches [3] the following guidelines are proposed for designing stacked microchannels for electronic cooling.

- a) For water-cooled silicon microchannels with relative high aspect ratio ( $\sim 6$ ) no more than two layers should be stacked as there is no significant benefit in thermal performance beyond two layers due to the fin efficiency constraints.
- b) For low conductivity materials such as stainless steel, there is no benefit in thermal performance by stacking microchannels (aspect ratio  $\sim 6$ ) layers.
- c) For a two-layered microchannel heat sink the channel aspect ratio should be less than 4 for stainless steel and less than 6 for silicon in order to maximize the benefits of stacking microchannels.
- d) Thermal resistance of an optimized stacked microchannel heat sink is strongly dependent on the channels length. The shorter the channel, the smaller the thermal resistance for the optimized stacked microchannel heat sink.
- e) The negative heat flux effects are most severe when the flow rate is low and the heat sink material is very conductive. Under these scenarios parallel flow arrangement should be chosen.

#### **6.4 Recommendation for future work**

- a) Parametric study of the effects of channel dimensions and thermal conductivity ratio between solid materials and the fluid on the conjugate heat transfer and overall thermal performance for uniform and discretely heated stacked microchannels.
- b) Systematic evaluation of the effects of the bonding conditions on the thermal interface resistance for stacked microchannels. These include bonding temperature, time, and pressure. These parameters may have significant impact on the implementation of stacked microchannel cooling technique.
- c) As measuring temperature on the wall has proven to be in-sufficient to fully understand the heat transfer phenomenon inside microchannels, direct measurement of temperature field becomes necessary. One such potential technique is to use Micro-PIV to measure velocity and temperature simultaneously based on the Brownian motion contribution to the broadening of the cross-correlation peak.
- d) Study of enhancement in heat transfer due to the presence of nano-particles in microchannels. It has been reported that nano-particles can enhance the effective thermal conductivity of the suspension and the convective heat transfer process, while have little effects on the friction loss. A further study of the particle concentration using Micro-PIV can enhance understanding the underlying physics of the reported enhancement in heat transfer.

## REFERENCES

- [1] International Technology Roadmap for Semiconductors, "International Technology Roadmap for Semiconductors 2003", <http://public.itrs.net/>
- [2] Tuckerman, D.B. and Pease, R.F.W., 1981, "High performance heat-sinking for VLSI", IEEE electron Device Letter 2, 126-129
- [3] Wei, X. J., Joshi, Y. K., 2004, "Stacked Microchannel Heat Sinks for Liquid Cooling of Microelectronic Components", Journal of Electronic Packaging, 126, 60-66
- [4] Fedorov, A.G. and Viskanta, R., 2000 "Three-dimensional conjugate heat transfer in the micro-channel heat sink for electronic packaging", International Journal of Heat and Mass Transfer, 43, 399-415
- [5] Blech, I.A. and Meieran, E.S., 1967, "Direct Transmission Electron Microscope Observations of Electrotransport in Aluminum Films", Applied Physics Letters, 11, 263
- [6] Bau, H.H., 1998, "Optimization of Conduits' Shape in Micro Heat Exchangers", International. Journal of Heat and Mass Transfer, 41, 2717-23
- [7] Tuckerman, D.B., 1984, "Heat-Transfer Microstructures for Integrated Circuits", PhD Dissertation, Stanford University
- [8] Harpole, G.M. and Eninger, J.E., 1991, "Micro-channel Heat Exchanger Optimization", Proceedings of the Seventh IEEE Semi Therm Symposium, 59-63
- [9] Copeland, D., Behnia, M. and Nakayama W., 1996, "Manifold Microchannel Heat Sinks: Isothermal Analysis", Proceedings of I-THERM V, 251-257
- [10] Ng, E.Y.K. and Poh, S.T., 1999, "Investigative Study of Manifold Microchannel Heat Sinks for Electronic Cooling Design", Journal of Electronics Manufacturing, 9, 2, 155-166
- [11] Vafai, K and Zhu, L, 1999, "Analysis of two-layered micro-channel heat sink concept in electronic cooling", International Journal of Heat and Mass Transfer, 12, 2287-2297
- [12] Wu, P. and Little, W.A., 1983, "Measurement of Friction Factors for the Flow of Gases in Very Fine Channels Used for Microminiature Joule-Thompson Refrigerators, Cryogenics, 23, 5, 273-277
- [13] Pfahler, J., Harley, J., Bau, H.H. and Zemel, J., 1991, "Gas and Liquid Flow in Small Channels", Micromechanical Sensors, Actuators and Systems, eds. Choi et al., ASME DSC 32, 49-60

- [14] Peng, X.F., Peterson, G.P. and Wang, B.X., 1994, "Frictional Flow Characteristics of Water Flowing through Rectangular Microchannels", *Experimental Heat Transfer*, 7, 249-264
- [15] Peng, X.F., Peterson, G.P. and Wang, B.X., 1994, "Heat Transfer Characteristics of Water Flowing through Rectangular Microchannels", *Experimental Heat Transfer*, 7, 265-283
- [16] Papautsky, I., Brazzle, J., Ammel, T. and Frazier, A.B., 1999, "Laminar Fluid Behavior in Microchannels Using Micropolar Fluid Theory", *Sensors and Actuators*, 73, 101-108
- [17] Harms, T.M., Kazmierczak, M.J., and Gerner, F.M., 1999, "Developing Convective Heat Transfer in Deep Rectangular Microchannels", *International Journal of Heat and Fluid Flow*, 210, 149-157
- [18] Mala, G.M. and Li, D., 1999, "Flow Characteristics of Water in Microtubes", *International Journal of Heat and Fluid Flow*, 20, 142-148
- [19] Mala, G.M., Li, D., Werner C., Jacobasch H.J., and Ning Y.B, 1997, "Flow Characteristics of Water Through Microchannels Between Two Parallel Plates with Electrokinetic Effects", *International Journal of Heat and Fluid Flow*, 18, 489-496
- [20] Tso, C.P. and Mahulikar, S.P., 1998, "The Use of the Brinkman Number for Single Phase Forced Convective Heat Transfer in Microchannels", *International Journal of Heat and Mass Transfer*, 41, 12, 1759-1769
- [21] Xu, B., Ooi, K. T., and Wong, N. T., 2000, "Experimental Investigation of Flow Friction for Liquid Flow in Microchannels", *International Communications in Heat and Mass Transfer*, 27, 1165-1176.
- [22] Liu, D. and Garimella, S. V., 2002, "Investigation of Liquid Flow in Microchannels", 8<sup>th</sup> AIAA/ASME Joint Thermophysics and Heat Transfer Conference, St. Louis, Missouri, Paper No. AIAA 2002-2776
- [23] Lee, P. and Garimella, S. V., 2003, "Experimental Investigation of Heat Transfer in Microchannels", HT2003-47293, Proceedings of HT2003, ASME summer heat transfer conference.
- [24] Baviere, R., Ayela, F., Person, S. Le. and Favre-Marinet, M., 2004, "An Experimental Study of Water Flow in Smooth and Rough Rectangular Micro-channels", 2<sup>nd</sup> International conference on microchannels and minichannels, Rochester, New York, 221-228
- [25] Phillips, R.J., 1990, "Microchannel Heat Sinks", *Advances in Thermal Modeling of Electronic Components*, 2, Chapter 3, 109-184, ASME Press

- [26] Knight, R.W., Hall, D.J., Goodling and J.S., Jaeger, R.C., 1992, "Heat Sink Optimization with Application to Microchannels", IEEE Transactions on Components, Hybrids and Manufacturing Technology, 15, 5, 832-842
- [27] Weisberg, A. and Bau, H.H., 1992, "Analysis of Microchannels for Integrated Cooling", International Journal of Heat and Mass Transfer, 35, 10, 2465-2474
- [28] Yin, X. and Bau, H.H., 1997, "Uniform Channel Micro Heat Exchangers", Journal of Electronic Packaging, 119, 89-95
- [29] Adrian, R.J., 1991, "Particle Imaging Techniques for Experimental Fluid Mechanics", Annual Review of Fluid Mechanics, 23, 261-304
- [30] Santiago, J.G., Wereley, S.T., Meinhart, C.D., Beebe, D.J., and Adrian, R.J., 1998, "A Particle Image Velocimetry System for Microfluidics", Experiments in Fluids, 25, 316-319
- [31] Meinhart, C.D., Wereley, S.T. and Santiago, J.G., 1999, "PIV Measurements of a Microchannel Flow", Experiments in Fluids, 27, 414-419
- [32] Meinhart, C.D., Zhang, H.S., 2000, "The Flow Structure Inside a Microfabricated Inkjet Printhead", Journal of Microelectromechanical Systems, 9, 1, 67-75
- [33] Sharp, K.V., Adrian, R.J. and Beebe, D.J., 2000, "Anomalous Transition to Turbulence in Microtubes", MEMS 2, 461-466
- [34] Zeighami, R., Laser, D., Zhou, P., Asheghi, M., Devasenathipathy, S., Kenny, T., Santiago, J., and Goodson, K., 2000, "Experimental Investigation of Flow Transition in Microchannel Using Micro-resolution Particle Image Velocimetry", Proceedings of ITHERM 2000, Volume II, 148-153
- [35] Meinhart, C.D., Wereley, S.T. and Gray, M.H.B., 2000, "Volume Illumination for Two-Dimensional Particle Image Velocimetry", Measurement Science and Technology, 11, 809-814
- [36] Olsen, M.G. and Adrian, R.J., 2000, "Out-of-Focus Effects on Particle Image Visibility and Correlation in Microscopic Particle Image Velocimetry", Experiments in Fluid, 29, 166-174
- [37] Bourdon, C.J., Olsen, M.G. and Gorby A.D., 2004, "validation of an Analytical Solution for Depth of Correlation in Microscopic Particle Image Velocimetry", Measurement Science and Technology, 15, 318-327
- [38] Olsen, M.G and Bourdon C.J., 2003, "Out-of-Plane Motion Effects in Microscopic Particle Image Velocimetry", Journal of Fluids Engineering, 125, 895-901

- [39] Olsen, M.G. and Adrian, R.J., 2000, "Brownian Motion and Correlation in Particle Image Velocimetry", *Optics and Laser technology*, 32, 621-627
- [40] Devasenathipathy, S, Santiago, J. G., Wereley, S. T., Meinhart, C. D., and Takehara K., 2003, " Particle Imaging Techniques for Microfabricated Fluidic Systems", *Experiments in Fluids*, 34, 504-514
- [41] Liu, D., Garimella, S. V. and Wereley, S.T., 2004, "Infrared Micro-Particle Image Velocimetry of Fluid Flow in Silicon-Based Microdevices", 2004 ASME Heat Transfer /Fluids Engineering Summer Conference, Charlotte, North Carolina, Paper number HT-FED04-56385
- [42] Park, J.S., Choi, C.K. and Kihm, K.D., 2004, "Optically Sliced Micro-PIV Using Confocal Laser Scanning Microscopy (CLSM)", *Experiments in Fluids*, 37, 105-119
- [43] <http://grover.mirc.gatech.edu/processinfo/stdrecipes/bosch.pdf>
- [44] Hongseok Noh, 2004, " Parylene Microcolumn for Miniature Gas Chromatograph", doctorate dissertation, Georgia Institute of Technology.
- [45] Tong, Q. Y. and Gösele, U., 1999, *Semiconductor wafer bonding: science and technology*, New York : John Wiley
- [46] Lasky, J B, 1986, "Wafer bonding for silicon-on insulator technology", *Applied Physics Letter*, 48, 78
- [47] Hunt, C. E., Desmond, C. A., Ciarlo, D. R. and Benett, W. J., 1991, "Direct bonding of micromachined silicon wafers for laser diode heat exchanger applications", *Journal of Micromechanics and Microengineering*, 1, 152-156
- [48] Lin, C. C., Ghodssi, R, Avon, A. A., Chen, D.-Z., Jacobson, S., Breuer, K., Epstein, A. H. and Schmidt M. A., 1999, "Fabrication and characterization of a micro turbine/bearing rig", *Twelfth IEEE International Conference on Micro Electro Mechanical Systems* , 529-533
- [49] Raffel, M., Willert, C.E. and Kompenhans, 1998, *Particle Image Velocimetry: a Practical Guide*. Springer, Berlin Heidelberg New York
- [50] Meinhart, C.D., Wereley, S.T. and Santiago, J.G., 2000, "A PIV Algorithm for Estimating Time-Averaged Velocity Fields", *Journal of Fluids Engineering*, 122, 285-289
- [51] Meinhart, C.D. and Wereley, S.T, 2003, "The Theory of Diffraction-Limited Resolution in Microparticle Image Velocimetry", *Measurement Science and Technology*, 14, 1047-1053

- [52] Parasad, A.K., Adrian, R.J., Landreth, C.C. and Offutt P.W., 1992, "Effects of Resolution on the speed and accuracy of Particle Image Velocimetry Interrogation", *Experiments in Fluids*, 13, 105-116
- [53] Tsuei, L and Savas, O, 2000, "Treatment of Interfaces in Particle Image velocimetry", *Experiments in Fluids*, 29, 203-214
- [54] Shah, R.K. and London, A.L., 1978, *Laminar Flow Forced Convection in Ducts*, Academic Press, New York